3D1D Modeling of the Convective-Reactive Mixing in Rapidly Accreting White Dwarfs

by

David Stephens
B.Sc., University of Waterloo, 2017

A Thesis Submitted in Partial Fulfillment of the
Requirements for the Degree of

MASTER OF SCIENCE

in the Department of Physics and Astronomy

University of Victoria

3D1D Modeling of the Convective-Reactive Mixing in Rapidly Accreting White Dwarfs

by

David Stephens
B.Sc., University of Waterloo, 2017

Supervisory Committee

Dr. Falk Herwig, Supervisor
(Department of Physics and Astronomy)

Dr. Arif Babul, Departmental Member
(Department of Physics and Astronomy)

Abstract

1D stellar evolution and nucleosynthesis simulations have traditionally modeled the mixing within convection zones as a diffusive process. The fluids within a convection zone are advecting and do not diffuse. However the diffusive approximation is valid when the burning timescale of an exothermic reaction is longer than the convective turn over timescale to which the mixing of those species is approximated over. Since it is 1D, it also assumes that the material is isotropically distributed within the convection zone. In the He-flash convection zones of rapidly accreting white dwarfs (RAWD) H is ingested and burned well within the convective turn over time of 38 minutes. The H is burned through the exothermic $^{12}\mathrm{C}(p,\gamma)^{13}\mathrm{N}$ reaction, $\mathrm{Q} = 1.944$ MeV, and then the unstable $^{13}\mathrm{N}$, with a half-life of 9.6 minutes, will decay to $^{13}\mathrm{C}$ which will undergo the $^{13}\mathrm{C}(\alpha,n)^{16}\mathrm{O}$ reaction releasing neutrons. The neutron densities, depending on the H-ingestion rates and mixing details, reach $N_n \approx 10^{13} - 10^{15}$ cm^{-3} which starts the *i*-process within the convection zone. The H burning provides energy to the flow leading to the dynamic details of the flow being important for the mixing of the H and thus the *i*-process nucleosynthesis. This is a convective-reactive environment. The isotropic, well mixed over many convective turn over timescales, and long burning timescale assumptions for H in the diffusive approximation are broken in the convective-reactive environment of a He-shell flash convection zone in a RAWD.

To more accurately model convective-reactive mixing environments, a 1D two stream advective mixing model is formulated. A downstream advects H-rich material from the top of the convection zone down to the H-burning region while the upstream advects H-poor material back up to the upper convective boundary. The mixing model includes a horizontal mass flux, γ, which describes the efficiency to which mass is mixed between the two streams. This predominately causes the homogenization of the material between the two streams. The radial mass flux, α, and the horizontal mass flux, γ, are calibrated from 3D hydrodynamic simulations of the RAWD in order to model the mixing within the He-flash shell convection zone.

The downsampled 3D cartesian data output, the *briquette* data, from the 3D hydrodynamic simulations is used to compute γ. This required using numerical tools to interpolate quantities onto spherical shells from 3D cartesian data and to decompose the radial velocity field into its spherical harmonic modes. Trilinear interpolation is the simplest 3D interpolation method that was tested and it was the interpolation method of choice due to the constraints it has on the interpolating function. The validity of using higher order methods on the *briquette* data was studied in detail but was determined to not be usable due to the computational effort and constraints of the methods.

The two stream model post-processing of the H burning within the 3D hydrodynamic simulations of the RAWD showed excellent agreement in the metrics of the total mass of H burned, the burning rate and burning location of H. This includes two models which undergo dramatic H-ingestion and burning events caused by a GOSH, Global Oscillations of Shell H-ingestion. By adding a network containing 1000's of species to the 1D advective mixing model, the *i*-process from the RAWD is simulated and compared with a traditional 1D diffusive mixing model. The resulting neutron densities between the two models are comparable however the efficiency to which each produce the heaviest stable elements are different. To reproduce the elemental abundance distribution of the CEMP-r/s star CS31062-050, the diffusive model is run for 15 days of stellar time while the advective model is run for 20 days. The H-ingestion into the He-shell as predicted by the stellar evolution calculations lasts 30 days. The *i*-process material within the RAWD can be removed from it and participate in the galactic chemical evolution of the galaxy that it resides in. This is due to the RAWD possibly reaching the Chandrasekhar mass and from the loss of material through stellar winds and common envelope interactions with its nearby companion star.

Contents

List of Tables

List of Figures

Acknowledgements

First of all, I cannot forget my family and friends back in Ontario who have been supporting me throughout the years. I wouldn't have made it to this point without them. I would like to thank my parents, **Geoffrey and Julianna Stephens** and my brothers, **Ryan and Scott Stephens**.

For my masters thesis work here in Victoria I would like to thank:

- **Falk Herwig** for providing me with the opportunity to study stars. There is no doubt in my mind that 3D stellar hydrodynamic simulations and the *i*-process are cool.
- **Paul Woodward** for writing the 3D hydro code and ensuring that I never have to read or understand anything past the "flags" file!
- **Robert Andrassy** for the insight and discussions on the nature of convection in stellar interiors. Your work in *ppm.py* shows that user friendly code can be written by those in science!
- **Pavel Denissenkov** for enabling the implementation of this advective mixing model into `mppnp` under a very short timeline. Thanks! It was really nice to see how this model works with a full network.
- **Michael Zingale** for his "introduction to computational astrophysical hydrodynamics" (`pyro`) notes. This advective model could never have been finished on time without its great discussion of the numerics involved with advection.
- **Mariah Bridgeman** for coming out to the west coast for me (and probably the harbour seals and otters too).

Dedication

I would like to dedicate this thesis to the harbour seals, otters and sea lions of Southern Vancouver Island.

1

Introduction

"The nitrogen in our DNA, the calcium in our teeth, the iron in our blood, the carbon in our apple pies were made in the interiors of collapsing stars. We are made of star stuff."

– Carl Sagan, *Cosmos*

1.1 Background

Even before written history, humans have looked to the night sky and used the stars to keep track of time. By creating shapes out of collections of bright stars, the constellations as time tracking devices were passed down through generations. Across many ancient cultures the stars and constellations were thought to be in the realm of the gods and far away from the Earth. Early attempts to measure the parallax of the stars with the naked eye by the Greeks, Persians and Tycho Brahe all yielded null results which they erroneously used as evidence for geocentrism. Well after the invention of the telescope, precise enough measurements could be made to discover the parallax of distant stars, first by Bessel, Struve and Henderson in the mid 1800's, which brought to scale the enormous distances to the closest stars.

With simple estimates of the energy output of the Sun being unfathomably large, many theoretical models tried to predict the source of the energy of the Sun. Lord Kelvin had theorized the Suns energy source to be from gravitational contraction but this could only be true if the Sun had formed only 9 million years ago. This was known to be false due to radiometric dating of rocks on Earth setting the age of the Earth around 4.5 billion years old. It wasn't until the mid 20th century that the dominant energy source of main sequence stars was discovered, the nuclear fusion of hydrogen.

With many of the details of stellar evolution being figured out since then, a new interest in stars comes from their connection with galactic chemical evolution. Excluding the Big-Bang nucleosynthesis of H, He and Li, the elements in the universe were created through stellar processes. The α elements and Fe were created by nuclear fusion in massive stars while any elements heavier than Fe were created by neutron capture processes within stars (Meyer, 1994). The elemental distribution measured on the surface of the Sun, the Earth and all objects in the solar system, comes from the remnants of stars. Whether the bulk of the heaviest metals were formed in the He-flash convection zones of asymptotic giant branch (AGB) stars (Busso et al., 2001), the supernovae of super massive stars (Woosley & Weaver, 1995) or the merging of neutron stars (Abbott et al., 2017), the study of the origin of the elements in our universe is the study of stars.

1.2 Stellar Physics

To discuss the physics of stars, 3 different masses of stars are used to highlight different properties and evolutionary behaviour. These are the Sun ($1\mathrm{M}_\odot$, $\mathrm{Z}_\odot$), a $3\mathrm{M}_\odot$, $\mathrm{Z}_\odot$ star which is a progenitor for a Rapidly Accreting White Dwarf (RAWD) model of Denissenkov et al. (2019) and a $25\mathrm{M}_\odot$, $\mathrm{Z}_\odot$ star that includes all major burning stages that occur within stars.

1.2.1 Stellar Timescales

Stars are spherically symmetric spheres of plasma that evolve on extraordinarily long timescales for most of their lives. From the initial collapse of cold H gas into a sphere, its first ignition of H fusion, expansion into red giants and to their eventual death to a white dwarf, neutron star or black hole, a stars life is full of change. A star lives out most of its life through the main sequence, defined by the H burning within their cores. Depending on their mass, the stable H-core burning phase can last 10's of millions of years to 10's of billions of years. This burning phase has an associated timescale that depends on their initial mass and composition, the nuclear timescale τ_n for a species n. The Sun has an expected H burning timescale, $\tau_\mathrm{H} \approx 10$ Gyr while a $3\mathrm{M}_\odot$ star has $\tau_\mathrm{H} \approx 370$ Myr and a $25\mathrm{M}_\odot$ star has a $\tau_\mathrm{H} \approx 6.4$ Myr (Ritter et al., 2018b). Stars with more mass than the Sun have significantly shorter τ_H even though they have much more H available for burning because their energy loss per second at their surface, luminosity, can be over a million times larger than the Sun. The H burning timescale can be represented as the ratio of the total amount of energy that can be released from burning H, E_{H}, to the rate at which the energy is being lost, the luminosity L.

$$\tau_{\mathrm{H}} = \frac{E_{\mathrm{H}}}{L} \tag{1.1}$$

With each successive burning phase after H yielding less energy per gram of reactants, the timescales of the advanced burning phases become significantly shorter than the previous one. The types of energy generating reactions in stars are H, He, C, Ne, O, and Si burning, each with their own timescale and each requiring a minimum temperature to ignite. The He-core burning of the $25\mathrm{M}_{\odot}$ star lasts roughly 650 Kyr while its Si-core burning phase that lasts only around a day.

After a star depletes the H in its core during the main sequence the luminosity from the H burning decreases leading to energy being transported away from the core. This causes the star to begin to contract releasing gravitational potential energy which eventually makes it way into the form of heat keeping the star in hydrostatic equilibrium. The contraction continues to increase the temperature of the core until He burning is ignited. The collapsing of the star would occur, with the absence of any nuclear burning, over a timescale called the thermal timescale which is defined to be

$$\tau_{\mathrm{T}} = \frac{U}{L} \; \alpha \; \frac{GM^2}{LR} \tag{1.2}$$

where U is the internal energy (Kippenhahn et al., 2012). There is a factor of unity on the proportional side of the equation that depends on the thermodynamic properties of the star. In this case, the transfer of gravitational potential energy to the internal energy of the gas is fully balancing the star, keeping it in hydrostatic equilibrium and stopping it from collapsing in a free fall. During the AGB phase of the $3\mathrm{M}_{\odot}$ star, it undergoes thermal pulses from the recurring He-flashes in its He-shell. The luminosity reaches a maximum of 10^8 $\mathrm{L}_{\odot}$ causing the star to rapidly expand and cool over a thermal timescale of 100 years (Oswalt & Barstow, 2013).

After Si burning in the $25\mathrm{M}_{\odot}$ star, there are no longer any nuclear reactions that can keep the star in hydrostatic equilibrium. The star collapses so quickly that the gravitational potential energy from collapse is unable to thermally support the star and therefore it collapses in a free-fall state. This free-fall or dynamic timescale is given by Kippenhahn et al. (2012) as

$$\tau_{\mathrm{ff}} = \left(\frac{R^3}{GM}\right)^{1/2} \tag{1.3}$$

Another dynamic-like timescale is the convective turn over timescale. This measures the time it takes for a typical fluid element to advect from one end of a convection zone to the other and can be written as

$$\tau_{\mathrm{conv}} = \frac{R_{\mathrm{conv}}}{\langle v \rangle} \tag{1.4}$$

During the lifetime of a star the relevant timescales typically arrange themselves as

$$\tau_{\mathrm{n}} \gg \tau_{\mathrm{T}} \gg \tau_{\mathrm{conv}} > \tau_{\mathrm{ff}} \tag{1.5}$$

1.2.2 Stellar Structure

A set of 4 coupled partial differential equations can describe the structure of a star across its entire lifetime. These are formulated in the Lagrangian mass coordinate and are given by Kippenhahn et al. (2012) as

$$\frac{\partial r}{\partial m} = \frac{1}{4\pi r^2 \rho} \tag{1.6}$$

$$\frac{\partial P}{\partial m} = -\frac{Gm}{4\pi r^4} - \frac{\partial^2 r}{\partial t^2}\frac{1}{4\pi r^2} \tag{1.7}$$

$$\frac{\partial L}{\partial m} = \varepsilon_{\mathrm{n}} - \varepsilon_{\nu} + \varepsilon_{\mathrm{g}} \tag{1.8}$$

$$\frac{\partial T}{\partial m} = -\frac{GmT}{4\pi r^4 P}\nabla \tag{1.9}$$

where r, m, P, T, ∇, ε_{n}, ε_{ν} and ε_{g} are the radius, enclosed mass, pressure, temperature, $\nabla = \frac{d \ln T}{d \ln P}$, the nuclear energy generation per unit mass, the neutrino energy loss per unit mass and the gravitational energy per unit mass due to expansion or contraction. Equation 1.6 is a relation between the Eulerian and Lagrangian coordinates. Equation 1.7 is Newton's Second Law with hydrostatic equilibrium when $\vec{a} = 0$ (the 3D equation 1.23). Equation 1.8 is energy conservation within a star (the 3D equation 1.27) and equation 1.9 is the temperature gradient.

The temperature gradient, ∇, of a stellar region is dependent on the energy transport mechanism. The three main sources of energy transport within a star are conduction, radiative diffusion and convection. Conduction within stars is expected to be completely negligible (Kippenhahn et al., 2012) but depending on the conditions within the star, the energy is transported by radiation or convection. A star that has a radiative zone has its energy transported by radiative diffusion which has a temperature gradient of the form

$$\nabla_{\text{rad}} = \frac{3}{16\pi acG}\frac{\kappa LP}{mT^4} \tag{1.10}$$

where a, c, κ are the radiation constant, the speed of light and the opacity. A convective stratification is adiabatic and thus has the general form of

$$\nabla_{\text{ad}} = \frac{P\delta}{T\rho c_P} \tag{1.11}$$

where $\delta = (d\ln\rho/d\ln T)_{\text{P}}$ and c_{P} is the specific heat capacity at constant pressure (Kippenhahn et al., 2012). If a fluid element is heated so rapidly that it is unable to transport heat to its neighbours through radiative diffusion before it becomes buoyant, the fluid will begin to convect. This is encapsulated in the Schwarzschild criterion which states that a fluid element is stable to convection if

$$\nabla_{\text{rad}} < \nabla_{\text{ad}} \tag{1.12}$$

is satisfied. A region within a star where this criterion is not satisfied is convectively unstable.

In any stellar evolution calculations there is an additional equation to describe changes to chemical species within a star through nuclear burning and mixing. This equation is typically written in terms of a mass fraction, $X_{k,i} = m_{k,i}/dm_{k,i}$, at a cell i for a particular species, k, as written by (Paxton et al., 2010)

$$\frac{dX_{k,i}}{dt} = \left(\frac{dX_{k,i}}{dt}\right)_{\text{burn}} + \left(\frac{dX_{k,i}}{dt}\right)_{\text{mix}} \tag{1.13}$$

where the mixing term can be due to convection, rotation, gravitational waves and any other sources of mixing.

1.2.3 Nuclear Burning

Nuclear reactions that are undergone within stars are based on what species are present as well as the thermodynamic conditions. The reaction discussed commonly in this thesis is the $^{12}\mathrm{C}(p,\gamma)^{13}\mathrm{N}$ reaction, $^{12}\mathrm{C} + p \longrightarrow {}^{13}\mathrm{N} + \gamma$. The rate of change of the number density, n, of $^{12}\mathrm{C}$ due to this reaction depends on the number density of protons and the rate to which this reaction occurs. This can be written as

$$\frac{dn_{^{12}\mathrm{C}}}{dt} = -n_p n_{^{12}\mathrm{C}} \langle \sigma v \rangle_{^{12}\mathrm{C}(p,\gamma)} \tag{1.14}$$

where $\langle \sigma v \rangle_{^{12}\mathrm{C}(p,\gamma)}$ is the Maxwellian averaged reaction rate which is a function of temperature. For charged particle captures, such as a proton, the reaction rate depends sensitively on the temperature because of the Coulomb potential however for reactions that involve capturing a neutron, the reaction rate is not dependent on temperature (Kippenhahn et al., 2012). In the absence of resonances the neutron cross sections $\sigma \; \alpha \; 1/v$ (Kippenhahn et al., 2012).

The resultant nuclei from the $^{12}\mathrm{C}(p,\gamma)^{13}\mathrm{N}$ reaction, $^{13}\mathrm{N}$, is an unstable isotope. $^{13}\mathrm{N}$ has a half-life of 9.6 min and undergoes a β^+ decay resulting in $^{13}\mathrm{C}$. The rate of change in the number density of the $^{13}\mathrm{N}$ due to the beta decay is

$$\frac{dn_{^{13}\mathrm{N}}}{dt} = -n_{^{13}\mathrm{N}} \lambda_{\beta+} \tag{1.15}$$

where $\lambda_{\beta+}$ is the $^{13}\mathrm{N}$ beta decay reaction rate.

There are sources and sinks of any isotope due to reactions with other isotopes and beta decays. Even with a He-shell temperature of 275 million K the Coulomb potential prevents isotopes from capturing any charged particles other than protons and alpha particles. Generally, the rate of change of an isotope due to reactions with one other species and including beta decays is written like in Oswalt & Barstow (2013) as

$$\frac{dn_i}{dt} = -\sum_j (1+\delta_{ij})^{-1} n_i n_j \langle \sigma v \rangle_{ij} + \sum_{k,l} n_k n_l \langle \sigma v \rangle_{kl} - \lambda_i n_i + \sum_m \lambda_m n_m \tag{1.16}$$

A nuclear burning timescale for the loss of a particular isotope can be written in the case that there is only one reaction. For the $^{12}\mathrm{C}(p,\gamma)$ reaction in a He-shell, there is so much $^{12}\mathrm{C}$ that the reaction is limited by the number of protons. The timescale for a proton to be captured by a ^{12}C is

$$\tau_p = \frac{1}{n_{^{12}\mathrm{C}} \langle \sigma v \rangle_{^{12}\mathrm{C}(p,\gamma)}} \tag{1.17}$$

1.2.4 Convective Mixing

The dominant source of mixing within stars is due to convective motions. Physically, within the convection zone material is being advected and can undergo nuclear reactions while it is being transported. Since the convective motions operate on a timescale close to the dynamic timescale of a star, in many cases the homogenization of species within a convection zone can be considered instantaneous if there is little burning over the mixing timescale. A more accurate scheme for modeling the mixing over nuclear timescales, though not physically motivated but rather out of numerical convenience, is for the convective mixing to be described as a diffusive process. With the assumed spherical symmetry, the mixing of a species, k, in the Eulerian coordinates is given by

$$\left(\frac{dX_{k,i}}{dt}\right)_{\mathrm{mix}} = \frac{\partial}{\partial r}\left(D_i \frac{\partial X_{k,i}}{\partial r}\right) \tag{1.18}$$

where D_i is the diffusion coefficient in cell i. This is the diffusion equation and it has several properties that make it very useful in the stellar evolution context. The solutions to these equations over many diffusive timescales, $\tau_D = \ell^2/D$ (ℓ is the length scale of the system), is that the mass fraction approaches a flat profile in the absence of sources of $X_{k,i}$. The equation behaves such that the *flow* of species always goes from areas of high concentration to low concentration. There is no diffusive process that does not smooth and flatten the profile of the species being diffused. In the numerics, the diffusion equation can be solved with an implicit formulation, even over nuclear timescales.

To obtain a diffusion coefficient within a convection zone requires an estimate of the velocity profile within that convection zone. This is because the random motions of particles with a characteristic velocity over a mean free path will diffuse (Carter, 2001) with a diffusion coefficient of

$$D = \frac{1}{3} v \ell \tag{1.19}$$

The velocities of the fluids in the convection zone are estimated using the mixing length theory (MLT). The details of this model are formulated in Cox & Giuli (1968) but the idea of MLT is that a fluid element is advected a mixing length, ℓ, through the convection zone adiabatically until it looses its identity and mixes with the surrounding medium. For a given luminosity and stratification, there is an associated mean velocity at every radius for the convective fluid. The mixing length cannot be determined theoretically and so it is a free parameter in stellar evolution models. It is constrained semi-empirically, through fitting stellar populations in open and globular clusters for various mixing lengths as well as the Sun (Kippenhahn et al., 2012), to be

$$\ell = \alpha_{\mathrm{MLT}} \left(d \ln P / dr\right)^{-1} \tag{1.20}$$

where $\alpha_{\mathrm{MLT}} = 1.6$ is the mixing length parameter and $\left(d \ln P / dr\right)^{-1}$ is the local pressure scale height.

It is of course more ideal to model the mixing in the convection zones of stars by using an advective scheme because that is how material is physically transported. By applying the conservation of mass (in 3D, equation (1.22)) and the definition of a mass fraction, the advective mixing equation for each species, k, is

$$\frac{\partial \left(\rho X_k\right)}{\partial t} + \vec{\nabla} \cdot \left(\rho X_k \vec{u}\right) = 0 \tag{1.21}$$

This equation has a very different behaviour compared to equation 1.18. There is no bounded long term behaviour of the solutions to this equation, material can advect within the rigid walls of the simulation and there is no guarantee of a flat profile over long periods of time. Material can flow from areas with low concentration to areas with high concentration and vice versa. It is also the physically correct transport mechanism for fluids within the convection zone.

Advective mixing is not used in stellar evolution calculations because of the numerics required to solve these equations. The numerics are typically formulated as flux conservative methods which require explicit integration in conjunction with a timestep constraint (see Section 1.4 and Section 3.3.3.3) and thus immediately stops any chance of its use across general stellar evolution computations. This is simply because of the timescales involved.

Because of the implicit formulations of the diffusion equation, the diffusion approximation is used for all forms of mixing in stellar evolution codes such as `MESA` (Paxton et al., 2010) and many nucleosynthesis post-processing codes such as `mppnp` (Herwig et al., 2011). Diffusion works well for most scenarios encountered across stellar evolution however the approximations taken to assume that convective mixing can be modeled with diffusive mixing are broken when the mixing (equation 1.4) and burning timescales (equation 1.17) become equal. This is quantified with the Damköhler number being equal to 1 ($\mathrm{Da} = \tau_{\mathrm{conv}}/\tau_{\mathrm{react}}$; Dimotakis, 2005). With energy feedback from the burning and a Damköhler number of 1, the hydrodynamic regime is convective-reactive (Herwig et al., 2011) and so the details of the interaction of the burning and the feedback into the flow of the fluid (mixing) on dynamic timescales (see Section 1.4.4) become important to characterize the evolution and nucleosynthesis within that convection zone.

A common scenario in which $Da \approx 1$ is when there is mixing of H into a convective He-shell. The plentiful ^{12}C and He-burning temperatures cause the $^{12}\mathrm{C}(p,\gamma)^{13}\mathrm{N}$ reaction to burn all of the H well within a convective turn over time, τ_{conv}. The H-ingestion scenario is found across many different stars in different phases of evolution. These include the H-shell burning phases of Pop III stars (Clarkson et al., 2017), He-shell flashes of the RAWDs of Denissenkov et al. (2017), and in the post-AGB star, Sakurai's Object (Herwig et al., 2011).

The uncertainty in modeling the convective-reactive H-ingestion scenarios with diffusive mixing is that the hydrodynamic instabilities that entrain the flammable H occur on dynamic timescales in conjunction with the burning. The energy feedback can be substantial enough to drive large non-radial oscillations within the star (see Section 1.4.4). The idea that the mixing and transport of this material through the convection zone is diffusive when considering that it completely burns in less than a convective turn over timescale through advective transport is physically wrong.

Another example of a convective-reactive environment is from pre-supernova O-shell simulations. The 3D simulations of Yadav et al. (2019) show that the energy feedback from the entrainment of Ne is dramatic enough to cause large scale oscillations that can help with shock revival of core collapse supernovae (CCSN). The 1D models that contain convective boundary mixing show a more stable and slow burning with energetics that do not suggest large scale oscillations.

1.3 RAWD and the *i*-process

For a carbon-oxygen (CO) white dwarf (WD) in a compact binary with another star in a less evolved state, H-rich material from that star can be accreted onto the WD. The RAWD is a WD in which the rapidly accreted H is burned stably on the surface of the WD (Denissenkov et al., 2017). The H burning leaves He ashes behind which will eventually undergo He burning. The subsequent He-flash that occurs disrupts the H burning on the WD surface but also causes ingestion of H into the He-shell (Fig. 1.1). The He-flash causes the WD to lose most of the accreted material through common envelope interactions or stellar winds. The efficiency to which the He-shell material is able to be retained onto the WD is under 20% (Denissenkov et al., 2019) leading to most models being unable to reach the Chandrasekhar mass. After the He-flash event, the WD eventually contracts and accretes H from its binary partner once again.

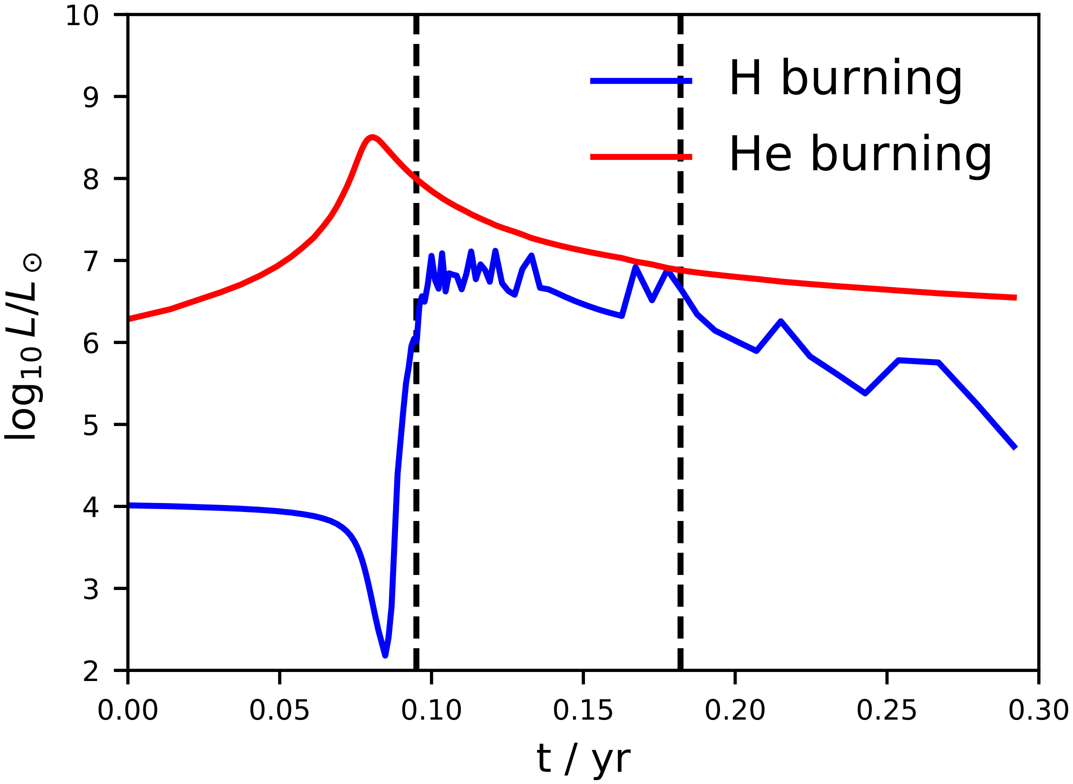

Figure 1.1: The H and He luminosities during a He-flash in the RAWD, model G, of Denissenkov et al. (2019) and the H-ingestion event immediately after. The bulk of the H-ingestion occurs over a single month which is shown between the black dashed lines.

The repeating He-flashes in RAWDs leads to many H ingestion events into the He-burning shell. One such He-flash and H-ingestion event is shown in Fig. 1.1. The temperatures are high enough such that the $^{12}\mathrm{C}(p,\gamma)^{13}\mathrm{N}$ occurs and burns all of the

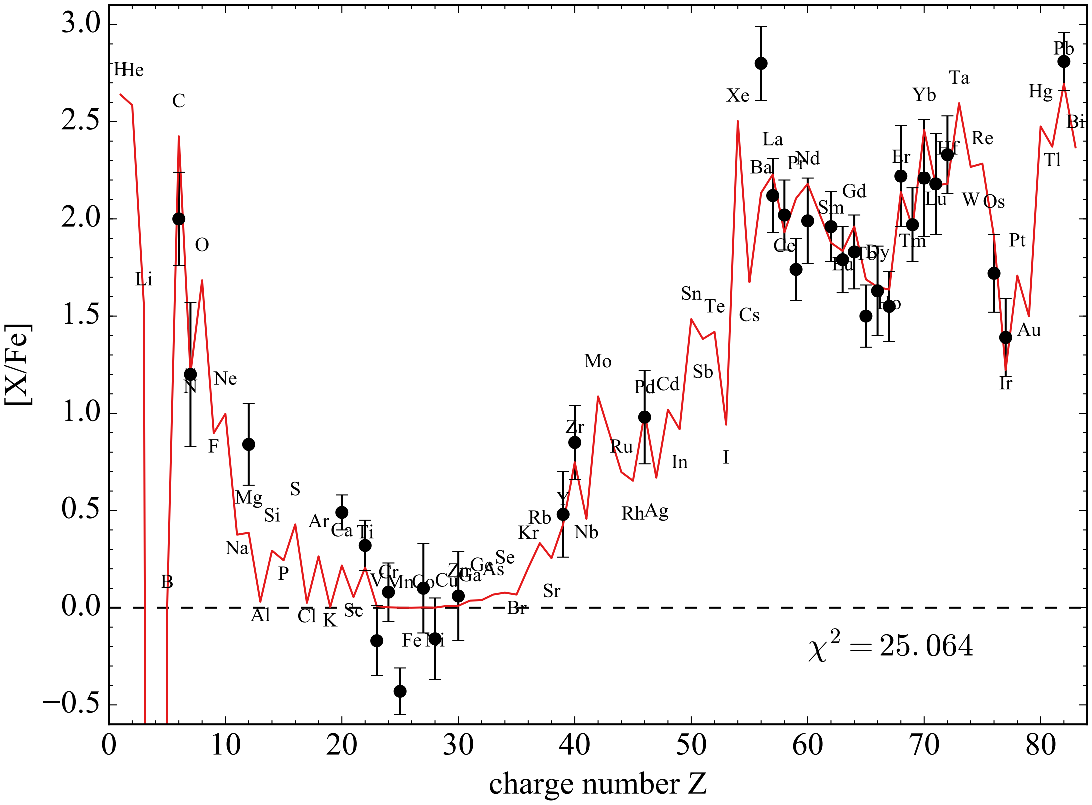

Figure 1.2: The i-process material of model G from Denissenkov et al. (2019) is diluted and fit to the observations of the CEMP-r/s CS31062-050 (Iwamoto et al., 2004; Johnson & Bolte, 2004).

H that is ingested. The subsequent reactions, ^{13}N$(\beta^+)^{13}$C and ^{13}C$(\alpha, n)^{16}$O, release neutrons into the convection zone at number densities of $N_n \approx 10^{14}\,\mathrm{cm}^{-3}$ which is within the i-process regime. With this material being able to escape from the WD and the fact that this type of binary system is common within the galaxy leads to estimates of the RAWD contributing significantly to the solar abundance distribution for Mo and other elements as discussed in Côté et al. (2018).

There are 3 different regimes of neutron capture processes that each have their own associated isotopic abundance distribution which are the s-process, the i-process and the r-process. The s-process typically has neutron densities of $N_n \approx 10^6 - 10^{10}\,\mathrm{cm}^{-3}$ and its main astrophysical source is within AGB stars while the r-process has neutron densities of $N_n > 10^{20}\,\mathrm{cm}^{-3}$. The only observationally confirmed site of the r-process is from neutron star mergers (Abbott et al., 2017). The i-process occurs with neutron densities of $N_n \approx 10^{13} - 10^{16}\,\mathrm{cm}^{-3}$ but the astrophysical sites of this nucleosynthesis are not certain. The mixture of metals from the s-process and r-process can explain most of the Suns elemental abundance pattern however they cannot explain certain elemental ratios observed in subclasses of carbon-enhanced metal poor (CEMP) stars.

The CEMP stars are Pop II stars that formed from H gas clouds with sub-solar metallicity. Since they are metal poor and have $[\mathrm{Fe/H}] \leq -2$, the metals that are within those gas clouds at formation are expected to have only come from a few metal-enriching events. The observations of these stars allows for testing whether certain nucleosynthetic sites/neutron densities are responsible for the observed elemental abundance patterns. The i-process nucleosynthesis of the RAWD model G from Denissenkov et al. (2019) is able to explain most of the elemental abundance features of the CEMP-r/s star CS31062-050 except for Ba (Fig. 1.2).

1.4 3D Stellar Hydrodynamics

One of the largest uncertainties in stellar evolution calculations and the nucleosynthesis calculations from those models is due to the treatment of convective mixing. In the near dynamic timescales of He-flashes a convection zone develops and expands in mass. These He-flash convection zones occur periodically in RAWDs but also within AGB stars. To efficiently produce the s-process within AGB stars, additional convective boundary mixing (CBM) not predicted by MLT was needed (Herwig, 2000). The CBM can influence the late-stage evolution of massive stars dramatically due in part to the additional fuel that is used for burning as seen in the models of Davis et al. (2019). To better understand how the interactions of the hydrodynamics within stellar convection influence the stably stratified material and the subsequent mixing of said material in the convection zone, 3D hydrodynamic simulations are used.

1.4.1 3D Hydrodynamic Equations

The hydrodynamic equations that the 3D hydrodynamic code that is used for this thesis, `PPMstar`, will solve are formulated based on three conservation laws; the conservation of mass, momentum and energy for a fluid. These are typically derived and written in the Lagrangian frame of the fluid, the frame in which at any time the velocity of the fluid is zero. The conservation of mass is given by

$$\rho_t + \vec{\nabla} \cdot (\rho \vec{v}) = 0 \tag{1.22}$$

where $\vec{v}$ is the velocity. The conservation of momentum, in a general form, is given by the Cauchy equation (Kundu et al., 2012)

$$\rho \frac{D\vec{v}}{Dt} = \rho\vec{g} + \vec{\nabla} \cdot \tau \tag{1.23}$$

where $\vec{g}$ is the gravitational field and τ is the stress tensor. This equation is a direct consequence of applying Newton's Second Law to a moving fluid volume. The $\frac{D}{Dt}$ operator is the advective derivative and can be transformed to the Eulerian frame with

$$\frac{D}{Dt} = \frac{\partial}{\partial t} + \vec{v} \cdot \vec{\nabla} \tag{1.24}$$

The `PPMstar` simulation solves the Euler hydrodynamic equations which is an approximation of the Cauchy equation where there is no viscosity and the only surface stresses on a fluid are due to the thermodynamic pressure. This reduces equation 1.23 to

$$\rho \frac{D\vec{v}}{Dt} = -\vec{\nabla} p + \rho\vec{g} \tag{1.25}$$

$$\frac{\partial \vec{v}}{\partial t} + \left(\vec{v} \cdot \vec{\nabla}\right) \vec{v} = \frac{-1}{\rho} \vec{\nabla} p + \vec{g} \tag{1.26}$$

which is exactly hydrostatic equilibrium in 3D when $\frac{D\vec{v}}{Dt} = 0$ (1D equation 1.7).

The total energy density of the fluid includes the sum of the kinetic, internal and gravitational potential energy densities as

$$E = \rho \left(\frac{1}{2} \left\| \vec{v} \right\|^2 + \Psi + \varepsilon \right) \tag{1.27}$$

where Ψ is the gravitational potential energy per unit mass and ε is the internal energy per unit mass. With no viscosity and no heat conduction, the energy conservation equation stated by Clarke & Carswell (2007) with a constant gravitational field is

$$\frac{\partial E}{\partial t} + \vec{\nabla} \cdot \left(\left(E + p \right) \vec{v} \right) = \rho \frac{\partial q}{\partial t} \tag{1.28}$$

where q is the heat added per unit mass. To close the system there is an equation of state relating the pressure, density and temperature as well as the internal energy to those state variables.

1.4.2 `PPMstar` Simulations

The Euler and energy equations are discretized and solved on a cubic, Eulerian grid, in the `PPMstar` simulations. The typical number of cells is 768^3 while the important science runs have a grid of 1536^3 cells. The hydrodynamics are solved with the Piecewise-Parabolic Method (PPM; Colella & Woodward, 1984; Woodward, 1986, 2007; Woodward & Colella, 1981, 1984). Special care is taken when advecting the species, FV, as a higher order scheme, the Piecewise-Parabolic Boltzmann method (PPB; Woodward, 1986; Woodward et al., 2015) is used.

Although the Euler equations are considered to be unrealistic for most terrestial applications due to the fact that viscosity is always present, the fluids in the interior of stars have Reynolds numbers greater than 10^{16} (Kippenhahn et al., 2012), which is essentially zero viscosity ($\mathrm{Re} = \rho v L/\mu$). The discretization of the numerics contain terms that effectively act like viscosity by dissipating kinetic energy. This artificial viscosity dissipates the energy at the grid scale which is consistent with simulations including an explicit viscosity (Porter & Woodward, 1994). These properties allow for realistic simulations of the convective fluid in the deep interiors of stars.

The PPM method is a flux conservation method for solving the hydrodynamic equations and so it is integrated explicitly. Every explicit hydrodynamic method has a time step criterion to ensure numerical stability, the Courant condition, that must be satisfied for every step. The Courant condition can be plainly stated as requiring that the propagation of a wave in a single time cannot travel further than one grid cell. Mathematically, the Courant number

$$\mathrm{C} = \frac{v\delta t}{\delta x} \tag{1.29}$$

must always be less than 1. This severely limits the size of the timesteps that the simulation can take. The `PPMstar` simulations can only feasibly model a star for 10's of convective turn over times which is a small fraction of the thermal timescale for any given simulation.

The `PPMstar` code contains two different fluids with different mean molecular weights, μ, that come into contact with each other. With the scientific interest of the mixing between stably stratified and convective material, the `air` fluid ($\mathcal{F}_2$) is designated within the convection zone while the `cld` fluid ($\mathcal{F}_1$) is the stably stratified material above it. At some radius, the two fluids mix together in the transition region. When the two fluids meet, they immediately come into thermal equilibrium and each fluid occupies a certain percentage of the volume of that cell. The fractional volume (FV) refers to the fraction of the volume of that cell that is occupied by the $\mathcal{F}_1$ fluid. For an ideal gas equation of state,

$$P = \frac{R}{\mu}\rho T \tag{1.30}$$

where $R = k_\mathrm{B}/m_u$ is the gas constant, the mass fraction of the $\mathcal{F}_1$ fluid is related to the FV as

$$X_\mathrm{cld} = \frac{\mathrm{FV}}{\left(\mathrm{FV} + (1-\mathrm{FV})\frac{\mu_\mathrm{air}}{\mu_\mathrm{cld}}\right)} \tag{1.31}$$

To realistically model a convection zone and the surrounding media, the `PPMstar` simulations need to model the stratification of the star accurately. To this end, the `PPMstar` simulations model the outside of a convection zone with a polytropic stratification,

$$P = K\rho^\gamma \tag{1.32}$$

where $\gamma > 1$ and K is a constant. The polytrope allows the `PPMstar` stratification to closely follow the original stellar evolution models stratification more closely which includes a more general equation of state (radiation pressure, degeneracy pressure, etc.) (Jones et al., 2017). For an ideal gas, the adiabatic stratification given by equation 1.11 is a polytrope with $\gamma = 5/3$ for the monatomic gas.

1.4.3 Scaling Laws

In order to drive convection there must be a heat source near the bottom of the convection zone. From the stellar evolution models this is calculated from nuclear burning but in the `PPMstar` simulations the nuclear burning is modeled with constant volume heating. For the simulations presented in this thesis, the luminosities of the RAWD are approximately 10 times larger than the nominal luminosity from the original stellar evolution model. This is a numerical limitation of the `PPMstar` simulations as the Mach number,

$$\mathcal{M}a = \frac{v}{c_s} \tag{1.33}$$

where c_s is the sound speed of the medium given by,

$$c_s = \sqrt{\left(\frac{\partial P}{\partial \rho}\right)_S} \tag{1.34}$$

of the flow would be too low. With such a slow flow, the simulations would have to be run longer to move to a quasi-static state and any numerical effects, such as alignment of the flow along the axes, become more pronounced.

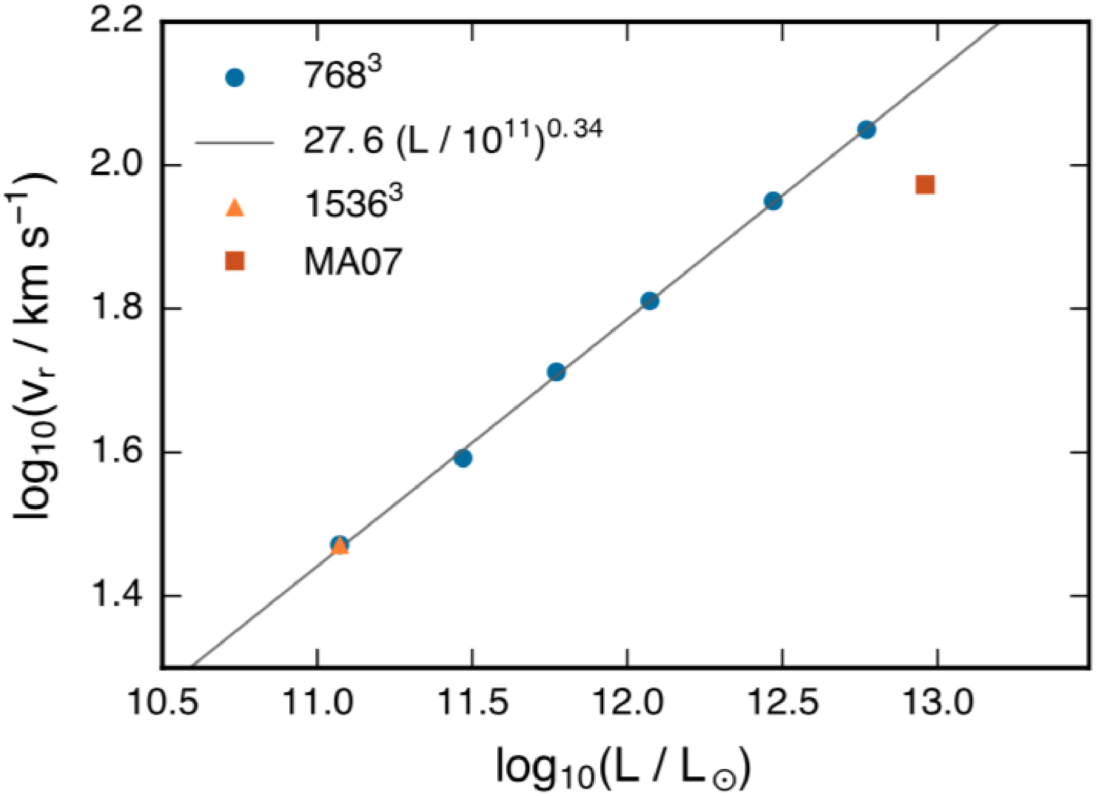

Figure 1.3: Figure 13 from Jones et al. (2017) showing the relationship of the rms of the radial velocity and the luminosity to the one third power ($v \ \alpha \ L^{1/3}$). This relationship spans over two orders of magnitude in this work. MA07 refers to the work by Meakin & Arnett (2007).

Although the simulations have significantly larger than nominal luminosities, many of the quantitative properties calculated can be scaled back to the nominal luminosity through scaling laws. A scaling law that has been theoretically and experimentally suggested is that $v \ \alpha \ L^{1/3}$ (Biermann, 1932; Jones et al., 2017; Müller & Janka, 2015; Porter & Woodward, 2000). This scaling law is quantitatively shown to

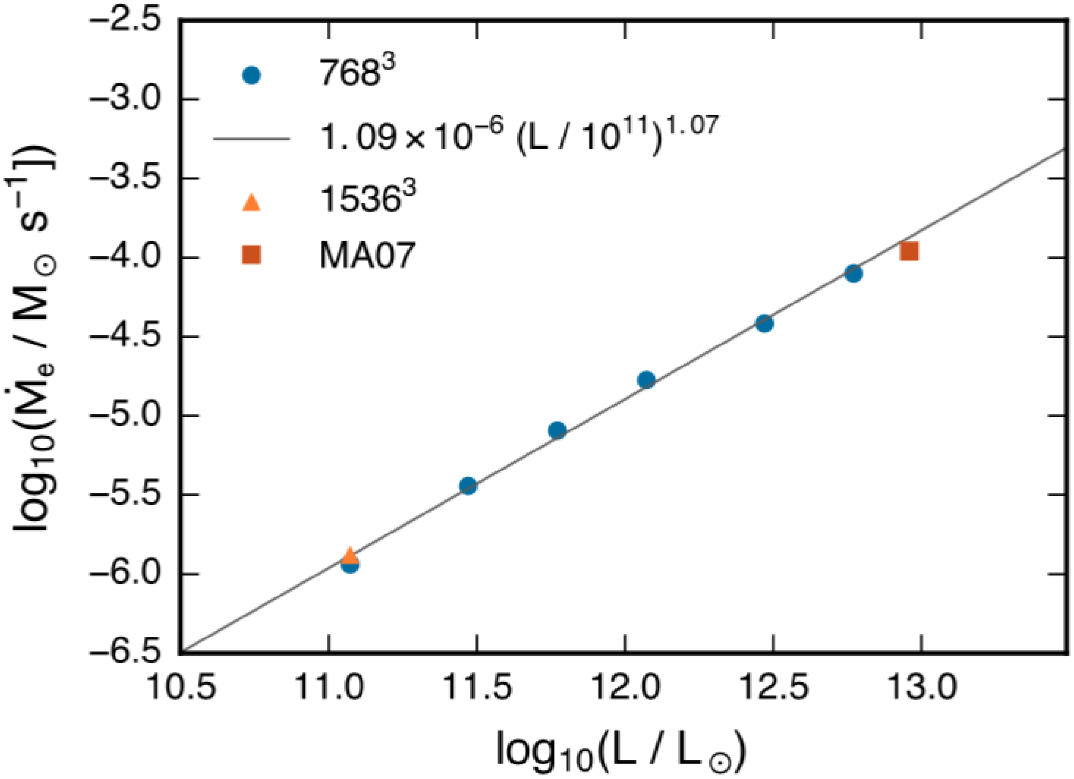

Figure 1.4: Figure 19 from Jones et al. (2017) showing the linear relationship between the entrainment rate and driving luminosity which spans over two orders of magnitude. There is no burning between the two fluids in these simulations. MA07 refers to the work by Meakin & Arnett (2007).

be true for the no burning O-shell simulations of Jones et al. (2017) (Fig. 1.3), and from the simulations of C-ingestion into an O-shell with C-burning from Andrassy et al. (2018) for `PPMstar` simulations. Another important scaling law is that the entrainment rate of the stably stratified fluid into the convection zone scales with the luminosity (Fig. 1.4). This occurs even in cases with explicit nuclear energy generation from a reaction network like the C-ingestion of Andrassy et al. (2018) and the RAWD simulations of Denissenkov et al. (2019) so long as the luminosity from that burning is significantly smaller than the background volume heating. Any velocities and entrainment rates from these high luminosity simulations can be scaled down to a nominal luminosity for a realistic advective or diffusive post-processing of the RAWD.

1.4.4 Global Oscillations of Shell H-ingestion (GOSH)

In the convective-reactive environment of Sakurai's Object, Herwig et al. (2014) computed 3D hydrodynamic simulations of the He-flash convection zone and its entrainment of stably stratified H. With the inclusion of the $^{12}\mathrm{C}(p, \gamma)$ reaction and its energy feedback into the system, the initially quasi-static H entrainment, for $\approx$ 850 min, abruptly increased. At this time, strong opposing horizontal flows converged near the convective boundary causing a downdraft that entrained H from the H-rich layer above the convective boundary. The burning of this H leads to large amounts of energy released back into the flow triggering new strong flows that again meet at the stiff convective boundary and entrain more H. These repeating global oscillations are captured in the root-mean-square (rms) radial velocity profiles in Fig. 1.5. These repeating oscillations are eventually damped and stopped from the massive ingestion of high entropy fluid (Herwig et al., 2014) which brings the convective flow back to quasi-static burning. This occurs in the lower resolution simulation that was run longer as seen in Fig. 1.5. The dramatic time-dependent behaviour of entrainment, changing the H burning location and mixing properties of the convection zone and the energy feedback from such events are not taken into account in 1D stellar evolution models nor the nucleosynthesis post-processing of such models as they do not predict such events. The ability for 1D diffusive mixing to model the dynamic and 3D nature of such events are easily questioned.

1.4.5 3D1D Nucleosynthesis

In principle, the nucleosynthesis within a convection zone could be computed directly in the 3D hydrodynamic simulations however there are two major limitations to doing this. One of these is due to the computational work needed. To model the *i*-process thousands of species are needed because of how neutron-rich the material can get. Within the `PPMstar` simulations these species would need to be advected independently and if they were to be advected with the same fidelity as the species included right now it would require 1000's of times more advective calculations making the code 1000's of times slower. This also directly increases the memory usage close to a factor of 1000. The amount of data that these simulations would be outputting is completely unfeasible (see Section 2.1). Another reason is that although the details of the neutron density depend sensitively on the convective-reactive burning, the H-ingestion event in the RAWD occurs over a month. Currently a 1536^3 simula-

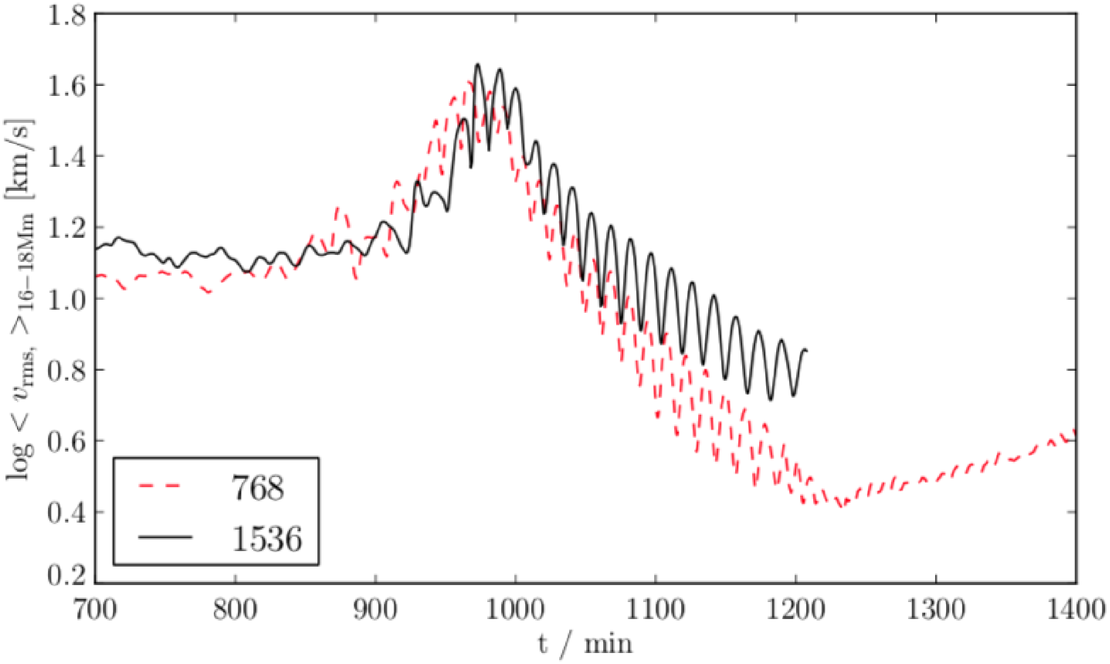

Figure 1.5: Figure 2 from Herwig et al. (2014) showing the rms velocity as a function of time in two simulations differing in resolution. Major oscillations occur around $t = 900$ min that are propagated similarly in both simulations. The 768^3 simulation is run longer and returns to quasi-static burning.

tion, using a standard amount of computational effort, is able to compute 10 hours of star time. With the Courant condition causing the hydrodynamic simulations to be tightly constrained by dynamic timescales, even with only advecting two species, the i-process nucleosynthesis timescale of the RAWD is well out of reach of current supercomputers.

In another field, CCSN, a diffusive-like modeling approach is commonly used. Lagrangian particles are scattered across the 2D or 3D hydrodynamic simulations with the nucleosynthesis being directly computed on them. The hydrodynamic solvers then advects these particles which are tracked and used as a tracer for the nucleosynthesis that happens during a core collapse. This requires significantly less computational effort than explicitly advecting fluids as in `PPMstar`. However Harris et al. (2017) used these particles and compared it with the nucleosynthesis being computed on their hydrodynamic grid directly. The resulting electron fractions of the ejected material, elemental abundance patterns, are wildly varying between the diffusive-like approach with varying number of particles and directly computing the nucleosynthesis on the grid. They also note that there are large uncertainties due to the small networks that must be used in order to compute the CCSN in a reasonable amount of computing time.

Another type of reduction in complexity to compute nucleosynthesis within stars is to use 1D modeling like the stellar evolution models of Section 1.2.2. `mppnp` (Herwig et al., 2011) is a 1D post-processing code that takes 1D stellar evolution models, calculates the nucleosynthesis of 1000's of species if needed and mixes them using a diffusive mixing routine. The accuracy of applying diffusive mixing to describe the dynamic convective-reactive environments of the RAWD and especially in the GOSH environment of Sakurai's Object is uncertain. There has been work done to include a 1D advective mixing scheme into nucleosynthesis calculations from the works of Cannon (1993) and Henkel et al. (2017). Their 1D advective mixing scheme, to which the model of Chapter 3 expands and improves on, uses the velocities estimated from MLT for their mixing coefficients rather than using 3D hydrodynamic simulations. They also assume that the mixing between the two streams (see Fig. 3.1) will have some associated mixing length that determines the rate to which mass is transferred between them. There is no physical motivation for what this mixing length could be. Their models, although numerically they are advective, do not take into account the general behaviour of 3D hydrodynamic flow within stellar convection zones (see Section 3.4.1.1) for calibrating their mixing coefficients or for justifying the physical motivation of using such a constrained model (see Section 3.3.3).

1.5 Goals of This Work

One of the goals of this work is to create a 1D advective mixing routine that is able to use the hydrodynamic mixing information from the 3D `PPMstar` simulations to inform its mixing parameters. The 1D advective mixing model will be applied to a RAWD from Denissenkov et al. (2019) where it is expected that no GOSH or large asymmetric perturbations will occur while the H is ingested. This makes the RAWD model an ideal test case for quantifying how the advective mixing routine will behave in a quasi-static environment where diffusive mixing is normally applied. There is also the fact that the resulting nucleosynthesis of the RAWD models are well understood. The numerical techniques needed to utilize the 3D hydrodynamic information from `PPMstar` for the advective mixing model is presented in Chapter 2. Chapter 3 discusses the formulation of the 1D advection model and its application on the RAWD. It verifies the mixing routines ability to accurately follow the mixing conditions in time using the `PPMstar` simulations as the realistic model of the RAWD mixing. The advective mixing model is finally applied with a large network capable of modeling the *i*-process and it is compared with a typical diffusive mixing model in Chapter 4. The conclusions and summary of this work are stated in Chapter 5 while some additional future applications of this work are discussed in Chapter 6.

2

Numerical Tools For `PPMstar` Data Outputs

In order to complete the work of Chapter 3 there are a number of important numerical details about the data sets that were used. These details are covered in this chapter.

2.1 `PPMstar` Data Outputs

While the `PPMstar` code is running a simulation, thousands of time steps pass by before a single *dump* of data is written to disk. The reason for this is due to how inefficient the code would be if it wrote every single time step to disk as well as the volume of data that would be written. The run `N16` has 1536^3 cubical cells and over the simulation time it had taken 2,362,020 time steps with only 1,143 *dumps* of data being written to disk. If `PPMstar` had written 10 quantities at single precision (32 bits) at the full resolution of the simulation (the FV, P, and ρ are at twice that resolution in the numerics), it would require approximately 145 Gb of disk space if it was written in a binary format. Due to the impossibility of saving this kind of data even over the number of *dumps* of the simulation, `PPMstar` outputs 3 different kinds of compressed scientific data: the *bobs*, *briquettes* and *rprofs* data sets. It also outputs *restart* files to restart the simulation from a dump. The details of each compressed scientific data types are discussed throughout this section but a summary of each is in Table. 2.1

During a `PPMstar` run, there are renderings of 10 quantities from a chosen vantage point in the simulation at every *dump*. The *bobs* data is output so that renderings of those quantities can be done again in the future. For this reason, the *bobs* data is at the full resolution of the simulation but the quantities are scaled to 8 bit integers. The 8 bit integers are sufficient for making high quality colour images. By scaling it from 32 bit floating point numbers to 8 bit integers, the *bobs* data output results in a

Table 2.1: The three compressed scientific data types from the `PPMstar` simulations.

Data Type	Resolution[a]	Data Precision	Size In Memory[b] (Mb)
bobs	1536^3	8 bit signed/unsigned integer	≈ 3600
briquette	384^3	32 bit float	≈ 226
rprofs	1536 or 3072	32 bit float	≈ 0.002 or 0.004

Notes: [a] The data type resolution with respect to a `PPMstar` simulation of resolution 1536^3; [b] For only one quantity of that data type

compression factor of 4 compared to outputting the information at single precision.

The *briquette* data is used to obtain 3D information of the simulation at single precision. The compression of the data is done by averaging within a 4^3 cell (*briquette* cell) leading to an effective resolution 4 times smaller in each direction than the simulation. This results in a compression factor of 64 from the original simulation per quantity. There are 32 quantities output to disk which involve different types of averaging. For example the *briquette* data has an output, $|v|$, which is an average of the magnitude of the velocity within a *briquette* cell. This would of course be different from determining the average of the magnitude of the velocity by the magnitude of the *briquette* averaged cartesian components of the velocity, v_x, v_y, v_z.

The *rprofs* data is an ASCII file output containing spherical averages of quantities as a function of radius. There are many different quantities that are output in this format because the disk space it uses is negligible and its computation is simple even with memory being distributed over many nodes. The FV, P and ρ have their spherical averages computed at double the grid resolution. Most calculations use the *rprofs* rather than the *briquette* data because it has the same radial resolution as the simulation. This is shown to be very important in subsequent sections as most thermodynamic quantities only have small perturbations from their spherical average.

The *rprofs* data has already been established as the scientific data set for the `PPMstar` simulations using tools written in *python*. I had taken on the task of creating a *python* interface for the *briquette* data which was required to complete the work discussed in Chapter 3.

2.2 Extracting 3D Information From The *Briquette* Data

For the rest of the chapter I will reference two 3D hydrodynamic simulations of the RAWD that are discussed extensively in Chapter 3. These are `N15` and `N16` which have grid resolutions of 768^3 and 1536^3, respectively. They are identical in every other way, heating, stratification, etc. For the discussion of the properties of the *briquette* data, they depend heavily on the resolution and so `N16` is the high resolution run with a *briquette* data cube of 384^3 while `N15` is the low resolution run with a *briquette* data cube of 192^3. Other details are available for these runs in Table 3.1.

To utilize the *briquette* data, only 10 of the 32 different quantities are saved into a binary file leading to a total memory cost of ≈ 2.3 Gb per *dump* for a 1536^3 run. This is at the limits of what a single thread in *python* can handle in a reasonable amount of time for data exploration. The most important quantities are x_c, the x-coordinates of the center of the cell to which the *briquette* data was averaged over, P, ρ, FV, and the cartesian components of the velocity v_x, v_y, v_z. These are formally the average of the `PPMstar` quantity at (x_c, y_c, z_c) within a region of 4^3 cells. Even with the limited amount of quantities being read in, many other quantities can be derived from these including the spherical components of velocity, temperature and mass fractions of the $\mathcal{F}_1$ and $\mathcal{F}_2$ fluids (see Section 3.3.1 for a description of these fluids).

To test the quality of the *briquette* data, it is useful to compare it to the *rprofs* data. By creating spherically averaged radial profiles of quantities with the *briquette* data, it should correspond exactly to a lower resolution version of the *rprofs* data. The `PPMstar` simulation computes radial profiles through binning. Every cell determines which radial bin it is in, the size of each bin being determined by the resolution of the simulation, and then contributes its value to that average. This is a crude method however it is used because it only requires local information and almost no operations other than searching for what bin a particular cell is within and summing. The fact that it is a local method is very important for the `PPMstar` simulations because the entire simulation box is spread out across 544 computing nodes for `N16`. MPI messaging between the nodes significantly slows down the simulation and so whenever possible, `PPMstar` will use methods that only require local information to that particular node. Using this binning technique the radial profiles of the *briquette* data are compared with the *rprofs* data for 3 different quantities, the FV, ρ and $|v|$. These are shown in Fig. 2.1. The *briquette* radial profiles are consistent with the *rprofs*.

Stars are spherical and so with the *briquette* data being in a cartesian grid format it is not useful for anything other than taking sliced images but the *bobs* data would be more suitable for this. However, plotting quantities on the surface of a sphere can show its distribution on the sphere. A simple way to do this is to use the binning

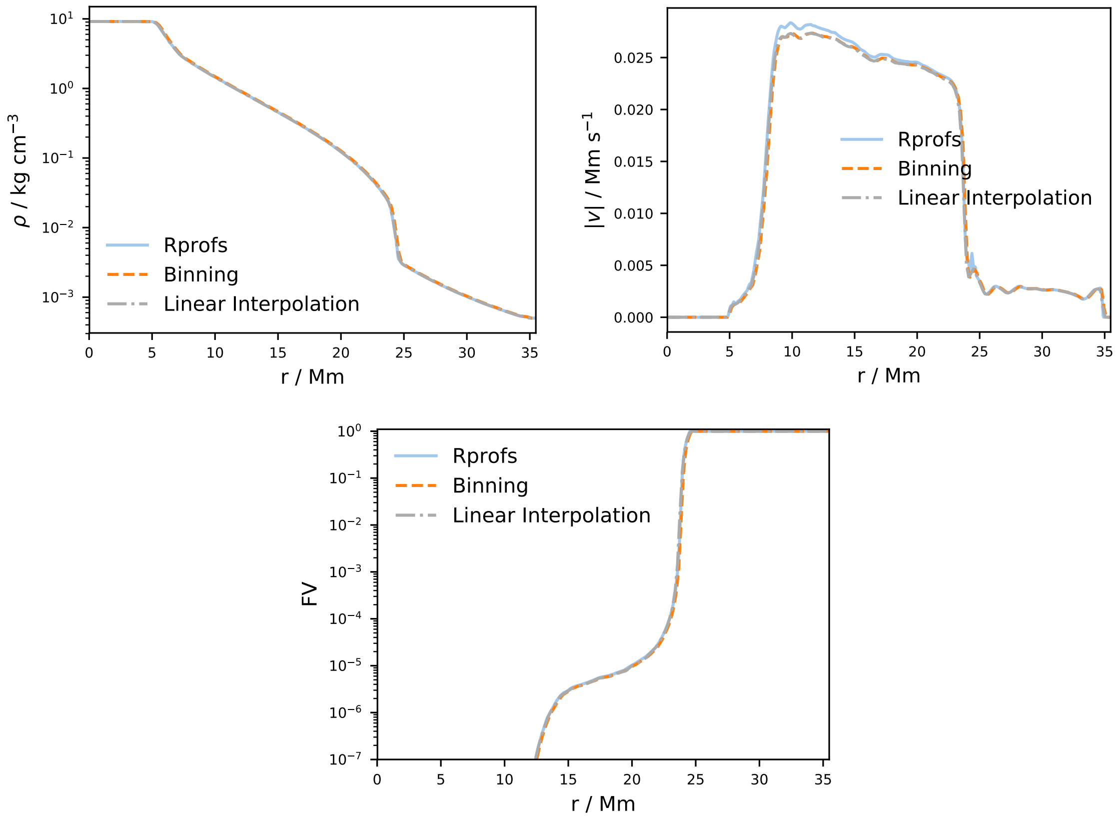

Figure 2.1: The spherically averaged radial profiles of 3 different quantities using the *rprofs*, the *briquette* binning technique (see Section 2.2) and the *briquette* linear interpolation technique (see Section 2.2.1). The three quantities are the ρ, $|v|$ and FV starting at the top left panel to the top right panel to the bottom panel, respectively. The data was taken from run `N16` at $t = 299$ min.

technique to define the quantity at a particular radius but then use each cells θ and ϕ coordinates to plot them in a mollweide projection. The density near the bottom of the convection zone is plotted in Fig. 2.2. Even with the high resolution of 384^3 there are significant numerical artifacts in the image. Because the density is very close to being spherically symmetric, the differences in the radius of the cells that are within a radial bin are significant enough to change the density by 10%. This technique is sufficiently accurate for a radial profile as the average is still represented but it is very poor for understanding the distribution of quantities on spheres. Another issue with this method is that the surface area coverage of the cells that were used to make the plot are not even. This can cause misleading surface plots as the plotting method uses area-filling triangles around every point to draw a face with a corresponding

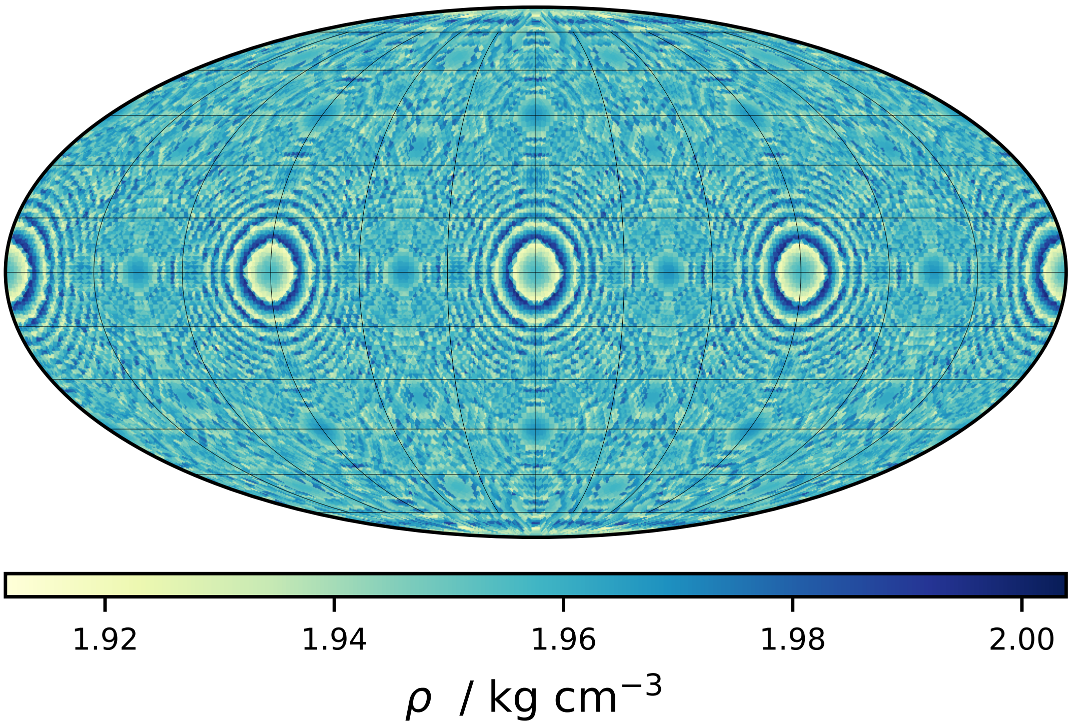

Figure 2.2: The mollweide projection of the density from `N16` at a radius of 9 Mm at $t = 299$ min using the binning technique described in Section 2.2. There are significant numerical artifacts from this technique that affect the spatial distribution of the density on a sphere.

colour. These triangles will be much larger around the poles than the triangles near $\theta = 45°, 135°$ although this is hardly noticeable unless a small sample of them is used. The simplest technique to more accurately get quantities on the surfaces of spheres is to use interpolation.

2.2.1 Linear Interpolation

Since many quantities of interest are roughly spherically symmetric even in the `PPMstar` simulations, a more accurate method than the binning method is needed to determine their distribution on a sphere. The simplest method would be a linear interpolation. With the fact that the `PPMstar` simulation has a regular grid, i.e the cells are cubic, the complexity of computing a linear interpolation is drastically reduced. The *scipy.interpolate.RegularGridInterpolator python* function is used to do the actual interpolations to the points. A qualitative description of this algorithm can help illuminate its effectiveness when working with this sort of data.

The algorithm works by doing successive linear interpolations to the arbitrary point (x, y, z) by enclosing it with a cube which has a point $C_{000} = (x_0, y_0, z_0)$ at the bottom left corner and a point $C_{111} = (x_1, y_1, z_1)$ at the top right corner. The corners of the cube are grid points which have known values of the quantity. 4 linear interpolations along the 4 cell corners from $x_0, y_{0,1}, z_{0,1}$ to x are done. Then, 2 interpolations from those x points are done along the y-axis to y and then one final interpolation along the z-axis is done to estimate the quantity at (x, y, z).

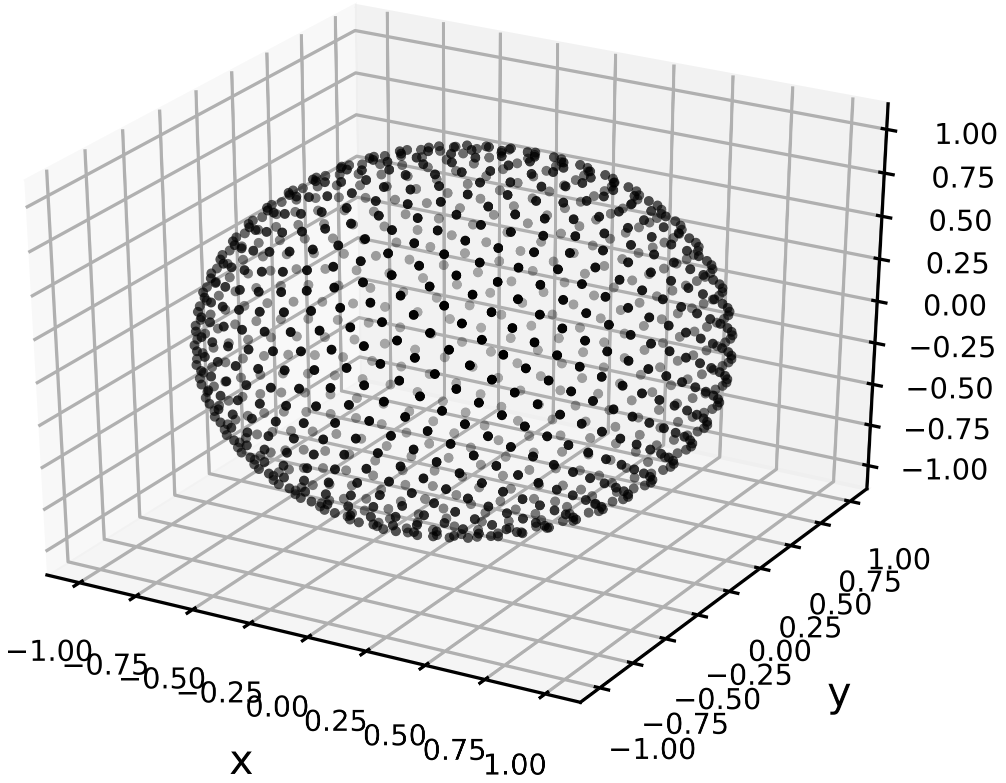

Figure 2.3: 1000 points uniformly distributed over a sphere using uniformly spaced r values to determine the θ points from equation 2.7 and ϕ points given by equation 2.9.

This method contains very useful properties that make it computationally fast. The trilinear interpolation is a local method that only requires information that is within the *neighbourhood* of that point to calculate it. Then, the fact that it is a regular grid makes it very easy to find the corresponding neighbours for the interpolation at (x, y, z) by using the binary search algorithm. These properties significantly speed up the calculations for computing an interpolation in the high resolution runs.

An example as to why this is needed is that in order to compute the spherical harmonics up to $\ell = 300$ at a single radius of 23.5 Mm in `N16`, it requires interpolations to $742,800$ points and these all require information from different points in order to compute the interpolation.

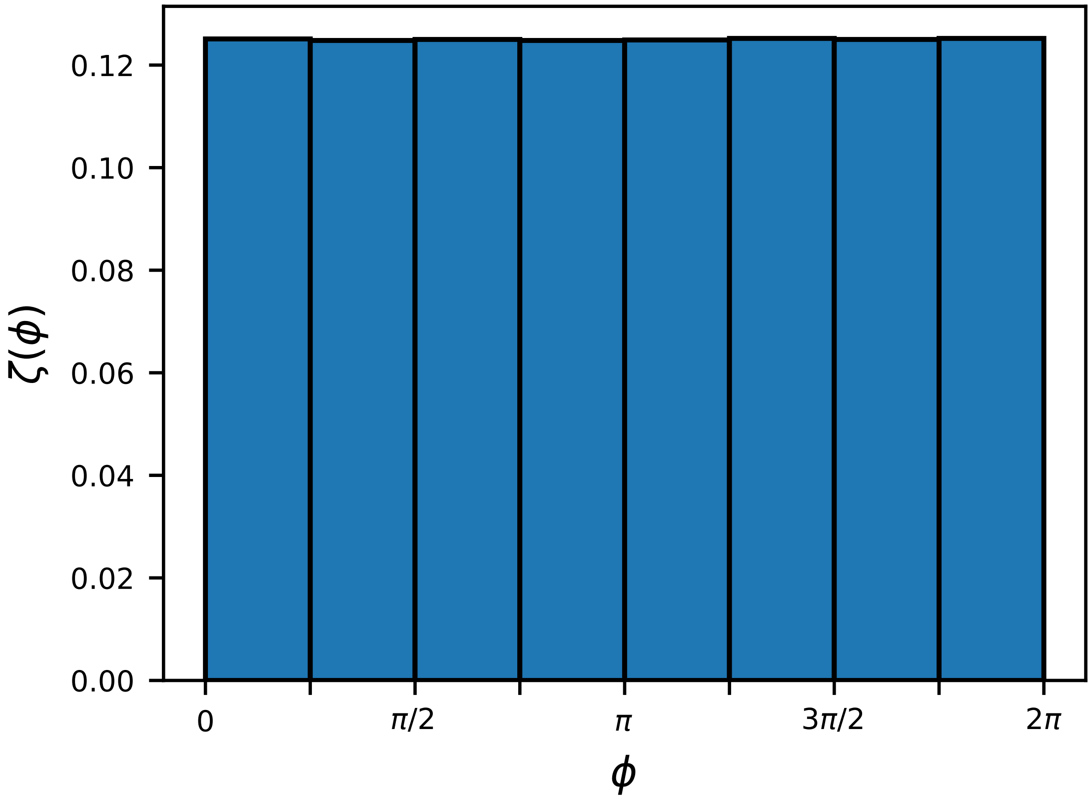

Figure 2.4: The pdf of 10,000 points sampled from equation 2.9. This results in a uniform distribution that is not due to a random number but is explicitly calculated depending on how many points there are.

With an interpolation method, the values of a quantity anywhere in the simulation can be determined. To interpolate onto a sphere with evenly distributed points representing equal areas cannot be done by simply splitting the θ and ϕ coordinates into equal pieces. This is because an area element on the unit sphere, $da = \sin\theta d\theta d\phi$, shows that the relative size of the $d\theta$ piece depends on $\sin\theta$. If constant $d\theta$ was used, the surface area of the points near $\theta = \pi/2$ would be significantly larger than the points near the poles. This can be restated as wanting to have N points within a region, $\theta \in (\theta, \theta + d\theta)$ and $\phi \in (\phi, \phi + d\phi)$ being proportional to the area of that region, $da = \sin\theta d\theta d\phi$. With the interpretation of the infintesimal area being a probability of a point being within that area, it can be interpreted as the joint probability density function (pdf) of the random variables θ and ϕ. The normalized joint pdf of θ and ϕ is

$$\kappa(\theta, \phi) = \frac{\sin\theta}{4\pi} \tag{2.1}$$

with the individual, normalized pdfs being

$$\psi(\theta) = \frac{\sin\theta}{2} \tag{2.2}$$

and

$$\zeta(\phi) = \frac{1}{2\pi} \tag{2.3}$$

To sample the points according to the pdf in equation 2.1 it is convenient to write it in terms of drawing samples from a uniform pdf, $u(r)$ ($r \in [0, 1)$), instead. To do this, the cumulative distributions of each pdf is needed. The cumulative distribution of $u(r)$ is designated by a capital letter, $U(r)$ and is

$$U(r) = \int_0^r dr = r \tag{2.4}$$

The transformation method allows for drawing a sample of the random variable x that follows the pdf $f(x)$ in terms of drawing a sample of the uniform random variable r. This is done by equating the two cumulative distributions, $F(x)$ and $U(r)$, and inverting $F(x)$ as

$$r = F(x) \tag{2.5}$$

$$x = F^{-1}(r) \tag{2.6}$$

Applying these to equations 2.2 and 2.3 yields

$$\theta = \cos^{-1}(1 - 2r) \tag{2.7}$$

and

$$\phi = 2\pi r \tag{2.8}$$

The distribution of θ is not uniform while, as expected, ϕ is uniform across its range.

This method could be sufficient for plotting purposes however there is another use case for interpolating points on a sphere which is to define radial rays of a quantity.

With a given θ and ϕ, a quantity could be plotted as a function of radius creating a ray. However, by using random numbers, each time the routine is run the distribution of points changes making it difficult to make use of this information. Instead of using a random number in equations 2.7 and 2.8 an explicit formula can be used for a given number of points. For a set of N points, the equation for θ can use uniformly spaced values of $1/N$ instead of the random number r while ϕ uses the formula

$$\phi_i = 2\pi \frac{(1+\sqrt{5})}{2} i \tag{2.9}$$

The $(1+\sqrt{5})/2$ term is the *golden ratio* which is used to make the points appear *visually* random along the entire sphere rather than simply increasing the indices linearly like θ (Fig. 2.3). In practice, a large number of these points from equation 2.9 have a distribution that is equivalent to a uniform pdf of ϕ across 0 to 2π as shown in Fig. 2.4.

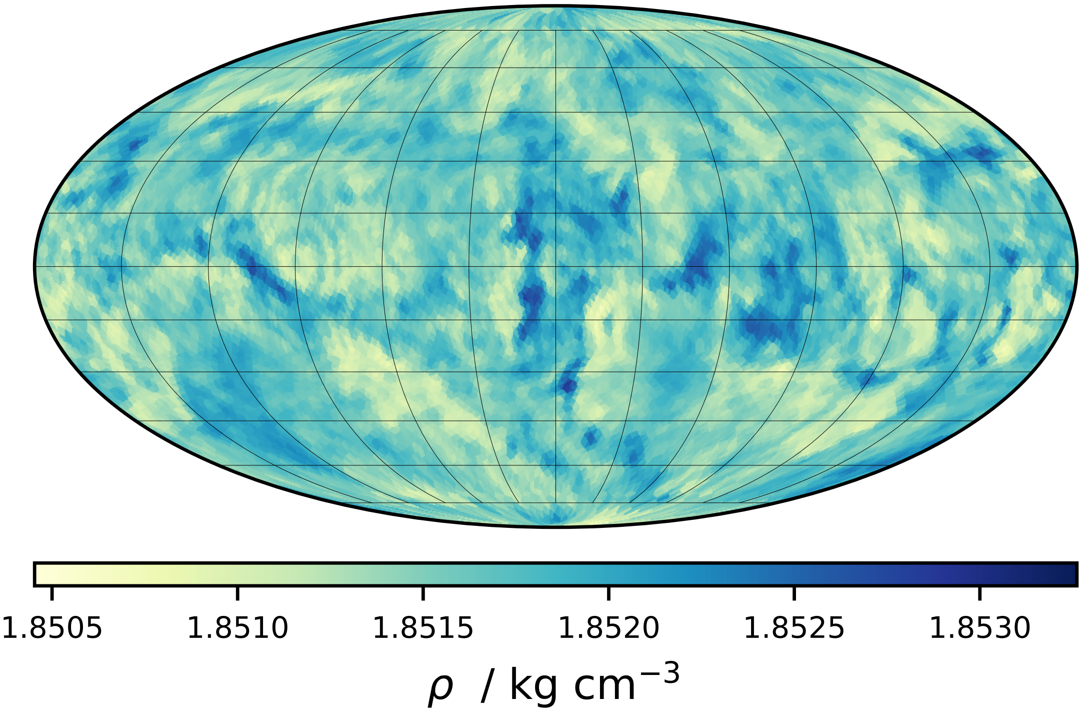

Figure 2.5: The mollweide projection of the density from `N16` at a radius of 9 Mm at t = 299 min using the linear interpolation technique described in Section 2.2.1. The numerical artifacts of the method are significantly damped compared with the binning technique shown in Fig. 2.2.

With a method to get uniformly distributed points on a sphere and being able to linearly interpolate to that sphere, the significantly improved mollweide plot of the density is shown in Fig. 2.5. There are still some numerical artifacts (ringing) occurring in this plot.

The moments data could also be used to determine the gradients of quantities at a given radius. The most important application of this would be the gradient of the X_{H} which would be used for a diffusion analysis. The diffusion coefficient can be written as

$$\vec{D}_{X_{\mathrm{H}}} = -\frac{\rho_{X_{\mathrm{H}}}\vec{v}}{\vec{\nabla} X_{\mathrm{H}}} \tag{2.10}$$

where $\vec{D}_{X_{\mathrm{H}}}$ is the diffusion coefficient, $\rho_{X_{\mathrm{H}}}\vec{v}$ is the mass flux of H and $\vec{\nabla} X_{\mathrm{H}}$ is the gradient of the mass fraction of H. Most stellar applications use only the radial component of the diffusion coefficient as it is expected that the material is distributed isotropically and thus only diffuses in the radial direction. Another application is looking at the anisotropy of the convective boundary which is defined by Jones et al. (2017) as the minimum gradient of the tangential velocity. This is discussed in detail in Section 3.4.1.2. Near the convective boundary, the radial gradient of the FV is shown in Fig. 2.6. The radial gradient was estimated using the central difference equation,

$$\frac{\partial f}{\partial x}(x_i) = \frac{f(x_{i+1}) - f(x_{i-1})}{2\delta x_i} + \mathcal{O}(\delta x_i^2) \tag{2.11}$$

for the x, y and z directions and then transformed to a radial derivative and interpolated onto the sphere. In the lower resolution run, `N15`, there are very strong numerical artifacts at the scale of the gradient in question. `N16` still shows these artifacts though to a smaller degree. From this data and the definition of the numerical derivative used, the errors in the derivative are proportional to the grid resolution squared. With the `N16` *briquette* data already being at the limits of what *python* can handle as well as the fact that 1536^3 `PPMstar` simulations are the scientific, high resolution runs, the *briquette* data cannot be used for estimating derivatives of quantities with the current techniques. It may be possible to use higher order interpolation to reduce the numerical effects and allow for estimating the derivatives of quantities.

2.2.2 Higher Order Interpolation

To get derivatives of quantities from the *briquette* data that are not dominated by numerical artifacts, higher order interpolation will be needed. There are two major

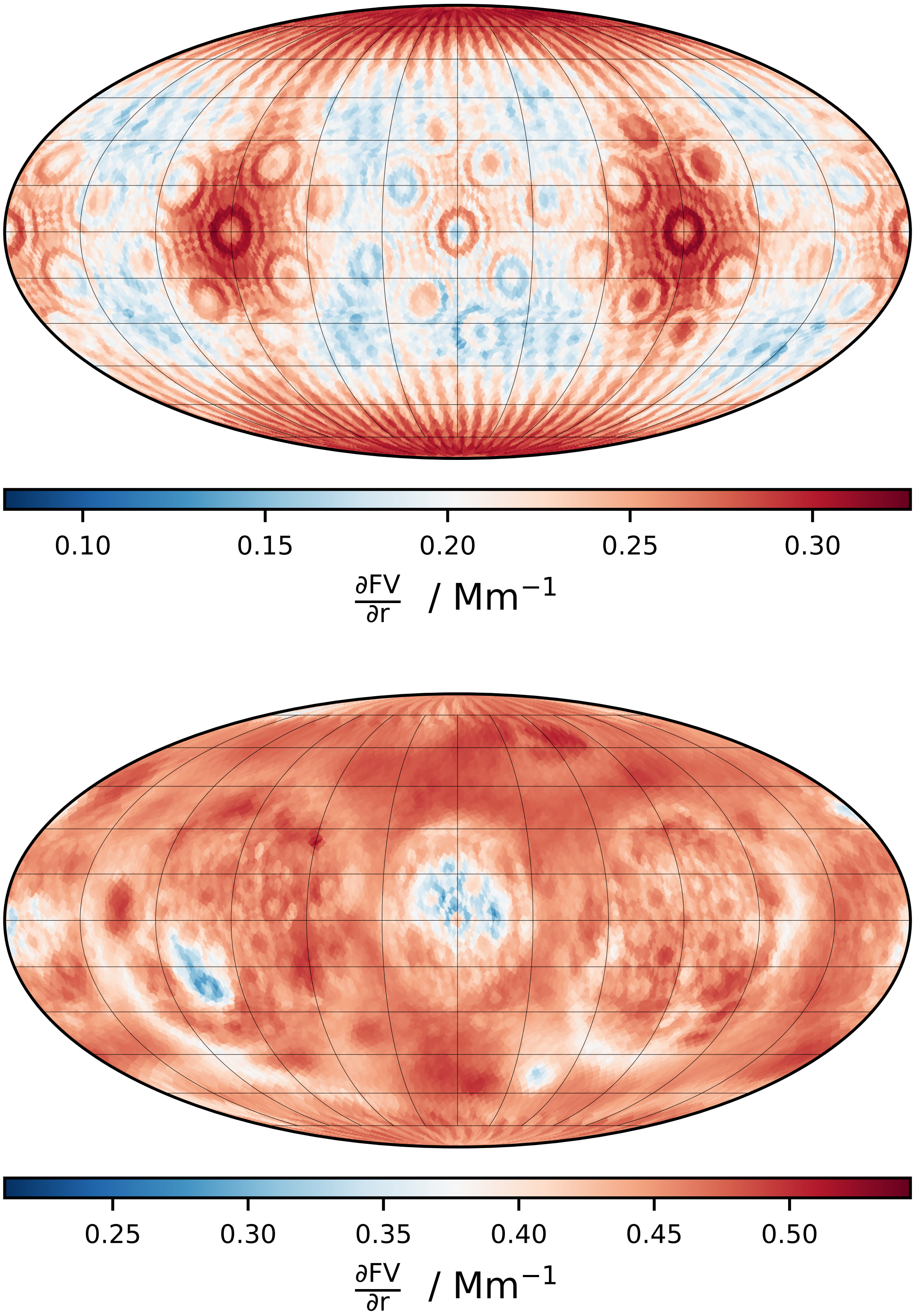

Figure 2.6: Both panels are the radial gradient of the FV at a radius of 23.5 Mm at $t = 299$ min. The top panel is `N15` with a briquette data cube of 192^3 while the bottom panel is `N16` with a briquette data cube of 384^3.

points that make it difficult to know how the radial derivative should be evaluated. Firstly, with higher order interpolants, they can be fit directly to the quantity of interest and then derivatives can be taken on the interpolation function to find the derivative of that quantity at any point. Or, numerical derivatives can be taken and then the interpolation can be done on those points to determine the derivative at any point. Secondly, because of the cubic grid, it is convenient and straightforward to take derivatives in the cartesian coordinates however it is unclear if a simple unit vector change will result with the correct gradient in spherical coordinates. Are the numerical representations of the gradient commutable with a change of bases? Is the radial gradient taken by interpolating to points on a sphere and taking the numerical derivative along the ray accurate? The order in which the operations of interpolation and derivatives, as well as how the derivatives are taken, will influence what the end result is so long as the resolution is finite. As the grid resolution decreases, these differences matter less and less.

To test the higher order interpolation methods, an analytic 1D function is used to study their behaviour. This function is given by

$$\eta(x) = a \tanh(cx) + b \tag{2.12}$$

where a, b and c are constants. This functions mimics the underlying functional form of the FV near the upper convective boundary. The derivative of this function is

$$\frac{\partial \eta}{\partial x} = ac \,\mathrm{sech}^2(cx) \tag{2.13}$$

To make these tests realistic to the sampling and resolution of the *briquette* data, a run, `M29`, which has a resolution of 768^3 was used. This is a model of H-core convection of a $25\mathrm{M}_{\odot}$ star that did not have any burning. What is relevant for the interpolation tests is that by using the underlying grid of `M29` it allows for a realistic sampling of equation 2.12 at the grid spacing. The FV data from `M29` is useful because it does not have any burning. This will help limit the higher order derivatives of the underlying function from being significantly large within the convection zone as the profile is essentially flat. All interpolation methods have errors that depend on the product of higher order derivatives of the underlying function being interpolated and the resolution. Fitting the FV of `M29` is a best case scenario for any interpolation method being applied to `PPMstar` simulations. All methods will be applied on a 1D ray along the x-axis with constant y and z coordinates.

2.2.2.1 Moments Interpolation

After linear interpolation, a quadratic function can be fit for interpolation. This is an interpolating technique that is used in the PPM method for advecting fluids, with which `PPMstar` is based off of. The interpolating function uses normalized unit coordinates such that the cell which is being interpolated has a range of $\tilde{x}, \tilde{y}, \tilde{z} \in [-1/2, 1/2]$. The interpolating function is

$$f(\tilde{x}, \tilde{y}, \tilde{z}) = a_{000} + a_{100}\tilde{x} + a_{010}\tilde{y} + a_{001}\tilde{z} + a_{110}\tilde{x}\tilde{y} + a_{101}\tilde{x}\tilde{z} + a_{011}\tilde{y}\tilde{z} + a_{200}\tilde{x}^2 + a_{020}\tilde{y}^2 + a_{002}\tilde{z}^2 \tag{2.14}$$

which only contains terms that are quadratic. With the fact that the *briquette* data are averaged quantities within their respective cells, it is useful to constrain the function by integrating it within the cell and requiring it to equal that cells value. The neighbouring cells *weight* the coefficients which describes how the quantity changes in each direction to quadratic order. There are 10 coefficients and so the function is weighted by the cells in a surrounding 3^3 cube resulting in a total of 27 cells. By integrating this interpolating function over the 27 cells, the coefficients can be determined. Integrating over the central cell yields,

$$\langle c_{000} \rangle = \int_{\tilde{x},\tilde{y},\tilde{z}=-1/2}^{1/2} f(\tilde{x}, \tilde{y}, \tilde{z}) d\tilde{x} d\tilde{y} d\tilde{z} = a_{000} + \frac{1}{12}(a_{200} + a_{020} + a_{002}) \tag{2.15}$$

$$a_{000} = \langle c_{000} \rangle - \frac{1}{12}(a_{200} + a_{020} + a_{002}) \tag{2.16}$$

and this can be applied to all 27 cells. Of course, this function is over constrained and so there is not a unique way to define the coefficients based on every cell average. Table 2.2 shows the coefficients that are used for this interpolating function in terms of the cell averages. This fitted function is only applicable within the central cell. A similar approach is used in the `PPMstar` code for the subgrid behaviour of the FV although there are additional constraints. This is called the *moments* method due to the idea that the interpolating function is describing up to the second moment of the quantity within that cell. Its application to the PPB advection of the FV is outlined in Appendix A of Woodward et al. (2015).

Applying this technique to the functional form of equation 2.12 with a sampling of that function according to `M29`'s grid is shown in Fig. 2.7. The quadratic interpolation

Table 2.2: The coefficients for equation 2.14 in terms of the cell averages of the 27 surrounding cells of the quantity being interpolated.

Moments Coefficient	In Terms of Cell Averages
a_{000}	$\frac{5}{4}\langle c\rangle_{000} - \frac{1}{24}(\langle c\rangle_{100} + \langle c\rangle_{-100} + \langle c\rangle_{010} + \langle c\rangle_{0-10} + \langle c\rangle_{001} + \langle c\rangle_{00-1})$
a_{100}	$\frac{1}{2}(\langle c\rangle_{100} - \langle c\rangle_{-100})$
a_{010}	$\frac{1}{2}(\langle c\rangle_{010} - \langle c\rangle_{0-10})$
a_{001}	$\frac{1}{2}(\langle c\rangle_{001} - \langle c\rangle_{00-1})$
a_{110}	$\frac{1}{4}(\langle c\rangle_{110} + \langle c\rangle_{-1-10} - \langle c\rangle_{-110} - \langle c\rangle_{1-10})$
a_{101}	$\frac{1}{4}(\langle c\rangle_{101} + \langle c\rangle_{-10-1} - \langle c\rangle_{-101} - \langle c\rangle_{10-1})$
a_{011}	$\frac{1}{4}(\langle c\rangle_{011} + \langle c\rangle_{0-1-1} - \langle c\rangle_{0-11} - \langle c\rangle_{01-1})$
a_{200}	$\frac{1}{2}(\langle c\rangle_{100} + \langle c\rangle_{-100}) - \langle c\rangle_{000}$
a_{020}	$\frac{1}{2}(\langle c\rangle_{010} + \langle c\rangle_{0-10}) - \langle c\rangle_{000}$
a_{002}	$\frac{1}{2}(\langle c\rangle_{001} + \langle c\rangle_{00-1}) - \langle c\rangle_{000}$

has a very poor representation of the underlying function within regions where the curvature is rapidly changing. This region is the most scientifically important region for trying to constrain the strength of CBM (Jones et al., 2017). The reason for its poor representation is because of the fact that there are no constraints to ensure that the function is continuous across different cells. The cell faces and grid center points of the fit are shown in Fig. 2.8. This method requires a significant amount of points in order for it to represent this transition region properly. Although it is not clear in Fig. 2.8, there are values of FV that are above 1 which is not possible. The linear interpolation does not have this issue because the lines are fit directly to the points and so the underlying interpolant is confined between the values of adjacent cells. For quantities that do not change rapidly from cell to cell in the radial direction, namely thermodynamic quantities, this method can be an alternative to the linear interpolation and formally has a higher accuracy.

2.2.2.2 Cubic Interpolation

Clearly from the *moments* interpolation with the resolutions that are used, constraints will be needed to ensure that some quantities, like FV, are bounded correctly. Two common cubic fitting routines are the cubic spline and the monotonic piecewise cubic Hermite interpolating polynomial (`PCHIP`). The *scipy.interpolate.CubicSpline* function is used for the cubic spline interpolation while the *scipy.interpolate.PchipInterpolator* is used for `PCHIP`. Applying these interpolating techniques to the sampled data of `M29` with the analytic function of equation 2.12 is shown in Fig. 2.7. Both of these

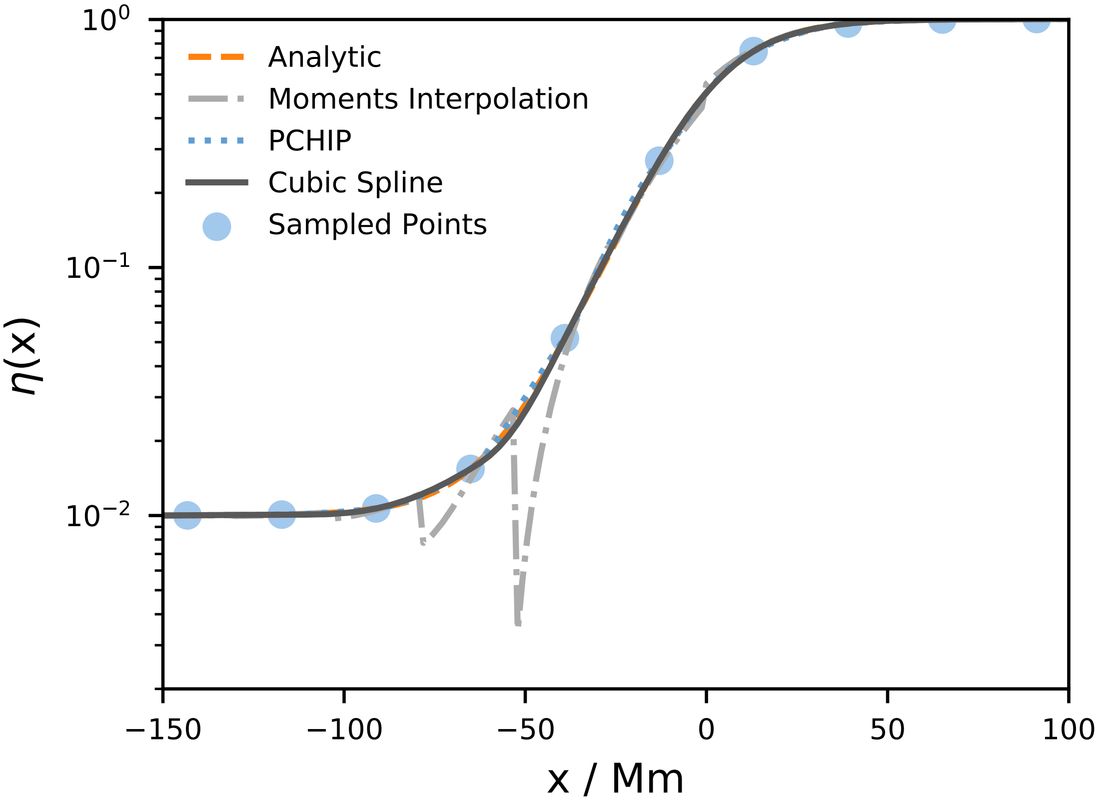

Figure 2.7: All 3 of the higher order interpolation methods discussed in Section 2.2.2 are applied to a function, equation 2.12, that is sampled on the grid of `M29` with a *briquette* resolution of 192^3. The analytic function is also plotted smoothly with the use of thousands of points. The interpolation methods are in 1D which causes most coefficients of the *moments* interpolation function, equation 2.14 and Table 2.2, to be zero.

techniques follow the analytic function very accurately and do not overshoot the FV above 1. Applying these to the actual FV data of `M29` is shown in Fig. 2.9.

Using a cubic spline interpolation on the 3D *briquette* data is not feasible. This is because the standard cubic spline technique uses global information as it simultaneously solves all coefficients for every cubic polynomial being fit between every point. This results in a sparse matrix that is inverted which is computationally expensive with many cells and 3 dimensions. It also has issues with not being monotonic between points causing significant over and under shoots (Fig. 2.9). On the other hand, the `PCHIP` algorithm is a local method that only requires information of its nearest neighbours making it suitable for *briquette* data. It also has a condition that forces

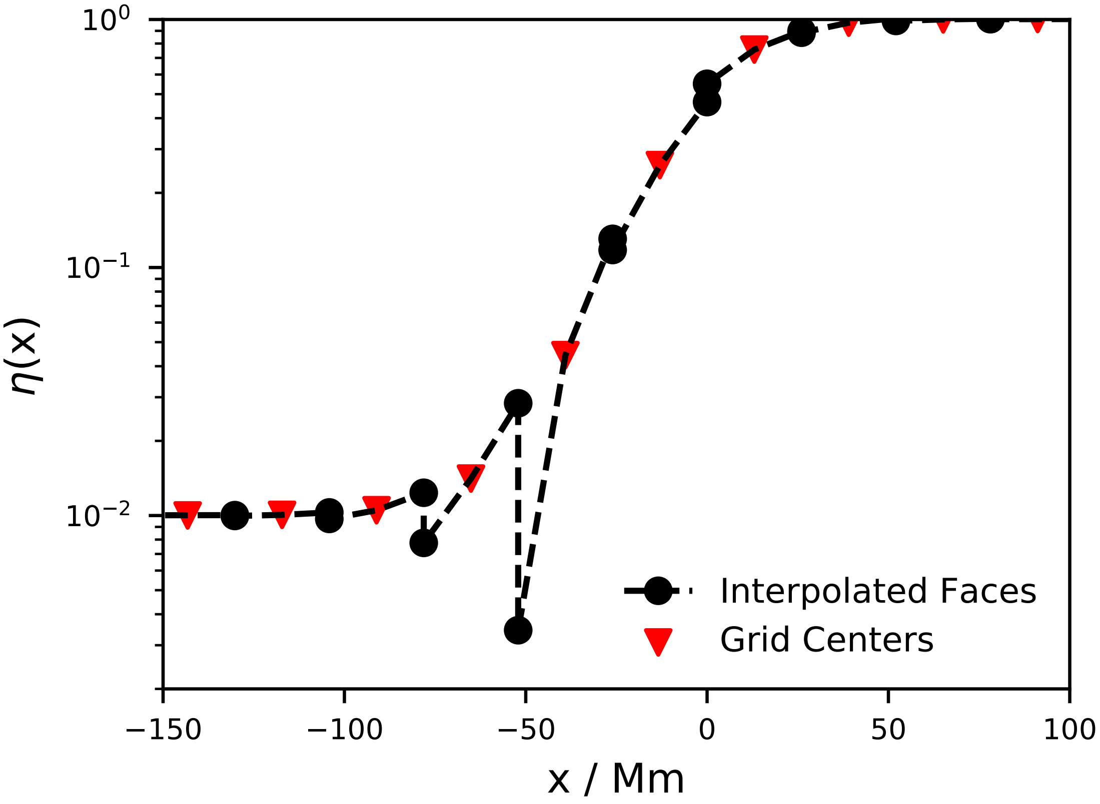

Figure 2.8: The *moments* interpolating function, equation 2.14, with the coefficients listed in Table 2.2 is applied to a function, equation 2.12, that is sampled on the grid of `M29` with a *briquette* resolution of 192^3. The sampled points which the interpolation method used are the grid centers, coloured in red, while the interpolation to the cell faces are coloured in black. The interpolation functions that describe a cells substructure are discontinuous across the cell faces when the underlying data is not *smooth* enough.

all cubic function fits between any two points to be monotonic. The interpolating function is strictly increasing, decreasing or flat between the two data points and thus no new maxima or minima are developed.

The formulation of the 1D `PCHIP` algorithm has its details in Fritsch & Carlson (1980) but a quick description of this algorithm is explained below. A cubic function in 1D has 4 coefficients requiring 4 constraints. The function is constrained to have the values specified at the two data points it is surrounded by as well as their derivatives. Since the derivatives are typically not known, the numerical derivative is estimated and evaluated at each point. To ensure the function is monotonic additional constraints are imposed on the derivatives. The algorithm ensures that the

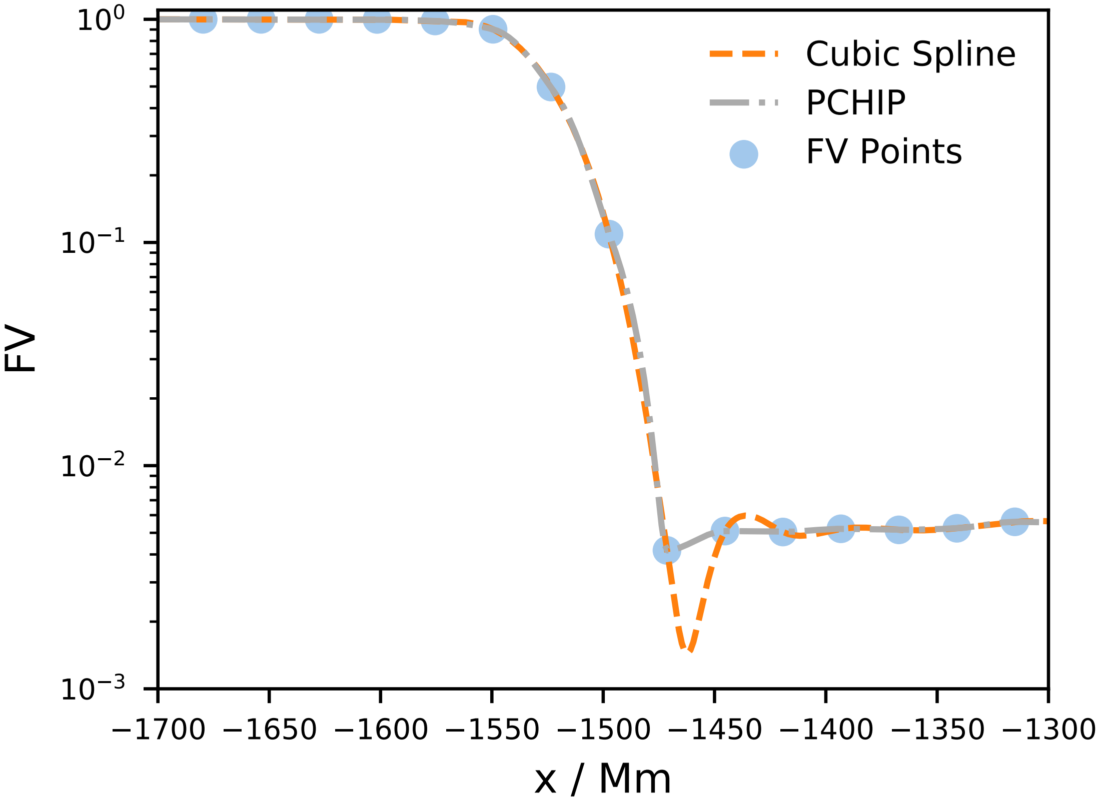

Figure 2.9: The *briquette* FV data from `M29` is fitted with a third order polynomial that has coefficients determined by two different methods, the cubic spline and `PCHIP` methods.

derivatives of the interpolant are continuous however the second derivative at the fitting points are discontinuous. This is seen in Fig. 2.10.

Since the `PCHIP` algorithm has a cubic interpolant, the derivative of that interpolant is quadratic. This can be compared with fitting the interpolant to two different estimates of the numerical derivative of the data, the central differences in equation 2.11 and

$$\frac{\partial f}{\partial x}(x_i) = \frac{-f(x_{i+2}) + 8f(x_{i+1}) - 8f(x_{i-1}) + f(x_{i-2})}{12\delta x_i} + \mathcal{O}(\delta x_i^4) \tag{2.17}$$

the 5-point stencil. These numerical derivatives are computed on the sampled data of equation 2.12 in Fig. 2.10 and for the FV data of `M29` in Fig. 2.11. For fitting data directly to the numerical derivative estimates in Fig. 2.10, it is clear that the `PCHIP` constraints force the cubic fits to underestimate the maximum of the derivative

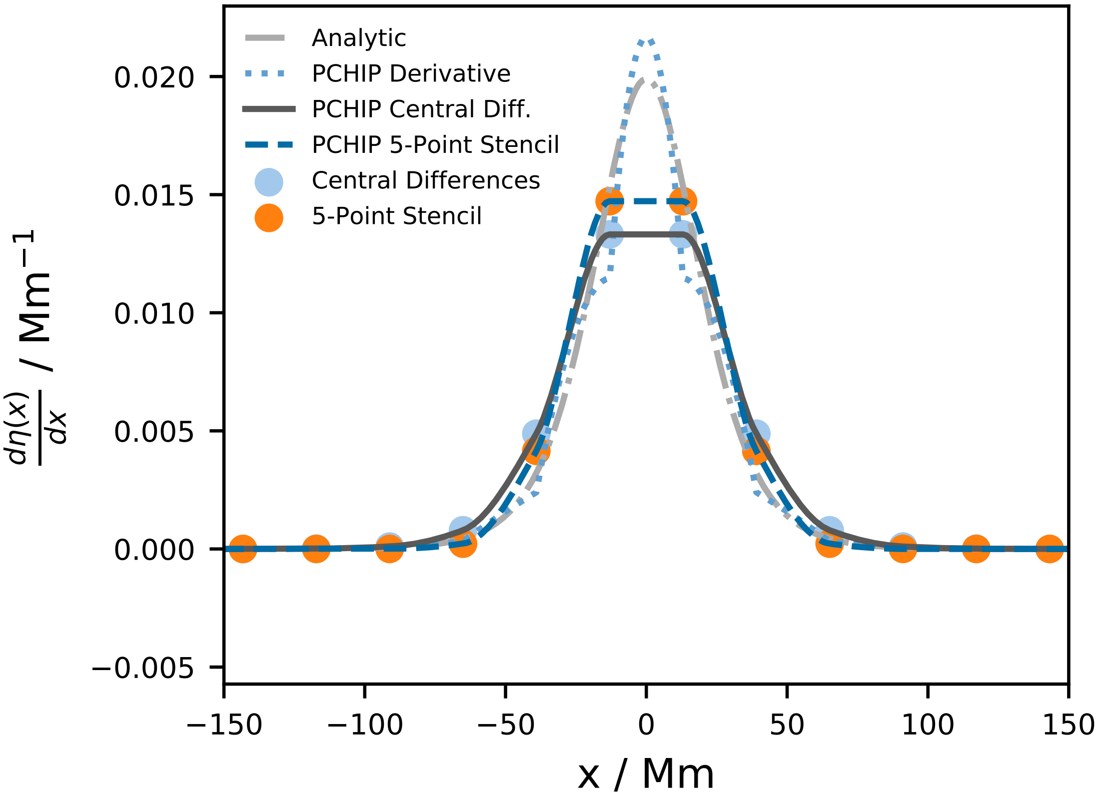

Figure 2.10: The `PCHIP` interpolation is applied to various types of sampled points to see which method best reproduces the analytic derivative (equation 2.13). The `PCHIP Derivative` line took the derivative of the interpolating function which used sampled points of the original analytic function (equation 2.12). The `PCHIP Central Diff.` and `PCHIP 5-Point Stencil` fit the interpolating function on two different estimates of the numerical derivative of the sampled points of the original analytic function. These are the central differences, equation 2.11, and 5-point stencil, equation 2.17, respectively.

due to the algorithm enforcing no new maxima between points. This causes the interpolation function to always have a maximum (or minimum) value that is exactly at a data point. By the arbitrary sampling of the function in equation 2.13, the maxima happens to be between two data points causing this underestimating issue. In Fig. 2.11 a different scenario occurs due to the sampling, the maxima is pinned down to one point with it falling off on either side. Based on whether the numerical derivative is taken with equation 2.11 or 2.17, the maximum value of the derivative changes but the location of the maxima does not.

Taking the derivative of the `PCHIP` interpolation functions yield quadratic func-

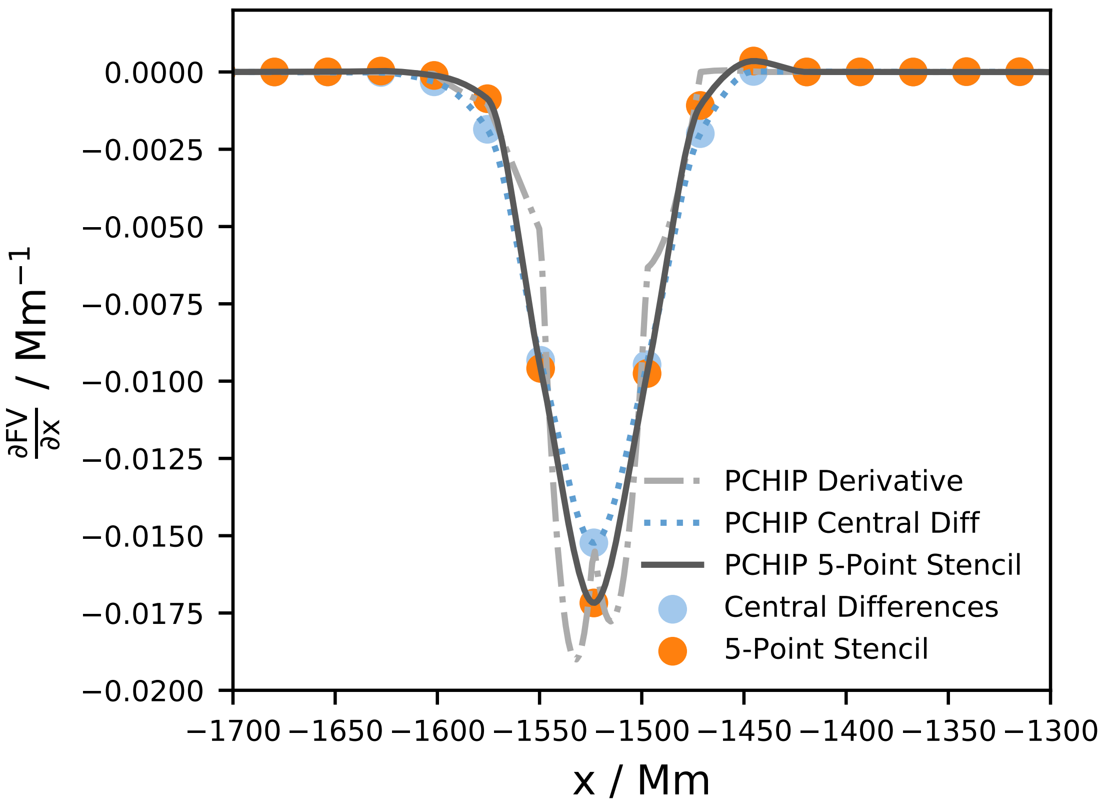

Figure 2.11: The `PCHIP` interpolation is applied to the `M29` *briquette* FV data. The real derivative of the FV is not known. The `PCHIP Derivative` line took the derivative of the interpolating function which used the FV data. The `PCHIP Central Diff.` and `PCHIP 5 Point Stencil` fit the interpolating function on two different estimates of the numerical derivative of the FV data.

tions. These quadratic functions are able to better estimate what the analytic derivative of equation 2.12 is in Fig. 2.10 with a maxima between the two sampled points however it is only smooth between the points and inherits a discontinuity in the derivative at the interpolant points. In Fig. 2.11 this technique causes the quadratic fit to have two local maxima on either side of one of the interpolant points. Due to the sparsity of the *briquette* grid points within the transition region, the derivative of the FV within this region is highly uncertain even with multiple techniques utilizing cubic interpolants.

This analysis was done with *briquette* data with a 192^3 grid and so doubling the resolution will improve the estimates. However, it would be more accurate to instead directly estimate the derivative of the FV in all cartesian directions and output it as a *briquette* averaged quantity rather than taking numerical derivatives on the *briquette* averaged quantities, though this is currently not implemented in the `PPMstar` simulations. There is also the difficulty of extending the `PCHIP` algorithm to 3D. The number of coefficients for a general cubic function in 3D is 64. Using 27 cell points and the derivatives on those cells only leads to 54 constraints, 10 more would be needed. It is also unclear how the monotonicity condition would be extended to such a cubic function which is clearly needed for quantities such as FV. It could be possible to use multiple `PCHIP` interpolations just like the trilinear interpolation stated in Section 2.2.1 to interpolate. However, due to the simplicity and reasonable accuracy of the trilinear method, the calculations using *briquette* data in Chapter 3 use the trilinear interpolation.

3

3D1D hydro-nucleosynthesis simulations. I. Advective-reactive post-processing method and application to H-ingestion into He-shell flash convection in rapidly accreting white dwarfs

Attribution

The following text represents a paper that is in preparation for submission at the time of the submitting this thesis. Apart from the editorial comments that were pointed out by the co-authors, all of the text is written solely by me except for the sections titled:

- PPMstar simulations (Section 3.3.1, written by Falk Herwig and myself)
- Diffusion post-processing (Section 3.3.2, written by Robert Andrassy)

The plots and analysis of this work, excluding the sections above, were completed solely by me. I ran the hydrodynamic simulations that were analyzed in this work. The original setup of the stratification for the hydrodynamic simulations was created by Robert Andrassy for a previous project, Denissenkov et al. (2019). The authors of this paper are (in this order)

- David Stephens, Department of Physics and Astronomy University of Victoria
- Falk Herwig, Department of Physics and Astronomy University of Victoria
- Paul Woodward, LCSE and Department of Astronomy University of Minnesota
- Robert Andrassy, Heidelberg Institute For Theoretical Studies

- Pavel Denissenkov, Department of Physics and Astronomy University of Victoria
- Huaqing Mao, LCSE and Department of Astronomy University of Minnesota

3.1 Abstract

We present two methodologies for post-processing 3D hydrodynamic simulations for applications in convective-reactive *i*-process nucleosynthesis. The application of said models are on a rapidly accreting white dwarf (RAWD) with [Fe/H] $= -2.6$ in which H is ingested into a convective He-shell during a He-flash. A 1D advective two stream model is formulated with the radial and horizontal mixing coefficients of that model being constrained by 3D hydrodynamic simulations. A more traditional modeling approach uses diffusion coefficients calculated from those same simulations. All 3D simulations include the energy feedback of the $^{12}\mathrm{C}(p,\gamma)^{13}\mathrm{N}$ reaction from the entrainment of stably stratified H. Global Oscillations of Shell H-ingestion (GOSH) in two of the RAWD simulations cause bursts of entrainment of H that is subsequently burned and feeds energy back into the flow. In each of the RAWD simulations, the entrainment and burning of H in is quasi-static up to simulation times of 300 min. The 1D advective two stream model predicts the rate, location and total mass of H burned in the He-shell that closely match what the 3D simulations predict. This is true even in the simulation whose GOSH causes major spherical asymmetries in the convective flows and entrainment of H at rates up to 40 times higher than during its quasi-static phase. The asymmetry between the X_{H} profiles of the up- and down-streams is in qualitative agreement with the 3D simulations.

3.2 Introduction

The details of mixing in convection zones within the stellar interior modifies the evolution of stars from the main sequence to core collapse. The continual mixing of H in the convective cores of intermediate to massive stars sets a timescale for the eventual main sequence turn off. This can be extended from convective boundary mixing (CBM) which slowly introduces additional H fuel to the core. Over the lengthy nuclear timescale of the H-burning during the main sequence, the mixing of chemical species is computed using either an instantaneous or diffusive mixing routine. The nuclear burning timescale is significantly longer than the mixing timescale within the convective core leading to the details of the mixing within the convective zone being sufficiently modeled with a space-time average theory. Such a theory, the mixing length theory (MLT Cox & Giuli, 1968), describes the energy transport and mixing properties of a convective region using averaged quantities over space and time. In advanced stages of evolution for massive stars the nuclear burning timescales approach convective timescales and so the details of the mixing become increasingly important for their structure as highlighted in Davis et al. (2019). To quantify this phenomenon, it is useful to define the Damköhler number, $D_{\mathrm{a}} = \tau_{\mathrm{mix}}/\tau_{\mathrm{nuclear}}$, which is the ratio of the mixing and nuclear burning timescales. As this number becomes larger and closer to 1, the details of the mixing have a greater impact on the burning.

For the cases where the Damköhler number is 1, 3D hydrodynamic simulations could advect many species and determine the convective-reactive nucleosynthesis inline. However, modeling any complicated nucleosynthesis, for example the *i*-process, can require networks with 1000's of species that can interact with each other which is well beyond the capabilities of any 3D hydrodynamic code on modern computing clusters today. 1D mixing models will be required to determine any complicated nucleosynthesis for the near future. However, it is useful to use 3D hydrodynamic simulations to determine the mixing properties of the convection zone and how the hydrodynamic instabilities lead to the entrainment of stably stratified material. The 3D hydrodynamic simulations of Ritter et al. (2018a) modeled a convective O-shell with a stable C-shell from a $15\mathrm{M}_{\odot}$ stellar model of Ritter et al. (2018b) to obtain estimates for the expected entrainment rate of the C-rich material. Using diffusive mixing constrained by the mixing properties of the convection zone and appropriate entrainment rates, the 1D nucleosynthetic post-processing models produced significant amounts of odd-Z elements like P, Cl, K and Sc which could explain the underproduction of said elements in current GCE models (Ritter et al., 2018a). The inline network only included the energy generation from the $^{12}\mathrm{C}(^{12}\mathrm{C}, \alpha)^{20}\mathrm{Ne}$ and subsequent $^{16}\mathrm{O}(\alpha, \gamma)^{20}\mathrm{Ne}$ reaction.

An interesting case arises when H is ingested into a He burning shell which then causes the $^{12}\mathrm{C}(p, \gamma)^{13}\mathrm{N}$ reaction. After the $^{13}\mathrm{N}$ beta decays to $^{13}\mathrm{C}$ the $^{13}\mathrm{C}(\alpha, n)^{16}\mathrm{O}$ reaction can release neutrons if the temperatures within the He shell are high enough. Sakurai's object has a unique abundance pattern (Asplund et al., 1999) which can be explained with H being ingested into the He-shell flash convection zone of this post-AGB star (Herwig et al., 2011). This causes the chain of reactions stated earlier and produces neutron densities high enough to be in the *i*-process regime ($N_n \approx 10^{12} - 10^{16}\,\mathrm{cm}^{-3}$) (Cowan & Rose, 1977). The energy generation from this ingestion of H is significant enough to cause a split in the He-shell flash convection zone in 1D stellar evolution models. To study the nucleosynthesis of Sakurai's object, Herwig et al. (2011) used a spherically symmetric diffusive mixing model even though it explicitly violates many of MLT's criteria for applicability. This is shown explicitly in the 3D hydrodynamic simulations of this very energetic event which bring about a GOSH, Global Oscillation of Shell H-ingestion, that causes large scale, energetic flows that making the star deviate significantly from spherical symmetry (Herwig et al., 2014).

A more quasi-static convective-reactive case of H-ingestion into a He-shell is within a Rapidly Accreting White Dwarf (RAWD) (Denissenkov et al., 2017). The 3D hydrodynamic simulations of Denissenkov et al. (2019) quantified the entrainment rates however the diffusive mixing used in the post-processing was taken directly from the stellar evolution models. The neutron densities reach $N_n \approx 10^{13}\,\mathrm{cm}^{-3}$ resulting in i-process nucleosynthesis. With the common-envelope accretion scenario being common in the universe, the RAWD heavy metal production could be significant enough to result in a significant portion of the Kr, Rb, Sr, Y, Zr, Nb and Mo composition in the Sun (Côté et al., 2018). The convective-reactive flows fed by the $^{12}\mathrm{C}(p,\gamma)^{13}\mathrm{N}$ energy generation is only $2-3\%$ of the total luminosity within the He-shell and does not lead to a GOSH in the previous work of Denissenkov et al. (2019).

A solution to the concerns of the validity of diffusive mixing in a convective-reactive environment and the inability of 3D hydrodynamic simulations to perform complex nucleosynthesis inline is to use a 1D advective mixing model. One such model has been formulated for use in the post-processing nucleosynthesis of stellar evolution models from the Monash group, MONSOON (Henkel et al., 2017). The model contains two adjacent streams of fluid flow (see Fig. 3.1 and Fig. 1 in Henkel et al., 2017), one with fluid moving upwards and another with fluid moving downwards. The two streams have an enforced horizontal mixing in order to conserve mass but it can also add in additional horizontal mixing. The radial transport velocities as well as the additional horizontal mixing within a convection zone are estimated with MLT.

The most severe limitations of the MONSOON methodology arise in the treatment of the additional horizontal mixing. The strength of this mixing has no dependence on the structure of the flow within the convection zone. Is the mixing between the two streams that represent the dipolar flows of core convection the same as if the flow field was at smaller angular scales like in shell convection (Chandrasekhar, 1961)? There is also a weak dependence on the horizontal mixing based on where a cell is within the convection zone. Shouldn't the mixing between the two streams, in low $\mathcal{M}a$ number flows, be stronger near the convective boundaries where the fluid is forced to overturn well before the boundaries (Jones et al., 2017)? These limitations are addressed in the 1D advective stream model of this work.

In this paper, we create 3D hydrodynamic simulations of a RAWD from Denissenkov et al. (2019) to quantify the mixing of H into the He-shell. After extracting the mixing information from the 3D hydrodynamic simulations for both the 1D diffusive mixing (Jones et al., 2017) and 1D advective stream models, the time evolution of the H burning in each is calculated. The details of the 3D hydrodynamic simulations, and the diffusive and advective mixing approaches are outlined in Section 3.3. Section 3.4 discusses the flow properties of the simulations and shows the post-processing of the 3D hydrodynamic simulations with the diffusive and advective mixing routines. Section 3.5 describes the implications of such results and further applications.

3.3 Methods

3.3.1 PPMstar Simulations

The advective post-processing method introduced here is applied to 3D hdyrodynamic simulations of He-shell flash convection in a rapidly accreting white dwarf (Denissenkov et al., 2017). The initial stratification has been taken from stellar evolution model G with metallicity [Fe/H] $= -2.6$ from Denissenkov et al. (2019).

As in previous work (Herwig et al., 2014; Jones et al., 2017) we use the `PPMstar` code of Woodward et al. (2015) with additional details provided by Andrassy et al. (2018). The explicit Cartesian-grid-based code is based on the Piecewise-Parabolic Method (PPM; Colella & Woodward, 1984; Woodward, 1986, 2007; Woodward & Colella, 1981, 1984), and tracks the advection of concentrations in a two-fluid scheme using the Piecewise-Parabolic Boltzmann method (PPB; Woodward, 1986; Woodward et al., 2015).

The luminosity from the ^{4}He burning within the convection zone is modeled with a constant volume heating. The entrained H reacts with the abundant ^{12}C, from the triple alpha ashes, in the $^{12}\mathrm{C}(p,\gamma)^{13}\mathrm{N}$ reaction. This reaction rate is computed using the analytic form of the rate from Angulo et al. (1999). We ignore the subsequent beta decay of ^{13}N leaving a total energy release per reaction of $Q = 1.943$ MeV. The two reactant fluids, the stably stratified fluid, $\mathcal{F}_1$, containing 89.4% by number of H and the convectively unstable fluid, $\mathcal{F}_2$, containing 14.3% by number of ^{12}C.

Table 3.1: Summary of the `PPMstar` simulations that were computed for this work. The entrainment rates are the slopes of the linear fits shown in Fig. 3.10 while the different definitions of the convective boundary are discussed in Section 3.4.1.2. All calculations are computed at $t = 299$ min.

run ID	Grid	t^{i}_{sim} (min)	t^{ii}_{adv} (min)	L_{He} ($L_{\odot}$)	$r^{iii}_{\mathrm{b,SC}}$ (Mm)	$r^{iv}_{\mathrm{b},v_{\perp}}$ (Mm)	$\dot{M}_{\mathrm{e}}$ ($\dot{M}_{\odot}\,\mathrm{s}^{-1}$)
N15	768^3	1634	47	1.46×10^8	23.86	23.59	1.07×10^{-11}
N16	1536^3	744	47	1.46×10^8	23.84	23.69	7.21×10^{-12}
N17	1152^3	631	47	14.6×10^8	26.74	26.82	1.08×10^{-10}

Notes: ^{i} The total star time of the simulation; ^{ii} The start of the advective post-processing of the simulation; ^{iii} The initial Schwarzschild boundary of the 3D simulations followed in the Lagrangian coordinates; ^{iv} $\partial v_{\perp}/\partial r$ where $v_{\perp}$ is the rms of the tangential velocity

3.3.2 Diffusive Post-Processing Model

Jones et al. (2017) invert the diffusion equation to derive a radius-dependent diffusion coefficient, which produces in 1D the same redistribution of species over the time frame of analysis as that given by their spherically-averaged 3D simulations of O-shell convection. They measure the rate of change in the radius-dependent mass fraction $X(r,\ t)$ of a species by computing the difference between the mass fraction profiles at two different points in time with some time averaging applied around them. With $\partial X/\partial r$ also known from the spherical averages, Jones et al. (2017) solve for the unknown diffusion coefficient $D(r)$ in the 1D Eulerian diffusion equation

$$\frac{\partial X}{\partial t} = \frac{\partial}{\partial x}\left(D(r)\frac{\partial X(r)}{\partial x}\right), \tag{3.1}$$

where they set $x = r$. We have improved upon this method[1] by mapping the results of the input 3D Eulerian simulations to a mass coordinate $m(r)$ and inverting the Lagrangian diffusion equation

$$\frac{\partial X}{\partial t} = \frac{\partial}{\partial m}\left(\sigma(m)\frac{\partial X(m)}{\partial m}\right) + \frac{\dot{q}}{\rho}, \tag{3.2}$$

where $\sigma = (4\pi r^2 \rho)^2 D(r)$ is the Lagrangian diffusion coefficient, ρ the density and $\dot{q}(m,\ t)$ destruction/creation rate of the species by nuclear reactions. This new approach has the following advantages:

- It removes the effect of thermal expansion and contraction from $\partial X/\partial t$. This effect has negligible influence on the results of Jones et al. (2017), but it is essential to account for in the rapidly expanding atmospheres of the RAWD simulations reported in the present work.
- It properly takes into account the spherical geometry of the problem and the radial dependence of the density.
- It takes into account nuclear reactions, which are present in our RAWD simulations but not in those of Jones et al. (2017).

---

[1] Andrassy et al. (2019), in preparation.

3.3.3 Advective Post-Processing Model

The 1D advection is formulated using a two stream approach in which one stream transports species radially upwards, while the other stream transports them radially downwards (Cannon, 1993; Henkel et al., 2017, Fig. 3.1). By default, the two streams are taken to be equal in their surface areas which is justified by the analysis of the 3D flow properties (see Section 3.4.1.1) and the discussion in Section 3.3.3.2. The model can have horizontal mixing between up- and down-stream cells that are adjacent to each other.

There are N cells per stream. The index i refers to the spatial index of the $2N$ cells and is used where the equations are agnostic to whether the cell is within an up- or down-stream. For computational and numerical simplicity, the indexing is done such that the downstream is inverted and *stitched* onto the top of the upstream. The indexing starts at the bottom of the upstream at $i = 1$ and so cell $i = N + 1$ is at the top of the downstream. The index k refers to species.

The discretization distinguishes variables defined on the cell boundaries which have spatial half-integer indices, $i + 1/2$, while those that represent cell averages have spatial integer indices i.

3.3.3.1 Discretized Equations

To formulate the equations we start off with the conservation of mass equation and then apply the divergence theorem to it to yield

$$\partial_t \int_V \rho \mathrm{d}V = - \oint_{\partial V} \rho \vec{v} \cdot \mathrm{d}\vec{a} \tag{3.3}$$

The term on the right hand side is interpreted as a sum of mass fluxes through the boundary of the given volume, V. The term on left hand side is the rate of change of the mass contained within that volume. This advective model conserves the total mass of every cell which requires that the mass fluxes at every cell sum to zero. This condition comes from the description and discussions of the various mass fluxes on a given cell in Sections 3.3.3.2 and 3.3.3.3 and those fluxes are shown in Fig. 3.1. Recasting equation 3.3 into the partial densities of every species, integrating both

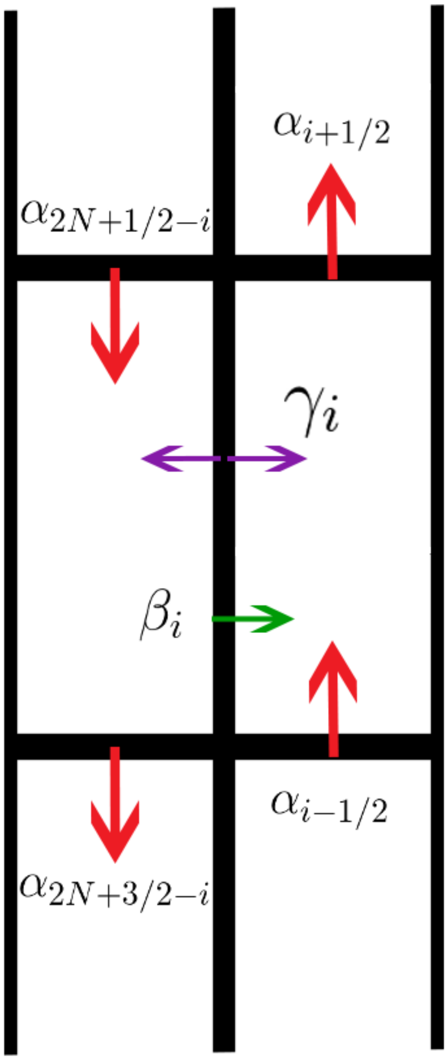

Figure 3.1: An illustration of the two stream model including all of the fluxes for a cell within the convection zone; α the radial mass flux (Section 3.3.3.2), β the enforced horizontal mass flux and γ the additional horizontal mass flux (Section 3.3.3.3). The index i refers to the upstream cell which has an adjacent downstream cell $2N+1-i$. The top downstream cell, $i = N+1$ has additional mass fluxes due to entrainment which is described in Section 3.3.3.4.

sides and applying the constraint that the mass of every cell is constant leads to

$$\partial_t \left(\sum_k m_{k,i} \right) = -(\sum_k \sum_{j=1}^{7} F^j_{k,i}) = 0 \tag{3.4}$$

where the index j refers to a specific species mass flux on the surface of cell i. The mass, $m_{k,i}$, of a given species within a cell can change however the total mass within that cell cannot. This is implicitly satisfied with equation 3.4. Therefore these equations only transport the mass of a given species throughout the convection zone and not the total mass of a cell i. Equation 3.4 includes all fluxes in the advective model and it is integrated explicitly. Two of the fluxes are from the entrainment of fluid into the convection zone which are zero for every cell except for cell $N+1$ which is at the top of the downstream (see Section 3.3.3.4). These fluxes are not shown in Fig. 3.1 for clarity.

3.3.3.2 Radial Mixing and Boundary Conditions

Within the convection zone, the bulk transport of species is through the radial direction. The radial mass flux, α, on each cell's upper and lower boundaries are given by

$$\alpha_{i+1/2} = 2\pi r_i^2 \rho_{i+1/2} v_{i+1/2} \tag{3.5}$$

where r, ρ, v are the radius, density and velocity defined on a cells boundary. The velocity is a positive-definite quantity in this model; the mass fluxes of individual species will explicitly carry the appropriate sign for transport. The radial species mass fluxes for cell i are

$$F^O_{k,i} = \alpha_{i+1/2} X_{k,i+1/2} \tag{3.6a}$$

$$F^I_{k,i} = -\alpha_{i-1/2} X_{k,i-1/2} \tag{3.6b}$$

where the superscript O and I refer to the outflow and inflow of mass at cell i, respectively. These constitute two of the fluxes from equation 3.4. The radius, density and velocities are all defined on the boundaries however the mass fraction of a particular species, k, is an average within a cell i. To achieve second order accuracy in the solutions of these equations, the mass fraction on the boundary is determined through a linear interpolation. There are two estimates for the interpolated state,

$$X_{k,i+1/2} = X_{k,i+1} - \frac{1}{2}\frac{\partial X_{k,i+1}}{\partial m_{i+1}} \delta m_{i+1} \tag{3.7a}$$

$$X_{k,i+1/2} = X_{k,i} + \frac{1}{2}\frac{\partial X_{k,i}}{\partial m_i} \delta m_i \tag{3.7b}$$

referring to the *up-sided* and *down-sided* estimates of the interpolated mass fraction, respectively. To ensure that the numerical scheme is stable, the interpolated state is chosen such that the discretization is *upwinding*. In practice, this just means that if the velocity is upwards, the *upwinded* interpolated state is the *down-sided* estimate because material is being advected upwards. To reduce the high frequency oscillations in the solutions when there are discontinuities and minima/maxima in the slope estimates, the minmod limiter is used on those numerically estimated slopes (LeVeque, 2002).

$$\frac{\partial X_{k,i}}{\partial m_i} = \texttt{minmod}(\frac{X_{k,i} - X_{k,i-1}}{\delta m_i}, \frac{X_{k,i+1} - X_{k,i}}{\delta m_i}) \tag{3.8}$$

where

$$\texttt{minmod}(a, b) = \begin{cases} a & \text{if } |a| < |b| \text{ and } a \cdot b > 0 \\ b & \text{if } |b| < |a| \text{ and } a \cdot b > 0 \\ 0 & \text{otherwise} \end{cases} \tag{3.9}$$

In order for this model to remain consistent with the nearly-hydrostatic equilibrium of the underlying 3D stellar hydrodynamic simulation, every spherical shell must have a net mass flux of zero to ensure that there is no net mass transport in the radial direction. This means that

$$\alpha_{i+1/2} = \alpha_{2N+1/2-i} \tag{3.10}$$

At the inner and outer boundaries of the convection zone the velocities are zero. Physically, this condition is enforcing that all of the radial flow is turning over at the boundary such that there is only a horizontal flow. Of course, fluid can and does over turn at some distance before the boundary (Jones et al., 2017) which are written as sources of horizontal mixing in this model (Section 3.3.3.3). The constraints on the radial mass flux coefficients to enforce a horizontal flow at the boundaries are

$$\alpha_{N-1/2} = \alpha_{N+1/2} = \alpha_{N+3/2} \tag{3.11a}$$

$$\alpha_{2N-1/2} = \left(\alpha_{2N+1/2} \equiv \alpha_{1/2}\right) = \alpha_{3/2} \tag{3.11b}$$

These coefficients cause, at the uppermost cell in the upstream, all of the mass that enters that cell to flow directly into the uppermost cell in the downstream. This is a horizontal flow. These boundary conditions are essentially periodic boundary conditions and from the numerical and computational perspective, it is convenient to have the two streams attached to each other to form a ring. By applying equation 3.3 to a convection zone that has zero velocity on its boundaries, there is no mass entering or leaving the convection zone and so it remains constant. For this reason, the model follows the Lagrangian coordinates of the initial convection zone as it expands in Eulerian coordinates (Section 3.4.1.2).

In equation (3.5), the radial mass flux depends on a surface area, taken to be $2\pi r^2$, to which the underlying transport of mass, ρv, is advected through. In principle, the surface area can be different between the up- and down-stream cells and still ensure that the net mass flux is zero so long as the product ρv with the respective surface areas are constant at every shell. With the low $\mathcal{M}a$ number flows in the RAWD simulations, the largest density perturbations are at the percent level as seen in Fig. 3.3. The density can therefore be approximated to be constant at every shell so that $\rho_{i+1/2} = \rho_{2N+1/2-i}$. The spherical average of the radial velocity at every shell is zero (Fig. 60). This also means that the spherical average of the positive and negative components of the radial velocity, when averaged separately, are equal in magnitude. The magnitude of the velocity at each shell can then be approximated as being the same, $v_{i+1/2} = v_{2N+1/2-i}$. With the density and velocities being equal across both streams, the surface area must also be equal across both streams. Another consequence of these approximations is that the mass of the cells in both streams at a given radius are also equal, $\delta m_i = \delta m_{2N+1-i}$.

3.3.3.3 Horizontal Mixing

With only the radial mass fluxes given by equation 3.6 contributing to equation 3.4 thus far, the only way in which the fluxes at the upper and lower boundary of any cell sum to zero is if the product of $2\pi r^2 \rho \vec{v}$ is constant for all radii. This is not true for the convection zone in the RAWD simulations nor in general. Rather, the spherically-averaged radial velocity profile from the 3D simulations in Fig. 3.2 shows a pronounced peak about $1/3^{\text{rd}}$ from the bottom of the convection zone and falls off well inside the convective boundaries where the flow turns around in a broad sweep corresponding to the low $\mathcal{M}a$ numbers.

Using Fig. 3.1 as a reference, if the upstream has $\alpha_{i+1/2} > \alpha_{i-1/2}$, then over a time step the mass within that cell i will decrease. Simultaneously the downstream will be increasing its mass by the same amount due to the fluxes being equal in the two streams at every layer (equation 3.10). To conserve the mass in each of the cells, there is an enforced horizontal mass flux of

$$\beta_i = \alpha_{i+1/2} - \alpha_{i-1/2} \tag{3.12}$$

from one stream to the other. The sign of this coefficient β determines whether mass is transferred from the downstream to the upstream or vice versa. The horizontal species mass flux at the upstream cell with index i is

$$F^{\beta}_{k,i} = \begin{cases} -|\beta_i| X_{k,2N+1-i} & \text{if } \beta_i > 0 \\ |\beta_i| X_{k,i} & \text{if } \beta_i < 0 \end{cases} \tag{3.13}$$

One could consider a situation where neighboring cells at the same radius conserve mass in the shell but allow for the mass in each cell to be variable so that the β coefficient is not exactly as written in equation 3.12. However, since the density fluctuations are at the percent level as shown in Fig. 3.3 they are approximated as being the same at every layer. Therefore the mass within each cell should not change due to horizontal mixing. Combining this fact with there being no net radial transport of mass, the mass within every cell is constant at all times and thus each cell has a horizontal species mass flux given by equation (3.4).

With the β and α mass fluxes, the total mass flux at every cell is zero. There can be additional horizontal mass fluxes so long as the sum of them is equal to zero. This additional horizontal mass flux is given the symbol γ and it is unique at each layer between shells, i.e $\gamma_i = \gamma_{2N+1-i}$, to ensure that the total mass flux at every cell is still zero. However, the additional horizontal species mass flux is not zero and has the form

$$F^{\gamma}_{k,i} = \gamma_i \left(X_{k,i} - X_{k,2N+1-i} \right) \tag{3.14}$$

for each cell.

While mass is being transported radially in the up- and down-streams, mass is also being exchanged between them through a horizontal mass flux. The mixing between of the mass of a given species k between cell i and its adjacent cell $2N+1-i$ implied by equation 3.14 has the effect of homogenizing the species between the two streams at every layer, depending on the value of γ. There are two competing timescales that determine how efficient the mixing between the up- and down-streams are. These are the radial advection timescale,

$$\delta t_{r,i} = \frac{|\delta r_i|}{v_{r,i}} \tag{3.15}$$

and the horizontal time scale, $\delta t_{h,i}$, for a given cell. Associated with these timescales are mass fluxes. The radial mass flux is α while the horizontal mass flux is γ. With these two competing timescales, if one is shorter than the other it is implied that the shorter timescale has a larger mass flux than the longer timescale. This can be written as

$$\gamma_i = \alpha_i \frac{\delta t_{r,i}}{\delta t_{h,i}} \tag{3.16}$$

The mental picture of a convection zone being composed of one upstream and one downstream that splits the convection zone evenly into two hemispheres is very unrealistic (Fig. 3.4). Instead, this model should be thought of as the upstream being the superposition of all radially upward flows and similarly for the downstream. From this idea, if the upward flows are small in their surface area at a given radius, they can more easily mix with the adjacent down flows. To decompose the velocity into upward and downward flows at a particular length scale on a sphere, the power spectrum (spherical harmonics) of the radial velocity is taken. To compute the spherical harmonics the python package `pyshtools` is used for data sampled on a sphere. The maximum ℓ mode that the velocity is decomposed into is chosen such that the smallest wavelength, $\lambda = 2\delta r$ where $\lambda = 2\pi r/\sqrt{\ell(\ell+1)}$, that can be sampled from the *briquette* data (see Fig. 3.4) with grid spacing of δr is computed.

For a given mode, ℓ, there is an associated length scale, or wavelength, $\lambda = 2\pi r/\sqrt{\ell(\ell+1)}$. A particle at the center of a stream must move, tangentially to the surface of the sphere, half of this wavelength to be in the center of the adjacent stream. With an average tangential velocity, the particle will take $\delta t_{h,i,\ell} = \pi r_i / \left(\langle|v_{\perp,i}|\rangle\sqrt{\ell(\ell+1)}\right)$ amount of time to mix, for a given mode ℓ. The flow does not develop with only one very dominant mode but a spectrum of modes (Fig. 3.6) and so the horizontal timescale is weighted by its power, $S_{cc}(\ell, r) = \sum_{m=-\ell}^{\ell} |c_{\ell,m}(r)|^2$. Therefore, the horizontal timescale is

$$\delta t_{h,i} = \sum_{\ell} \frac{S_{cc}(\ell, r_i)\pi r_i}{\left(\sum_{\ell} S_{cc}(\ell, r_i)\right)\langle|v_{\perp,i}|\rangle\sqrt{\ell(\ell+1)}} \tag{3.17}$$

3.3.3.4 Entrainment

A convection zone can entrain, or ingest, material due to hydrodynamic instabilities at the boundaries. This process can be included as an additional mass flux, the entrainment mass flux, to equation 3.4. However, with the limitation of requiring the mass for every single cell to be constant, the amount of mass that is being entrained must also be removed from that exact same cell. In the RAWD simulations, the entrained material has a composition that is significantly different than the composition of the convection zone. The $\mathcal{F}_1$ fluid is the entrained fluid, with a given composition, while the $\mathcal{F}_2$ is the convective fluid. The $\mathcal{F}_1$ fluid comes into the convection zone in a downstream, as shown in Figures 3.4 and 3.5. With only two fluids, the entrainment species mass fluxes are

$$F^e_{N+1,k=1} = \dot{M}_e \tag{3.18}$$

$$F^e_{N+1,k=2} = -F_{N+1,k=1} \tag{3.19}$$

where $\dot{M}_e$ is the entrainment mass flux of the $\mathcal{F}_1$ fluid into the convection zone.

3.3.3.5 The Courant Condition

With the fact that the method is explicit, the timesteps are limited by the Courant condition. With the cells being discretized in mass, the Courant condition can be plainly stated as requiring that the total amount of mass advected out of any given cell in a single timestep cannot be larger than the mass within that cell. The Courant number in any cell is given by

$$C_i = \frac{\delta t \left(\alpha_{i+1/2} + \gamma_i + |\beta_i|\right)}{\delta m_i} \tag{3.20}$$

and the Courant condition states that for all i, $C_i \leq 1$. Any post-processing simulations with this two-stream model have the condition that the maximum Courant number across all cells is 0.5. This determines the timesteps that the model takes.

3.4 Results

3.4.1 3D Hydrodynamic Simulations of RAWDs

3.4.1.1 Flow Properties

As with the other `PPMstar` simulations in Andrassy et al. (2018); Jones et al. (2017); Woodward et al. (2015), the RAWD simulations do not start with any initial perturbations in the velocity field but rather the numerical representation of the spherically symmetric thermodynamic variables develop instabilities. These are quickly over taken by the flow developing from heat being injected (Table 3.1) in a thick spherical shell. This shell is contained within the radii 8.28 Mm and 10.28 Mm and can be seen in Fig. 3.2. After about 15 minutes, this transient state is completely lost and the natural flow of the convection zone has developed.

The rms radial profiles of the radial and tangential velocities are shown in Fig. 3.2. The radial velocity drops sharply near the convective boundaries (CB's) while the tangential velocity is dominant near the CB's. Directly from these profiles it is clear that there will be significantly more horizontal mass transport near the CB's (equation 3.16) than the middle of the convection zone. This coincides with the flows being forced to turn over near the CB's. `N15`'s spherically averaged velocities are smaller than `N16`'s and it is significant when considering that the difference between the two runs is the doubling of the spatial resolution in `N16`. A possible cause for this is due to the significantly higher entrainment rates in `N15` compared to `N16`, shown in Fig. 3.10. With the convective fluids doing work to bring the initially stable $\mathcal{F}_1$ fluid into the convection zone, some of its kinetic energy is lost resulting in the lower velocities.

The radial velocity field is shown at two radii in Fig. 3.4. These mollweide-projection plots are made using the *briquette* data from a `PPMstar` simulation. This data set is downsampled by a factor of four in each spatial direction through averaging the `PPMstar` simulation. The radial velocity at 14.5 Mm is mostly dominated by two modes, $\ell = 2$ and 3, which can be seen visually in Fig. 3.4 as well as from its power spectrum in Figures 3.6 and 3.7. This is consistent with the flow being dominated by the most unstable and largest convective mode that can be in that spherical shell, $\ell \approx \pi r/\Delta r \approx 3$ (Chandrasekhar, 1961). At 23.5 Mm, the velocity field is not dominated by a few modes but the power is instead spread over many modes of ℓ. The large plumes that are advecting from the center of the convection zone are broken up into smaller, incoherent streams that are swept across by the large tangential

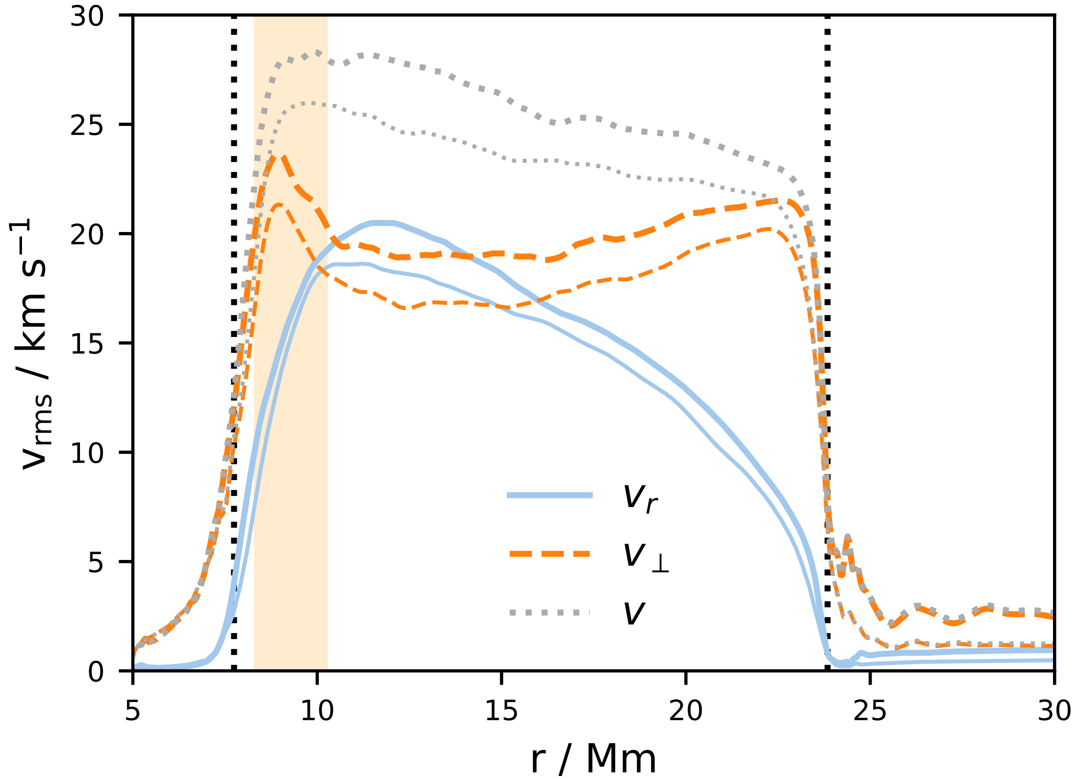

Figure 3.2: The rms radial profiles of v_r, $v_\perp$ and v at $t = 299$ min. The thick lines are from run `N16` while the thin lines are from run `N15`. The black dotted lines correspond to the convective boundaries that are used in `N16`'s stream model post-processing (Sections 3.4.1.2 and 3.4.2.2). The beige shaded region is where the volume heating is applied. When integrated, it corresponds to the helium luminosity, L_{He}, stated in Table 3.1.

velocities (Figures 3.2 and 3.8).

3.4.1.2 The Convective Boundary and Entrainment and Burning of H

The CB in 1D stellar evolution models can be determined by the Schwarzschild criterion. If the fluid is unstable to convection, the convection zone, after mixing, is adiabatically stratified such that $dS/dr = 0$, or in the case of an ideal gas equation state which is used for the simulations done in this paper, it can be expressed as $dA/dr = 0$ where $A = P/\rho^\gamma$. The `PPMstar` simulations are initialized with a convection zone defined by these properties. In previous works using the `PPMstar` code, Andrassy et al. (2018); Denissenkov et al. (2019); Jones et al. (2017), the CB during

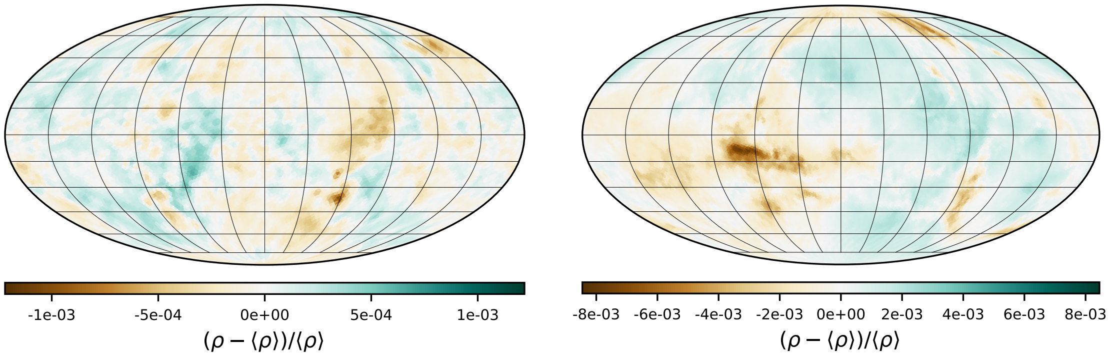

Figure 3.3: The perturbation of the density from its mean on spherical shells for `N16`. The left panel is at a radius of 14.5 Mm, within the H burning region (Fig. 3.16), while the right panel is at a radius of 23.5 Mm which is near the upper convective boundary. These snapshots are taken at $t = 299$ min. The largest perturbations are at the percent level.

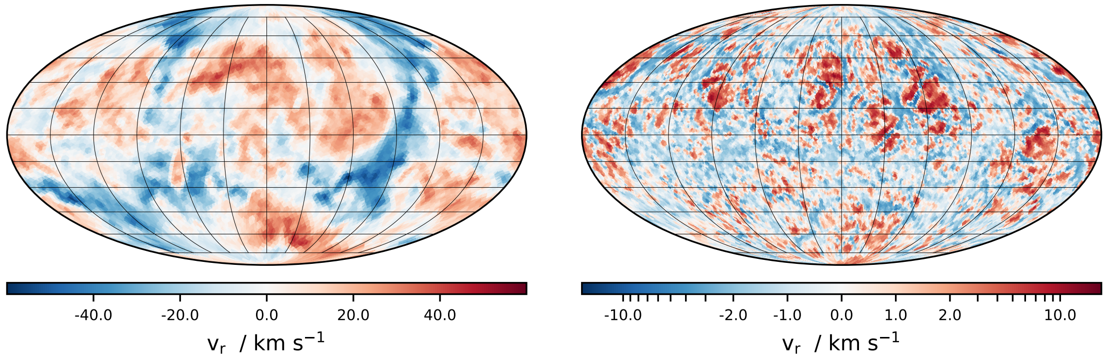

Figure 3.4: The radial velocity component on spherical shells from `N16`. The left panel is at a radius of 14.5 Mm, within the H burning region (Fig. 3.16), while the right panel is at a radius of 23.5 Mm which is just below the upper convective boundary. These snapshots are taken at $t = 299$ min. These plots were made with the *briquette* data which is downsampled by a factor of 4 (384^3) from the resolution of run `N16` (1536^3). The 16000 points on the sphere to which the velocities are calculated are distributed such that each point's surface area coverage is roughly equal to $4\pi/N$. This is well below sampling within every cell on these shells and is only used for plotting purposes.

the simulation was determined using the minimum of $\partial v_\perp/\partial r$ with the spherically averaged profiles of $|v_\perp|$. The Schwarzschild criterion does not adequately describe the stability of the fluid near the boundaries in these simulations as even in areas where the entropy gradient is weakly positive, the fluid is flowing with moderate ve-

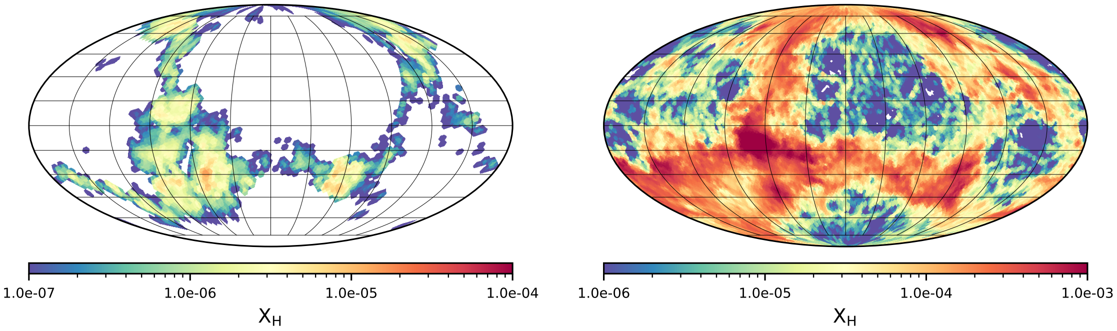

Figure 3.5: The H mass fraction, X_{H}, on spherical shells from `N16`. The left panel is at a radius of 14.5 Mm, within the H burning region (Fig. 3.16), while the right panel is at a radius of 23.5 Mm which is near the upper convective boundary. These snapshots are taken at $t = 299$ min. This plot uses the fractional volume, FV, with which the H mass fractions are derived from, that is at half the grid resolution.

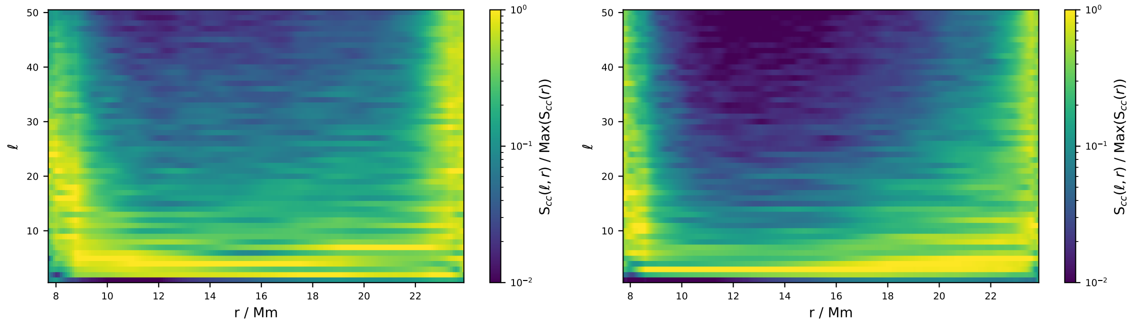

Figure 3.6: The power spectrum, in terms of the spherical harmonic modes, ℓ, of the radial velocity as a function of radius at $t = 299$ min within the convection zone. The left panel is from run `N15` while the right panel is from run `N16`. The power in each radial bin is normalized by the maximum power within that radial bin.

locities (Jones et al., 2017). The gradient condition expresses the 3D nature of the CB as when the fluid advects near the stiff boundary, the fluid is forced to turn over. This can be viewed as small perturbations from a spherically symmetric boundary. In Fig. 3.9, the thickness of the CB of `N16` as described by 1σ spatial fluctuations (Fig. 17 in Jones et al., 2017) is approximately 0.3 Mm, which is smaller than the pressure scale height at that boundary, $H_P = 0.9$ Mm. At $t = 299$ minutes, the top of the convection zone as determined with the spherical average of the minimum of $\partial v_{\perp}/\partial r$ is equal to 23.69 Mm. For reasons discussed in Section 3.4.2.2, the CB across time can also be determined by following the initial Schwarzschild boundary at the start of the simulation in Lagrangian coordinates. This initial Schwarzschild boundary is

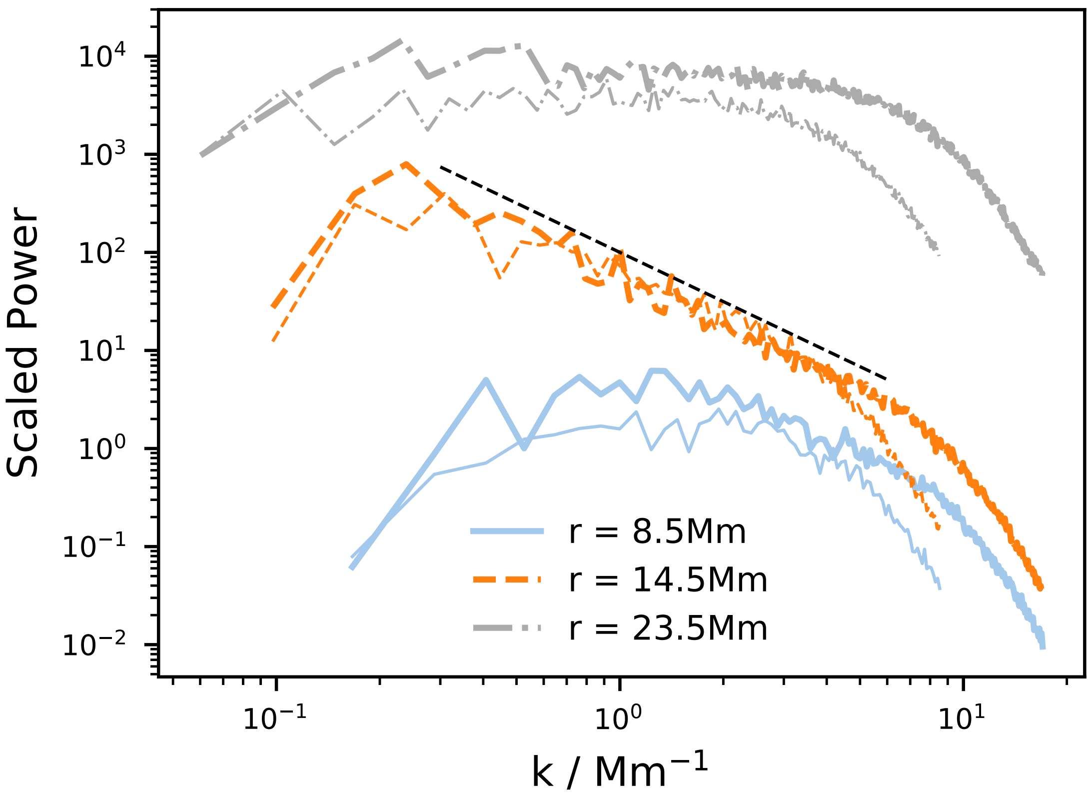

Figure 3.7: The power spectrum as a function of the wavenumber, k, of the radial velocity at select radii at $t = 299$ min. The thick lines are run `N16` while the thin lines are from run `N15`. The spectrum is limited by the Nyquist sampling of the *briquette* data resulting in a larger maximum wavenumber reached in the higher resolution run, `N16`. The power in each spectra at a given radius are scaled to show their k dependence clearly. The black dashed line is proportional to $k^{-5/3}$ for reference.

determined numerically with the condition that fluid with $dA/dr \neq 0$ is stably stratified. This definition of the CB for all runs at $t = 299$ min as well as the CB as determined by the minimum of $\partial v_{\perp}/\partial r$ are tabulated in Table 3.1.

At the upper CB, the entrained $\mathcal{F}_1$ fluid follows the convective downflows deep into the convection zone until it reaches the burning region where the $^{12}\mathrm{C}(p,\gamma)^{13}\mathrm{N}$ reaction occurs. To determine the entrainment rates of the burning runs, `N15`, `N16` and `N17`, a method, which is described in more detail in Andrassy et al. (2018) and Denissenkov et al. (2019), was used. To summarize, the mass of the $\mathcal{F}_1$ fluid that was entrained is composed of the mass that was burned and the mass that is present within the convection zone that has a boundary radius of r_{ub}. The density of the

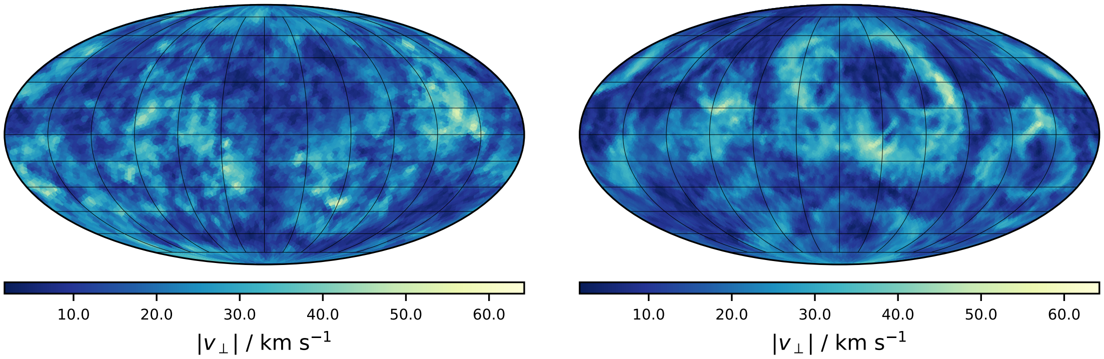

Figure 3.8: The magnitude of the tangential velocity, $|v_\perp| = \sqrt{v_\phi^2 + v_\theta^2}$, on spherical shells from `N16`. The left panel is at a radius of 14.5 Mm, within the H burning region (Fig. 3.16), while the right panel is at a radius of 23.5 Mm which is near the upper convective boundary. These snapshots are taken at $t = 299$ min.

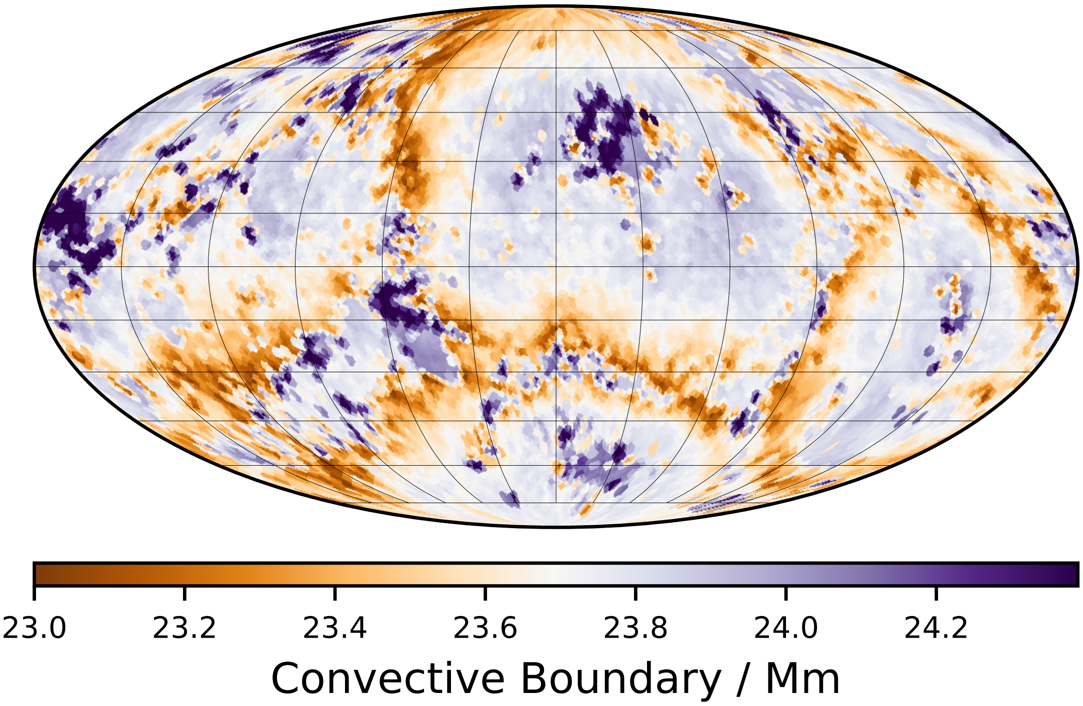

Figure 3.9: Location of the upper convective boundary of `N16` according to the minimum of $\partial v_\perp / \partial r$ at $t = 299$ min. Taking the spherical average, the upper convective boundary is at 23.69 Mm while the boundary that is calculated from the `PPMstar` initialized Schwarzschild criterion that is followed in Lagrangian coordinates is at 23.84 Mm (discussed in Section 3.4.2.1).

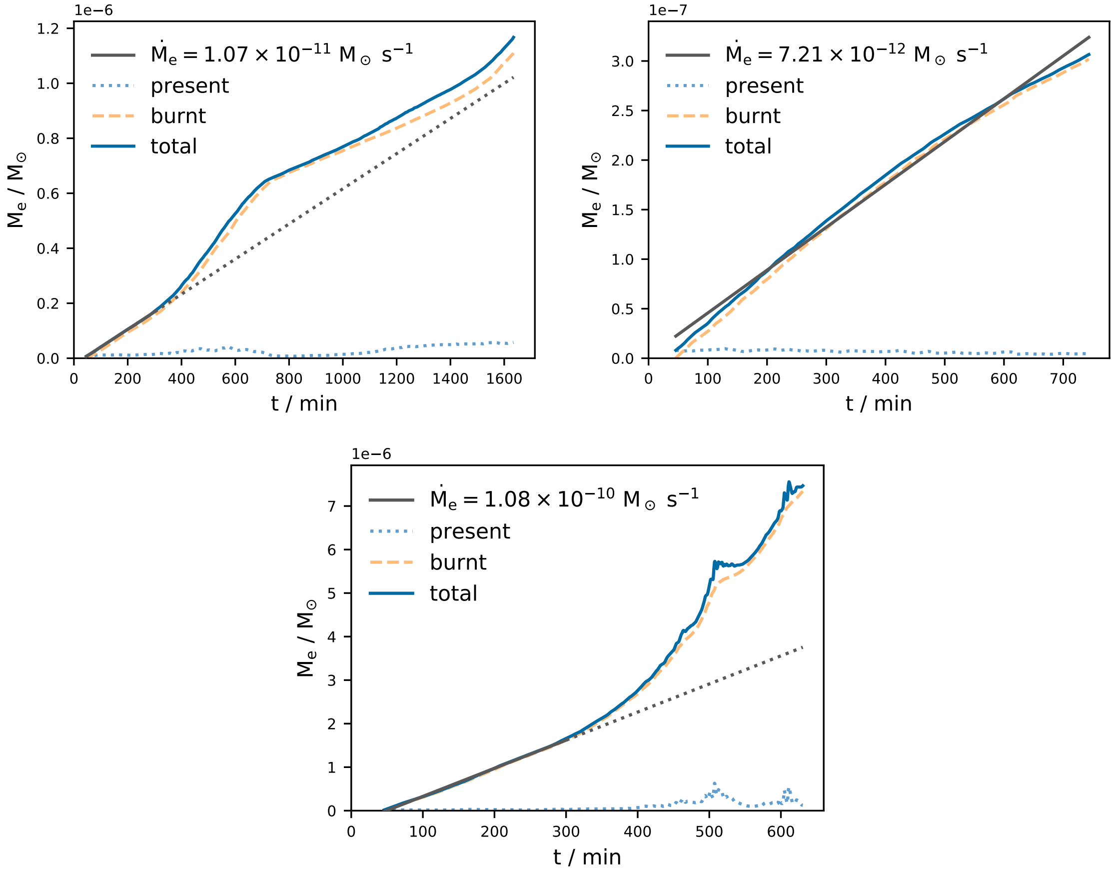

Figure 3.10: The time evolution of the mass of the $\mathcal{F}_1$ fluid being entrained, burned and retained within the convection zone after a simulation time of $t = 46$ min. The top panel is from `N15`, the middle panel is from `N16` and the bottom panel is from `N17`. $\dot{M}_e$ is the rate that the $\mathcal{F}_1$ fluid is being entrained into the convection zone and its instantaneous value is used in the entrainment of said fluid in the advective and diffusive post-processing models. A linear fit of the entrainment rates for each run is calculated over a time interval corresponding to the solid line while the dotted line is an extension of that fit. This is during the quasi-static phases of each run. A GOSH occurs in `N15` and `N17` leading to a runaway burning and entrainment in `N17` but not `N15` which stabilizes after $t = 700$ min (Fig. 3.11).

reactant fluid is integrated to within 0.5 Mm of the CB which is approximately the average scale height of the rms tangential velocity gradient at the boundary, $H_{v_\perp,\mathrm{ub}} = (\partial \ln v_\perp / \partial r)^{-1}$, for all RAWD simulations during their quasi-static burning phases. This constant offset prevents minor fluctuations in the calculated entrained mass due to the very large concentrations of the $\mathcal{F}_1$ fluid near the CB and prevents major changes in the velocity field (GOSH in `N15` and `N17`) from providing outlandish integration boundaries. This offset is extended to 5 Mm for `N17` during its GOSH due to the major changes in the spherically averaged $\mathcal{F}_1$ concentrations near the majorly perturbed convective boundary. The burnt material is calculated using the spherical profiles of density, temperature and mass fraction to determine what the burning rate per unit volume is. This burning rate is integrated in time to determine the amount burnt over a *dump* (see Section 3.4.2.1). The entrainment rates, mass burnt, and present material of the $\mathcal{F}_1$ fluid within the CB's of `N15`, `N16` and `N17` are shown in Fig. 3.10. A linear fit of the entrainment rate of `N15`, `N16`, and `N17` over their quasi-static burning phases are $\dot{M}_{\rm e} = 1.07 \times 10^{-11}\,{\rm M}_\odot\,{\rm s}^{-1}$, $\dot{M}_{\rm e} = 7.21 \times 10^{-12}\,{\rm M}_\odot\,{\rm s}^{-1}$, and $\dot{M}_{\rm e} = 1.09^{-10}\,{\rm M}_\odot\,{\rm s}^{-1}$, respectively. `N15` and `N17`'s entrainment rates become non-linear and increases significantly around $t = 300$ min (see Section 3.4.1.3). Even within the linear regime the entrainment rate of `N15` is $\approx 10\%$ larger than `N16`'s though the scale of this difference is consistent with the entrainment convergence results of Woodward et al. (Fig. 17 in 2015).

Throughout the entirety of the `N16` simulation, the burning and entrainment of H maintains a quasi-stationary state resulting in the linear growth of the total entrained material. The distribution of $X_{\rm H}$ is plotted on spherical shells near the convective boundary, 23.5 Mm, and within the start of the H burning region, 14.5 Mm, in Fig. 3.5. The corresponding radial velocity field at those radii is shown in Fig. 3.4. The distribution of the $X_{\rm H}$ at 23.5 Mm in conjunction with the radial velocity distribution shows that that the upflows are essentially H-free while the downflows are H-rich. As the H-rich material moves through the H burning region, the downflow material is rapidly burned until it is H-free. Eventually this material will turn around and move in the upflow H-free. The H-free material is advected and mixed with the H-rich material as it is advected towards the upper boundary where it still maintains very small mass fractions ($X_{\rm H} \approx 10^{-6}$) at 23.5 Mm, ≈ 0.3 Mm from the upper CB (Table 3.1). The H-rich material ($X_{\rm H} \approx 10^{-3}$) is advected into the convection zone in the downflows near the CB.

3.4.1.3 GOSH in `N15` and `N17`

Directly from the entrainment rates of each run in Fig. 3.10, the entrainment rates begin to increase substantially around $t = 300$ min in both `N15` and `N17` and continues until $t \approx 700$ min. `N17`'s entrainment rate increases by a factor of up to 40 during this time compared with its quasi-static rate while `N15`'s entrainment rate increases

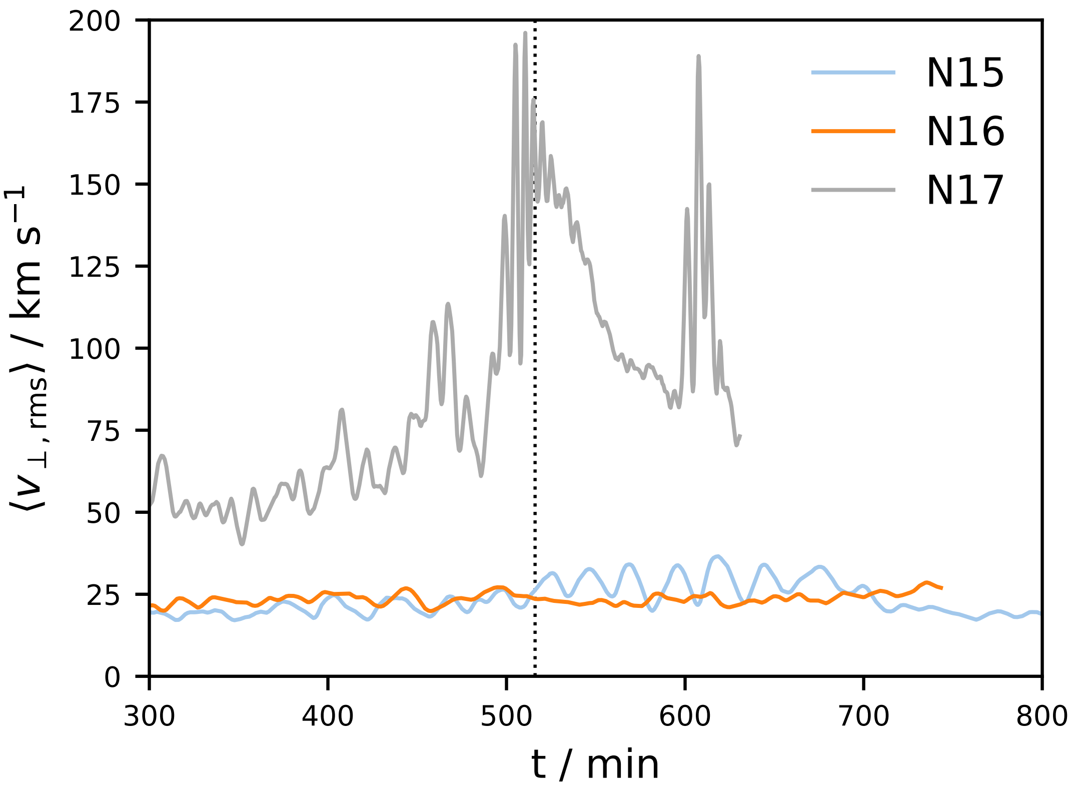

Figure 3.11: The average of the rms tangential velocity between 1 and 2 Mm below each simulations Schwarzschild boundary as described in Section 3.4.1.2. The very large oscillations in the tangential velocity in `N17` indicate a GOSH is occurring which causes the entrainment rate to increase by up to a factor of 100 (see Fig. 3.10) during these oscillations. Much milder oscillations can be seen in `N15` between 500 and 700 min with a modest factor of 3 increase in its entrainment rate. The black dotted line refers to the time of the renderings of the FV in Fig. 3.12.

by a factor of up to 3. The cause of these bursts of entrainment are due to the collision of opposing horizontal flows forcing significant amounts of H-rich material to be entrained in downdrafts where it will eventually burn and feedback energy into the flow (Herwig et al., 2014). The magnitude of the horizontal oscillations of these flows is clearly seen in Fig. 3.11 where the rms of the tangential velocity rapidly increases and decreases within convective turn over timescales. With the same heating rate as `N15`, `N16` does not undergo a GOSH at any point during its entire simulation which includes the full duration of the GOSH experienced by `N15`.

The consequences of the GOSH between `N15` and `N17` differ drastically due to the

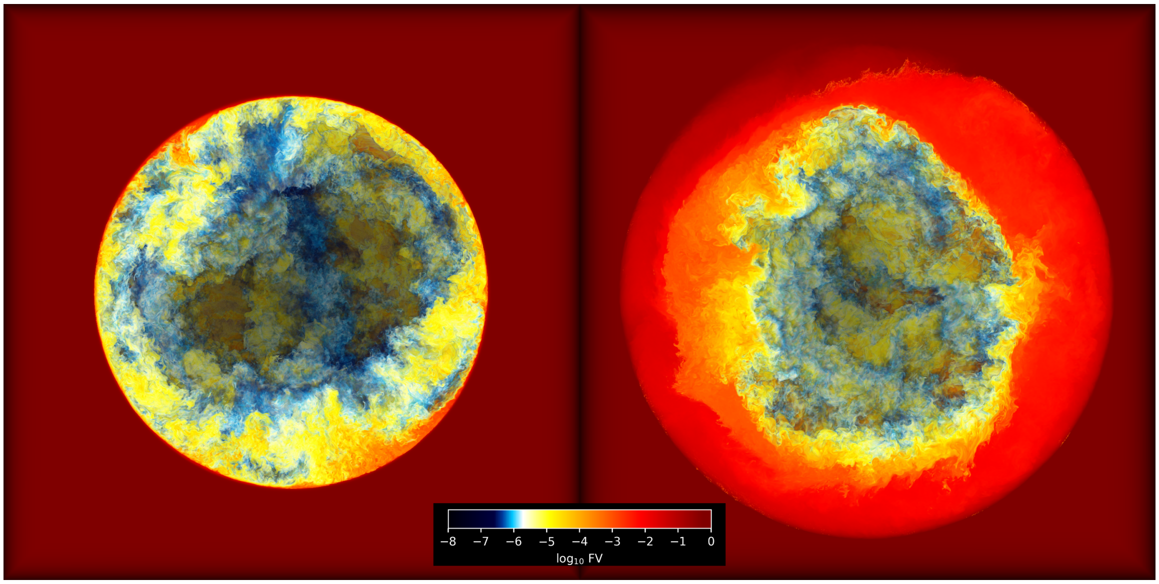

Figure 3.12: Both panels show a rendering of the FV at $t = 516$ min into the simulations. The left panel is from `N16` while the right panel is from `N17`. The entrainment rate of H rapidly increases when a GOSH instability occurs in `N17`. The hydrodynamic feedback from the energy released from burning causes even more H to be entrained and leads to an unstable runaway in `N17` but not in `N15`. This is contrasted with the quasi-static entrainment and burning in the higher resolution run of `N16` (Fig. 3.10).

differences in the amount of H ingested. The weak GOSH of `N15` does not entrain enough H to sustain it for a long period of time and thus it dissipates after 200 minutes of large scale oscillations. The burning of this additional entrained H is done such that there is very little build up of H within the convection zone (Fig. 3.10) during the GOSH. The GOSH does not increase the average tangential velocity significantly over its duration and a GOSH does not occur again throughout the 1600 minute long simulation. Conversely, `N17`'s GOSH causes significantly higher entrainment of H which is built up within the convection zone. This can be seen in the rendering of the fractional volume, FV, at $t = 516$ min in Fig. 3.12. The GOSH subsides briefly after the large build up of H and burns most of the H within the convection zone and then begins again at $t = 600$ min. The simulation is ended soon after the GOSH continues again as the expansion of the convection zone has begun to approach where the outer boundary condition is applied.

3.4.2 Advective Post-Processing

3.4.2.1 The RAWD Stream Model Constraints

Due to the initial transient at the start of any `PPMstar` simulation, the advective post-processing model does not begin until well after this transient has finished. This was chosen to be at 46 minutes for `N15`, `N16` and `N17`. The model is initialized with a X_{H} profile in the up- and down-streams that is equivalent to the spherically averaged X_{H} profile from the `PPMstar` simulation. As the post-processing begins, the initial guess of the profiles in the up- and down-streams is very quickly changed to the model's preferred profile. This takes around 5 convective turn over timescales and causes the diagnostics of the stream model, the burning rates and total mass of H burned, to deviate from the `PPMstar` profiles during this initialization period. For this reason, the stream model repeats the very first time step, with the entrainment rate at that point in time, until it establishes its own quasi-static profile. The radial profiles of the up- and down-streams that the stream model establishes is asymmetric as expected from the `PPMstar` simulation (Fig. 3.5) and `N16`'s is shown in Fig. 3.13.

The `PPMstar` simulations output the *briquette*, and any other data type, on a *dump* period which is a few thousand time steps. With the stream model being limited by the Courant condition, equation 3.20, there are, on the order of 20-30 post-processing timesteps being taken for every single *dump*[2]. The stream model uses the same stellar stratification and velocity profile for every timestep within a single *dump*. Although the stratification and velocity profile do change over *dumps*, it is negligible as the convective turn over time is $\approx$ 1000 s for `N16` while the dump interval for all runs is $\approx$ 26 s.

As discussed in Section 3.4.1.2, the CB in the 3D hydrodynamic simulations is not a sharp and spherically symmetric boundary as typically interpreted with the Schwarzschild criterion. The minimum of the spherical average of $\partial v_{\perp}/\partial r$, which can define the location of the CB, could be used to determine a time dependent CB for the stream model. However, the stream model requires that the mass of the convection zone and the mass of the individual cells must remain constant across all time (Section 3.3.3). Using the minimum of $\partial v_{\perp}/\partial r$ as the definition of the CB does not guarantee that the mass of the enclosed convection zone to be constant at all times. Complicating this further, the convection zones of the simulations are expanding and therefore the CB must be followed at all times in the Lagrangian

---

[2] `PPMstar`'s Courant condition is based on the speed of sound

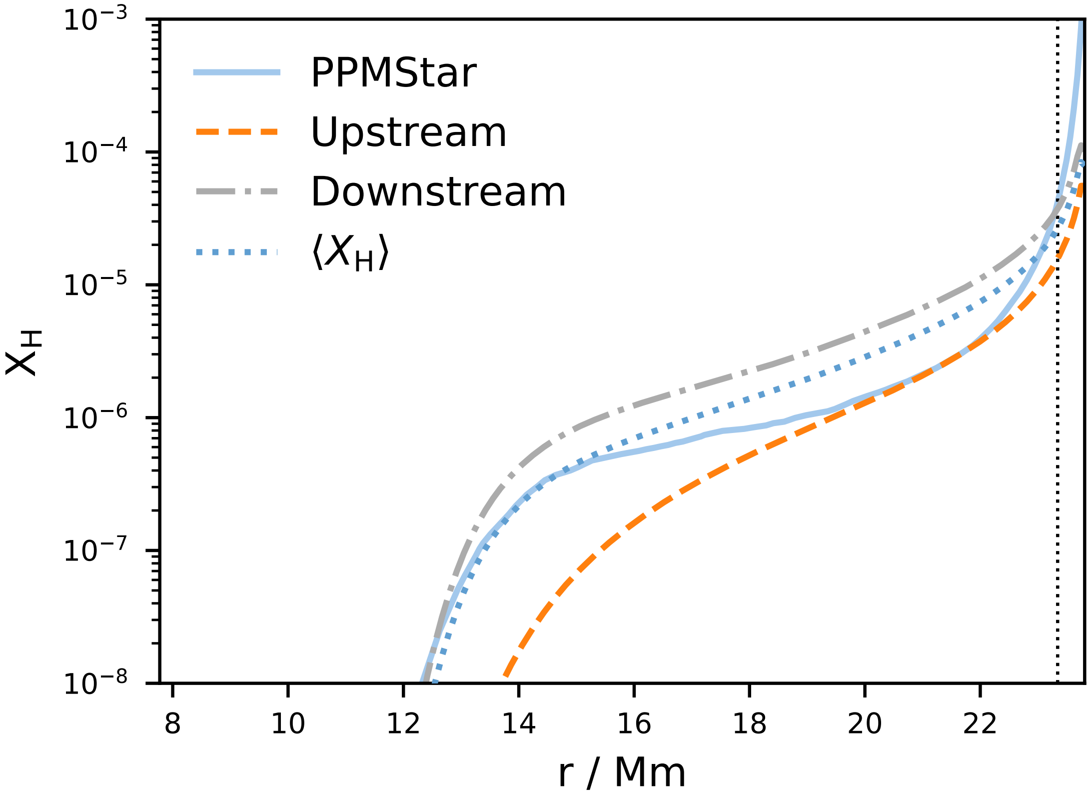

Figure 3.13: The $X_{\rm H}$ profiles from `PPMstar` and the up- and down-streams of the advective post-processing model for `N16` at $t = 299$ min. The spherical average of the up- and down-streams is $\langle X_{\rm H} \rangle$. The black vertical dotted line is where the integration of the $\mathcal{F}_1$ fluid is stopped for calculating the entrainment rates in Fig. 3.10.

coordinates. To simplify the definition of the CB, the Schwarzschild criterion at the bottom and top of the convection zone at the start of the simulation are used to define the convection zone for the stream model. These boundaries are followed in the Lagrangian coordinates as the convection zone expands. The difference between the two boundary criteria is only 0.15 Mm at $t = 299$ min for `N16` (Table 3.1). Given that the determination of the tangential velocity gradients are from the *briquette* averaged data with a resolution of 0.18 Mm, the two boundary determinations are equivalent to within one *briquette* cell.

The mass coordinates of the cell interfaces, which are constant for the whole duration of the post-processing, are calculated by initially splitting the convection zone into equally spaced radial shells in the Eulerian coordinates. This makes the mass of individual cells to vary radially but this ensures that the sampling of data from the hydro simulations is done at the cell resolution. This results in about 175 and 350 cells for the post-processing of `N15` and `N16`, respectively. As the `PPMstar` simulation evolves in time, the density, velocity and radius are interpolated to the mass coordinates of the cell interfaces.

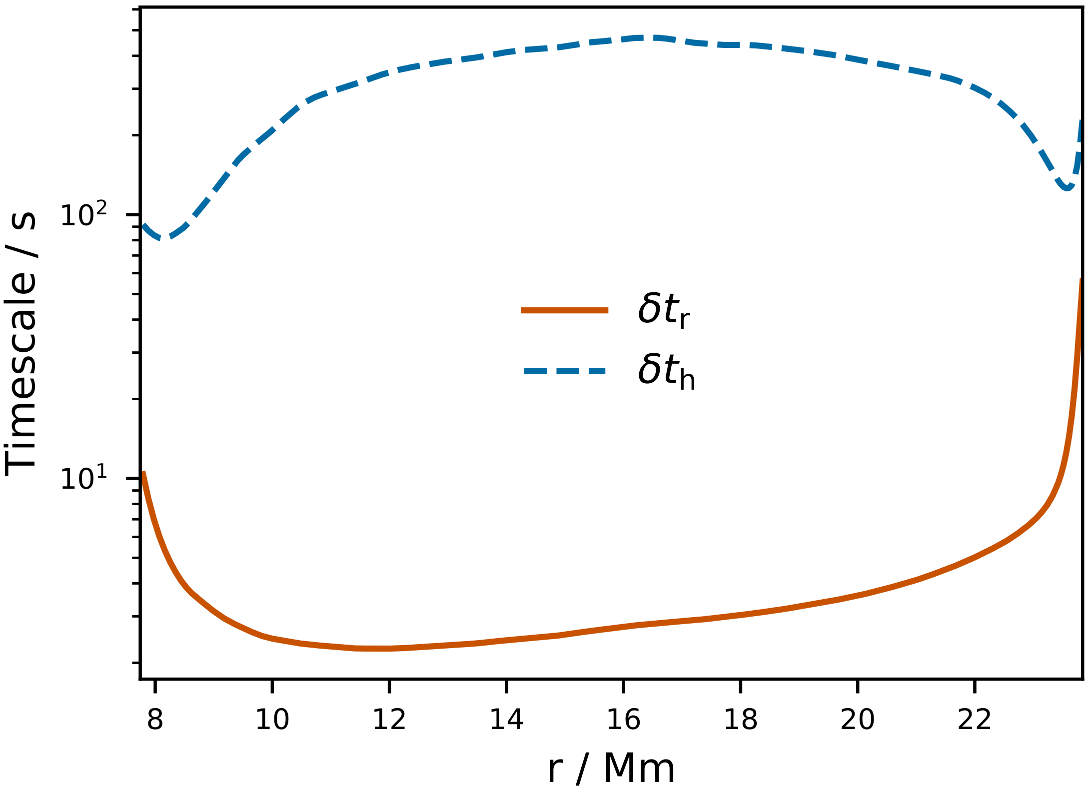

Figure 3.14: The radial and horizontal mixing timescales as a function of radius within the convection zone at $t = 299$ min for run `N16`. Equations 3.15 and 3.17 define the radial and horizontal mixing timescales.

The stream model for `N16` was run from $t = 46$ min until the end of that simulation at roughly $t = 744$ min resulting in roughly 42 convective turn over times. The entrainment of the $\mathcal{F}_1$ fluid into the stream models convection zone is taken directly from the time dependent entrainment in Fig. 3.10. The entrainment rates are small enough that the fact that the mass of the convection zone does not change over the any of the stream models timesteps is an accurate approximation to the `PPMstar` simulations. Integrating `N16`'s entrainment rate over the length of its simulation results in a total of $3.1 \times 10^{-7}\,\mathrm{M}_\odot$ of $\mathcal{F}_1$ fluid being entrained. The cell with the smallest mass within the stream model of `N16` is $4.1 \times 10^{-6}\,\mathrm{M}_\odot$.

3.4.2.2 RAWD Advective Post-Processing

Directly from the radial velocities on spherical shells, a normalized power spectrum is shown for runs `N15` and `N16` in Fig. 3.6. The power near the upper and lower CB's is spread across many scales while the power near the middle of the convection zone assumes a Kolmogorov-like spectrum (Fig. 3.7). With the smaller modes contributing significantly to the power near the CB's the mixing between the two streams is expected to be more efficient there. The `N15` and `N16` have qualitatively similar profiles for their power spectra showing dominant large modes at the middle of the convection zone and the spectra being flat over many scales at both CB's.

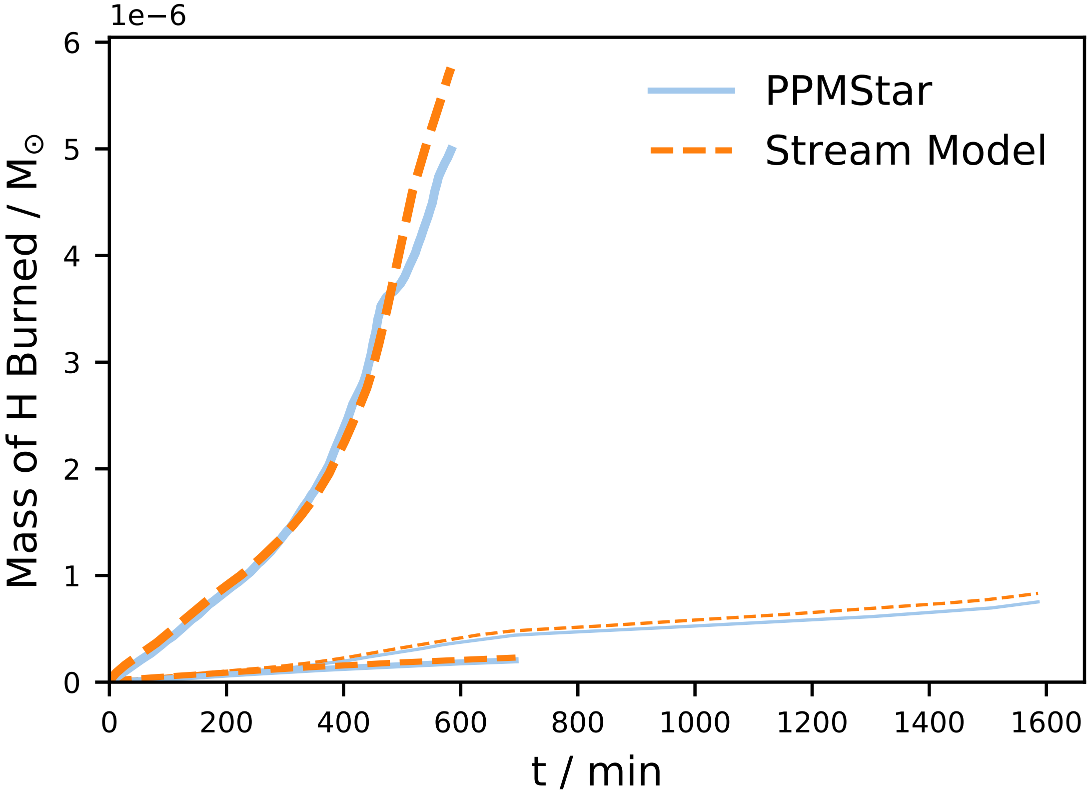

Figure 3.15: The total mass of H burned throughout the `PPMstar` and stream model simulations starting at $t = 46$ min. The thickest lines are from run `N17`, the medium sized lines are from run `N16` while the thin lines are from run `N15`.

Applying equation 3.17, the horizontal and radial timescales for run `N16` are shown in Fig. 3.14. The horizontal timescale is typically over an order of magnitude larger than the radial timescale suggesting inefficient mixing, even at the CB's. There is still significant power at the largest modes near the CB's leading to small changes in the horizontal timescales across the entire convection zone. The lack of efficient horizontal mixing is especially apparent in the middle of the convection zone where the up- and down-streams are very isolated from each other as seen in Fig. 3.13. The upstream is carrying nearly H-free material towards the top of the convection zone while the downstream is carrying H-rich material directly to the burning region. This distribution of H-free fluid in the upstream and H-rich fluid in the downstream is also validated by the 3D hydro simulations in Figures 3.4 and 3.5.

The spherical average of the two streams closely follows the spherical average of `N16` in all regions except near the top CB. At the very top of the convection zone it is underestimated while between 16 and 22 Mm it is overestimated. One component of this is likely due to an underestimation of the horizontal mixing at the top of the convection zone in the advective post-processing. The *briquette* data used to compute the spectra of the radial velocity has a resolution that is a factor of 4 smaller than the run's grid resolution. This downsampling involves averaging which significantly dampens the power in any short wavelength modes, directly increasing the horizontal mixing timescale and leading to less efficient mixing. Though, this is counteracted to some degree by the spherical averages of the horizontal velocities containing components due to internal gravity waves (Jones et al., 2017). This results in much more efficient radial transport of species allowing for the sliver of very H-rich material at the top of the convection zone to immediately advect downwards rather than be constantly mixed between the two streams.

The time evolution of the total mass of H burned for `N15`, `N16` and `N17` is shown in Fig. 3.15. With the repeating of the first time step for 5 convective turn over times, the post-processing model follows the `PPMstar` evolution closely. Even from the GOSH events in `N15` and `N17` (Section 3.4.1.3) the stream model post-processing adjusts its burning rate from the sporadic entrainment of H to yield the correct total mass of H being burned.

In the interest of nucleosynthesis calculations, it not only matters what the total mass of H that is burned but also where this burning is occurring within the He-shell and its rate. The H burning rate at a single time step from the `PPMstar` simulations and the stream model are estimated in `N16` with the techniques discussed in Section 3.4.1.2. These burning rates were integrated in order to estimate the total mass of H burned in `PPMstar` and the stream models. The burning rates can be seen in Fig. 3.16. The stream model is burning the H a few cells above where `N16` is burning H. This could suggest that the distribution of flow speeds that are present in `PPMstar`

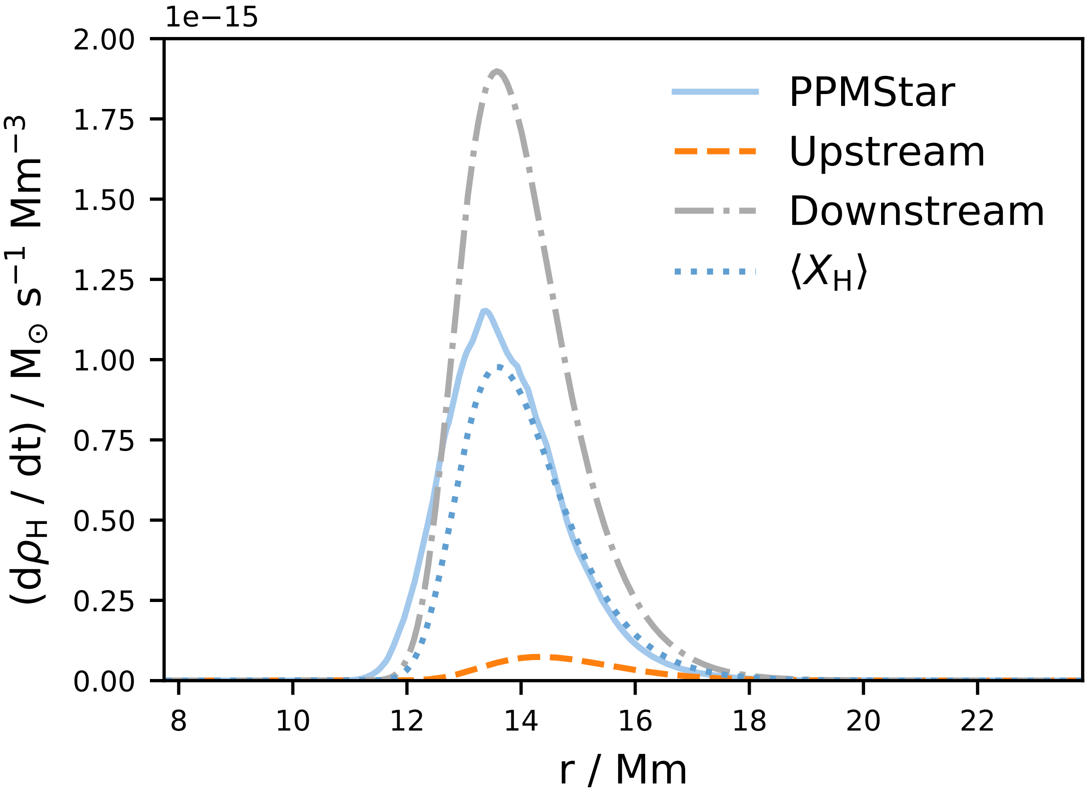

Figure 3.16: The burning rate of H per volume as a function of radius for `N16` and its advective post-processing model. The $\langle X_{\mathrm{H}} \rangle$ profile is from the advective post-processing model where the spherical average of the streams is used to estimate the burning rate, similarly to `PPMstar`. The $^{12}\mathrm{C}(p,\gamma)^{13}\mathrm{N}$ reaction is very sensitive to temperature and it does not burn any H until about 18 Mm with $\mathrm{T9} = 0.11$. All of the H is burned well before it reaches the bottom of the convection zone.

simulation modify where the bulk of the burning takes place within a convection zone from the spherical average. However, since the total mass of H that was burned are roughly the same in the `PPMstar` and stream model simulations, the space and time integrals of the burning rates shown in Fig. 3.16 must be the same throughout the length of the stream model.

3.5 Summary and Conclusions

In this paper, we described two different numerical methods to quantify the mixing within a convection zone from 3D hydrodynamic simulations. The stellar environment of choice was the He-shell in a RAWD with a metallicity of $[\mathrm{Fe/H}] = -2.6$ (model

G of Denissenkov et al. (2019)). One method was using a standard 1D diffusive mixing routine while the other was a two stream advective mixing model (Cannon, 1993; Henkel et al., 2017). These models require mixing coefficients which could be taken from estimates using MLT however instead we constrain the mixing by running 3D hydrodynamic simulations of the RAWD. The mixing coefficients are determined directly from the data of the 3D hydrodynamic simulations.

The high resolution RAWD simulation, `N16`, was run for more than 42 convective turn over times showing that its evolution in the entrainment and burning is approximately quasi-static. The radial velocity field at 14.5 Mm is dominated by the large modes of $\ell = 2$ and 3 while near the convective boundaries the flow is spread across many small modes (Figures 3.4 and 3.6). The large scale modes encounter the stiff upper boundary and begin to turn over, increasing the tangential velocities near the boundaries (Fig. 3.2). Using the gradient of the tangential velocity as a condition for the convective boundary yields a spherically averaged boundary at 23.69 Mm at $t = 299$ minutes. This convective boundary is consistent with the convective boundary as determined by the initial Schwarzschild boundary of the 3D simulations, which is followed in the Lagrangian coordinates, to within the resolution of the *briquette* data that was used to calculate both boundaries.

The entrainment of $\mathcal{F}_1$ fluid in `N16` is linear in time with an entrainment rate of $\dot{M}_\mathrm{e} = 7.21 \times 10^{-12}\,\mathrm{M}_\odot\,\mathrm{s}^{-1}$ while `N15` has an entrainment rate of $\dot{M}_\mathrm{e} = 1.07 \times 10^{-11}\,\mathrm{M}_\odot\,\mathrm{s}^{-1}$. `N15`'s entrainment rate increases by as much as a factor of 3 after it experiences a GOSH however it returns to quasi-static burning as shown in Fig. 3.10. The GOSH instability sets `N17` into a feedback loop of rapidly increasing entrainment which does not return to quasi-static burning. The entrained H-rich fluid is advected along the downflows to be burned rapidly at 14 Mm while the heavier, H-free fluid is advected along the upflows. These two fluid mixtures are nearly isolated from each other as there is a significant amount of H-free fluid with $X_\mathrm{H} \leq 1 \times 10^{-6}$ very close to the upper boundary, 23.5 Mm, while the spherical average is $X_\mathrm{H} \approx 1 \times 10^{-3}$ in the `PPMstar` simulations.

The advective post-processing models were calibrated by repeating the first timestep for 5 convective turn over times. This allowed the two streams to lose their initial spherically symmetric profiles and develop their own quasi-static profiles. The total mass of H burned closely follows the evolution of the quasi-static burning of `N16` and the GOSH's of `N15` and `N17`. At $t = 299$ min, the instantaneous H burning rates in `N16` are estimated and compared with its advective post-processing model where they are in excellent agreement in where the bulk of the burning occurs. The up- and down-streams horizontal mixing timescales are 1-2 dex longer than the radial mixing timescales resulting in the streams not homogenizing. Each stream has a distinct X_{H} radial profile that is qualitatively similar to `N16`'s distribution of H-free upflows and H-rich downdrafts though not of the same magnitude. The spherical average of the two streams is consistent with the `PPMstar` X_{H} profiles except at the upper boundary where it is underestimated. The difficulty in quantifying the convective boundary, the inclusion of wave velocity contributions to the spherical averages of the velocities and the spatial averages done in the *briquette* data are possible sources of this discrepancy (see Section 3.4.2.2).

A limitation of the advective post-processing is the fact that the numerical scheme has to be explicit. This limits the application of said model to only particular situations in the stellar evolution context. With this in mind, there are many interesting cases where the timescales of the dynamics and mixing coincide in evolved states of massive stars. One such example is C-ingestion into a O-shell of a $25\,\mathrm{M}_{\odot}$ star which could be a production site for odd Z elements significant enough to influence galactic chemical evolution of said elements (Côté et al., 2018; Ritter et al., 2018a). The many different burning layers of (γ, p) and (p, γ) that produce the odd Z elements may be sensitive to the exact nature of the mixing of these species throughout the burning regions. The non-linearity of the $^{12}\mathrm{C}+^{12}\mathrm{C}$ burning could lead to an interesting differences in the burning between the two streams (Andrassy et al., 2018). Another interesting example of convective-reactive nucleosynthesis via the $^{12}\mathrm{C}(p,\gamma)^{13}\mathrm{N}$ and subsequent $^{13}\mathrm{C}(\alpha,n)^{16}\mathrm{O}$ reactions is Sakurai's object in which a GOSH occurs (Herwig et al., 2014).

4

The *i*-process within a RAWD

Attribution

The text of this chapter was written solely by me. In order to model the *i*-process within the RAWD I needed to add my advective mixing model to the `mppnp` code which I have previous experience in from a class project. For that purpose I translated the original *python* advective mixing code into Fortran. The Fortran code is hosted on Github, `https://github.com/David-Stephens/two-stream-mixing`. I had extracted from the 3D RAWD simulations the required mixing data for 1D post-processing.

Pavel Denissenkov implemented my advective Fortran mixing routine into `mppnp` including translating my 1D post-processing mixing data into an appropriate file format for `mppnp`. Pavel also physically ran both the diffusive and advective models and created *python* notebooks to create Figures 4.1, 4.7 and 4.6 which are shown in this chapter.

4.1 Metal Poor Stars

Any metal poor star is expected to have only been contaminated by a single or a small number of nucleosynthetic events. Therefore they are excellent probes into determining the various nucleosynthetic processes that were present in the early universe. The carbon enhanced metal poor (CEMP) stars have an additional tag to their name to state the likely source of metal contamination observed on their surfaces. The work of Bisterzo et al. (2012) observed the abundances for CEMP-s (*s*-process metals observed) and CEMP-r/s (*r*-process and *s*-process metals observed) stars. The canonical approach to explain the heavy metal elemental abundance patterns on a CEMP-r/s star is to use a mixture of *s*-process and *r*-process yields. Bisterzo et al. (2012) explained the CEMP-r/s stars elemental abundances by theorizing that the *s*-process contamination came from a companion AGB star and the initial gas cloud that the star formed in was enriched with *r*-process material. Some of the CEMP-r/s stars of Bisterzo et al. (2012) were unable to have their elemental abundance patterns be explained by mixtures of *s*-process and *r*-process material from the suspected sources. This was due, in part, to the large spread in the abundances of first-peak elements such as Zr and Y being poorly fit by mixtures of *s*-process and *r*-process material. A metal poor star, HD94028 (Roederer et al., 2016), is also unable to be described with mixtures of *s*-process and *r*-process material. Roederer et al. (2016) claim that the super solar [As/Ge] ratio observed in HD 94028 can be explained with the *i*-process. They propose that the elemental abundances of this star come from a mixture of *s*-process, *i*-process and *r*-process material. They do not provide a definitive site for the source of the *i*-process material but state that the *i*-process is ubiquitous with H-ingestion into a convective He-burning region (Herwig et al., 2011) and state a few scenarios in which this could occur. There is also no discussion on how the particular proportions of the *s*-process, *i*-process, and *r*-process material could all be mixed within this star.

Some of the major uncertainties in determining *s*-process, *i*-process and *r*-process contributions to stellar elemental abundances comes from the uncertainties in their formation sites. For the *i*-process within He-shell convection zones, the rate of H-ingestion and the mixing details dictate the neutron densities while the neutron exposure (Kippenhahn et al., 2012),

$$\tau = v_{\mathrm{T}} \int N_n(t)dt \tag{4.1}$$

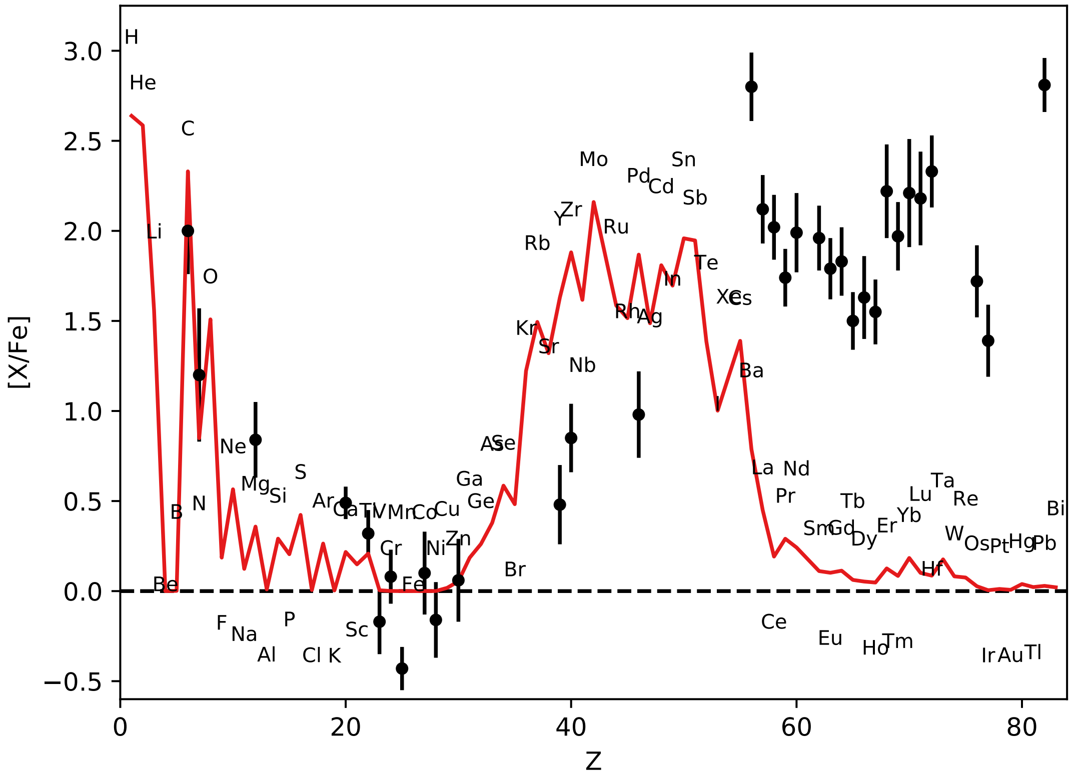

Figure 4.1: The elemental abundances of the *i*-process material within the He-shell assuming that all of the unstable species have decayed from the H-ingestion event and it is diluted. This is the distribution after 8 days, out of the entire month of the H-ingestion event. The neutron exposure is not enough for the *i*-process to produce significant amounts of Pb.

τ, dictates where the abundances of the heaviest elements peak. In equation 4.1 v_{T} is the thermal velocity and N_n is the neutron density. The neutron exposure is used as a proxy to predict how much of the initial seed material, typically ^{56}Fe, is able to capture enough neutrons to get all the way to ^{208}Pb. This can be seen when comparing the advective mixing post-processing models of the RAWD when the material has been exposed to *i*-process neutron densities for 8 days in Fig. 4.1 compared with 20 days in Fig. 4.7. There is also the mixing of the ^{13}N within the convection zone which dictates where ^{13}C is produced and the efficiency to which it captures ^{4}He, based on the temperature, to release a neutron. On top of all this, because the *i*-process populates species that are far from stability, the neutron capture cross-sections can be very uncertain with most not being experimentally determined. This can have major implications for the interpretation of results due to different isotopes being the deadlock or branching points of the flow of neutron-rich species (Denissenkov et al., 2018; McKay et al., 2019) which can dramatically change isotopic abundance ratios.

4.2 Advective and Diffusive RAWD Models

The limitations of the results of Chapter 3 is that the advective mixing model was written in *python* and it only included the $^{12}\mathrm{C}(p,\gamma)^{13}\mathrm{N}$ reaction which is the only reaction in the `PPMstar` simulations. Implementing a full nucleosynthesis network for computing the *i*-process in *python* would slow the advective mixing model to a crawl. There would also need to be a diffusive mixing implementation to be written in order for a comparison to be made. Instead, a general nuclear network and diffusive mixing solvers are already included in the `mppnp` code, outlined in Herwig et al. (2011), and so the advective mixing model would only need to be written within `mppnp`'s framework in order to replace the diffusive mixing portion of the routine.

The `mppnp` code operates under two assumptions, the energy feedback from the reactions it computes is already included in the evolution of the thermal stratification and that the burning and mixing operators can be split. The `mppnp` code operates by first solving the nuclear burning implicitly with a particular timestep and then immediately after implicitly solves the diffusive mixing over that same timestep. Using an advective mixing routine requires some changes to this mode of operation because of the fact that the advective timestep is limited by the Courant condition. These explicit timesteps are much shorter than the typical implicit burning timestep and so many subtime steps are taken. Since the burn and mixing operators are split, there is some mixing occurring with no burning. This is still appropriate for `N16` because for a given *dump*, which is the burning implicit time step that is used, there are approximately 20 subtime steps being taken to compute the advective mixing. Since the maximum Courant number of any cell is $C = 0.5$ (Section 3.3.3.5), at the worst case fluid is able to advect 10 cells within the simulation for every burning timestep. Over the 15 Mm of the simulation there are approximately 350 cells which means at the worst case, fluid is able to advect 0.4 Mm throughout the convection zone before an implicit burn step is taken again. This can become significant if post-processing a run like `N17` where there are approximately 40-50 subtime steps being taken and its resolution is lower leading to fluid advecting approximately 1.1 Mm.

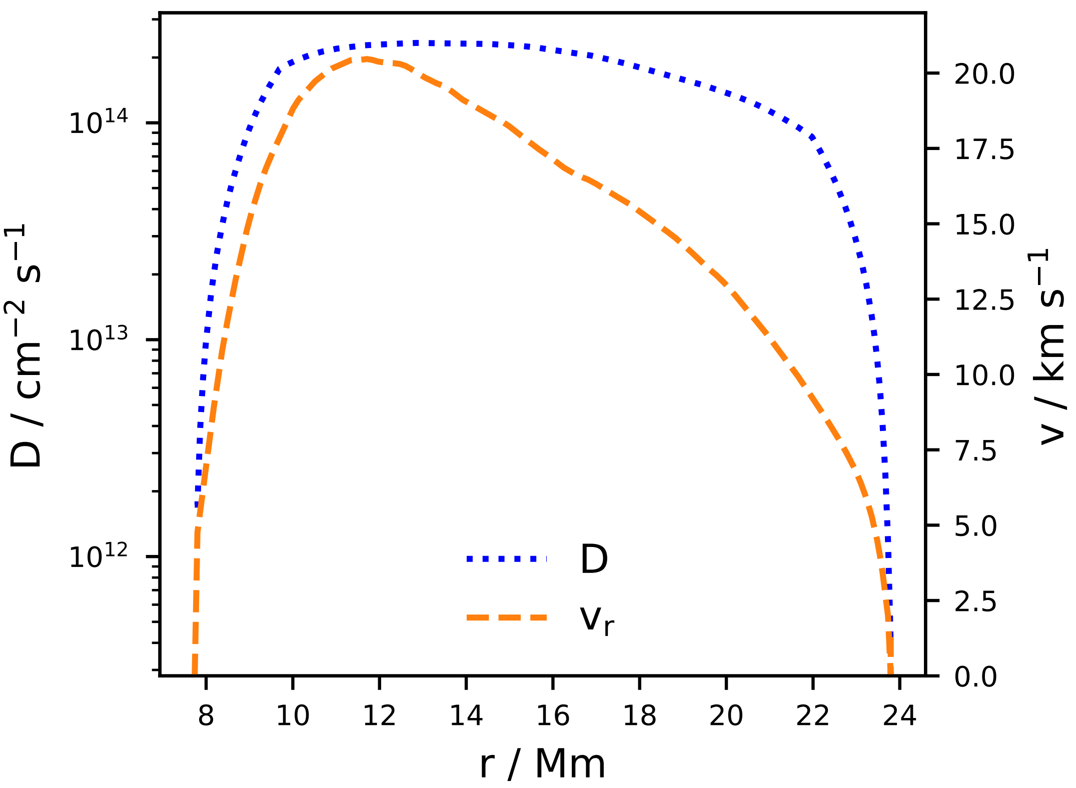

Figure 4.2: The spherically averaged radial velocity and diffusion coefficient from `N16` at $t = 299$ min. The diffusion coefficient is estimated with equation 1.19 where the velocity is the spherically averaged radial velocity. The length scale is the typical choice in stellar applications, equation 1.20.

In many of the burning `PPMstar` simulations, such as the C-ingestion of Ritter et al. (2018a), the diffusion coefficients are estimated by inverting the diffusion equation (equation 1.18) as outlined in Section 3.3.2. Of course, some of this H is burned as it is advected within the convection. The burning of H can be estimated and inverted in order to obtain the diffusive mixing of the H and it is also described in Section 3.3.2. In order to estimate the diffusion of the X_{H} throughout the convection zone there needs to be H everywhere within the convection zone. This is untrue for the RAWD case as it is all burned well before it reaches the bottom of the convection zone as seen in Figures 3.13 and 2.1. Instead, the simplest estimates of a diffusion coefficient can be done with equation 1.19 where the velocity is the *rprof* radial velocities and the length scale is from equation 1.20. This diffusion coefficient and the velocity at $t = 299$ min for the i-process nucleosynthesis post-processing of `N16` is shown in

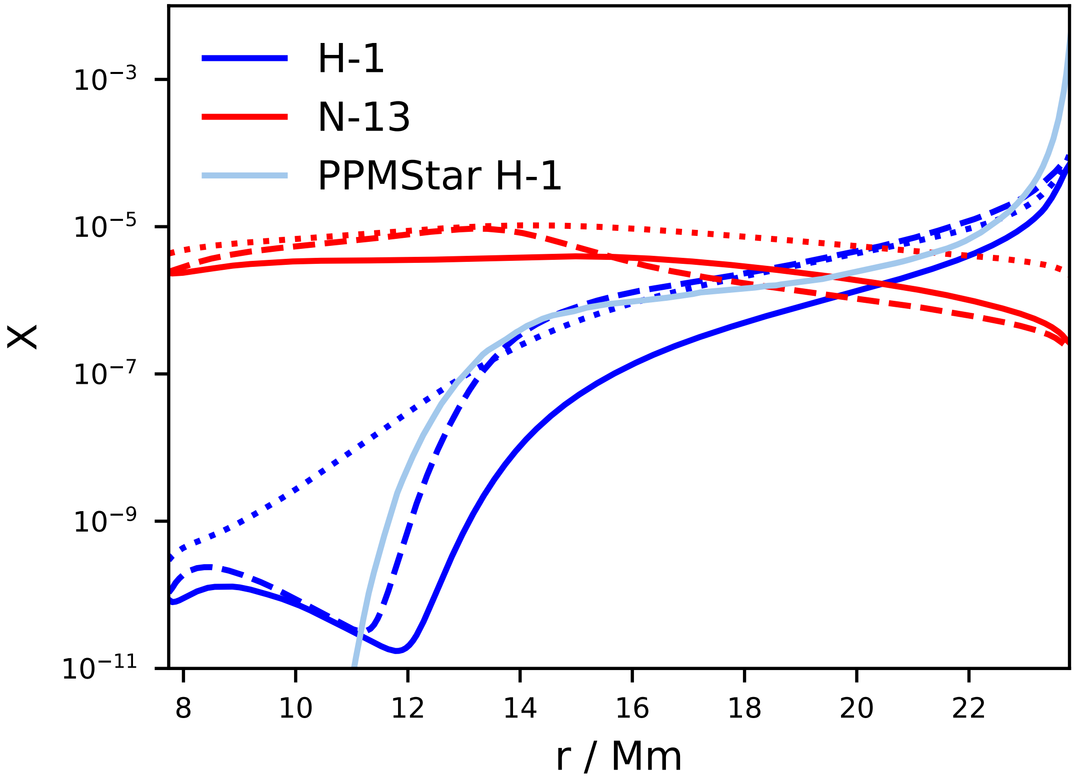

Figure 4.3: The coloured lines represent the two different species, H and ^{13}N while the linestyle refers to the particular mixing model when the mixing is computed in `mppnp`. The two different algorithms for computing the mixing in the convection zone for `mppnp` are the advective mixing model (Chapter 3) and a diffusive mixing model. The solid line is the upstream of the advective model while the dashed line is the downstream of the advective model. The dotted line is from the diffusive mixing model. There is an additional line referring to the X_{H} from the `PPMstar` simulation of `N16`. These are all taken at $t = 299$ min.

Fig. 4.2.

The diffusive and advective mixing models have exactly the same initial conditions as well as have the same evolution of the stratification and entrainment of H computed directly from the `N16` simulation. The only difference between the two models is how the species within the convection zone are transported and thus mixed within it. A plot of the H and ^{13}N at $t = 299$ min for both the diffusive and advective mixing models is shown in Fig. 4.3. The advective mixing model is able to reproduce the burning region of the $^{12}\mathrm{C}(p,\gamma)^{13}\mathrm{N}$ reaction but there is an additional tail of protons at the bottom of the convection zone. This contrasts to the `PPMstar` simulations because

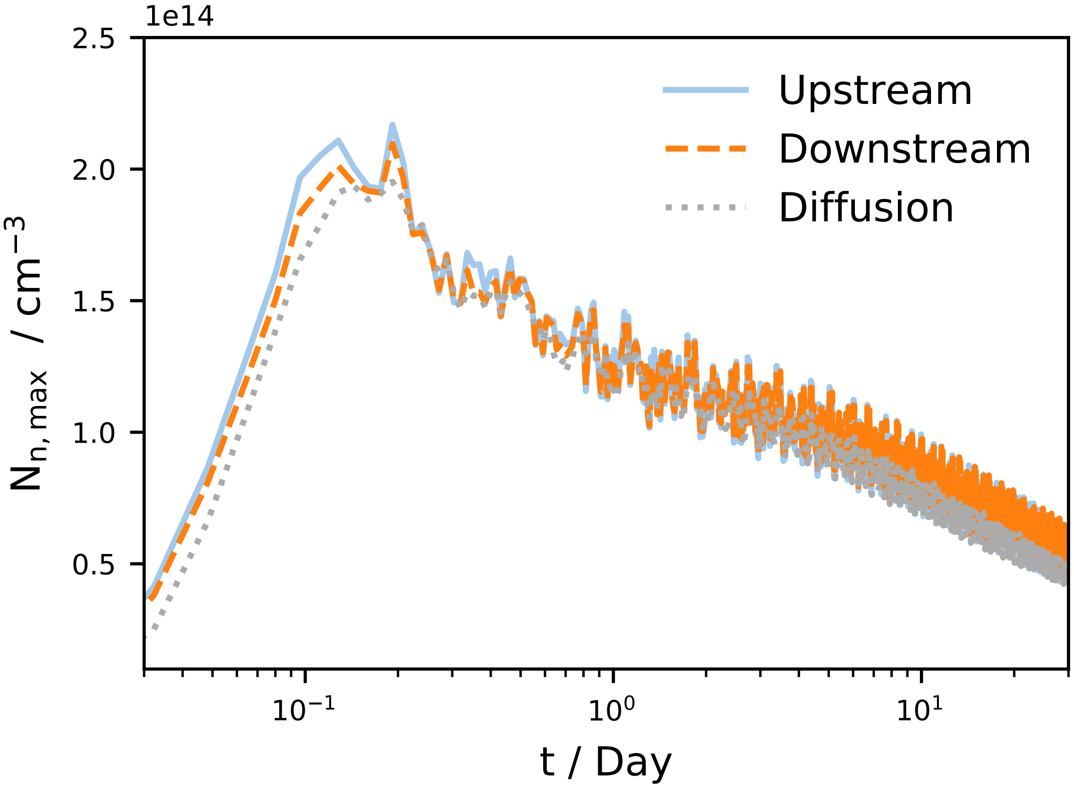

Figure 4.4: The maximum neutron density within the convection zone from the diffusive mixing model and the two stream advective mixing model as a function of time. There is data for the entire H-ingestion event, 30 days.

it only includes the ^{12}C$(p,\gamma)^{13}$N reaction by transforming one fluid, $\mathcal{F}_1$, into another, $\mathcal{F}_2$. There are (n,p) reactions occurring at the bottom of the convection leading to a sudden rise in the X_{H} profile well within the ^{12}C$(p,\gamma)^{13}$N burning region. The diffusive mixing model, in an average sense, captures the interplay between the (n,p) reactions and the ^{12}C$(p,\gamma)^{13}$N reaction but there is not a sharp transition between the two regions like in the advective mixing model.

From the advective mixing model there is less ^{13}N being produced and most of it is concentrated at the bottom of the convection zone while the diffusive mixing model spreads it out more evenly. With nearly equal $X_{^{13}\mathrm{N}}$ at the bottom of the convection zone in both models, there will be roughly the same amount of ^{13}C$(\alpha,n)^{16}$O reactions and thus similar amounts of neutrons. The maximum neutron density within the convection zone as a function of time is shown Fig. 4.4. A couple of unstable species that are associated with i-process neutron densities, ^{78}Ge and ^{88}Kr, with half lives of

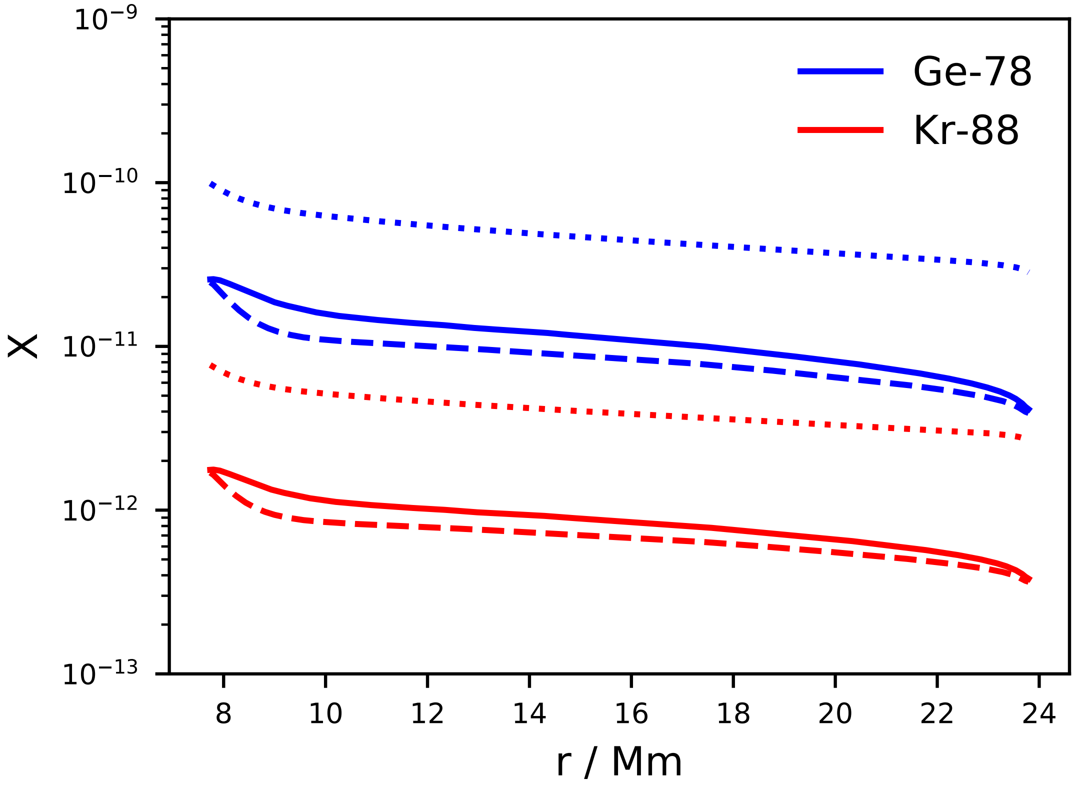

Figure 4.5: The coloured lines represent the two different species, ^{78}Ge and ^{88}Kr while the linestyle refers to the particular mixing model. The two different algorithms for computing the mixing in the convection zone are the advective mixing model (Chapter 3) and a diffusive mixing model. The solid line is the upstream of the advective model while the dashed line is the downstream of the advective model. The dotted line is from the diffusive mixing model.

$\approx$ 1 hour after $t = 299$ minutes of simulation time are shown in Fig. 4.5.

The H-ingestion event lasts for roughly an entire month (Fig. 1.1) while the 3D simulation of said event, `N16`, only lasted approximately 12 hours. With the assumption that the quasi-static entrainment and burning of H occurring during the He-flash continues like in `N16`, it can be modeled by repeating the post-processing of `N16` 60 times. The neutron exposures during the He-flash are large enough to produce the signatures of the *i*-process near the second peak. The elemental abundance patterns from the nucleosynthesis within the RAWD can be compared with observations of elemental abundances on the surfaces of metal poor stars. One such star, CS31062-050 (Iwamoto et al., 2004; Johnson & Bolte, 2004), has an elemental

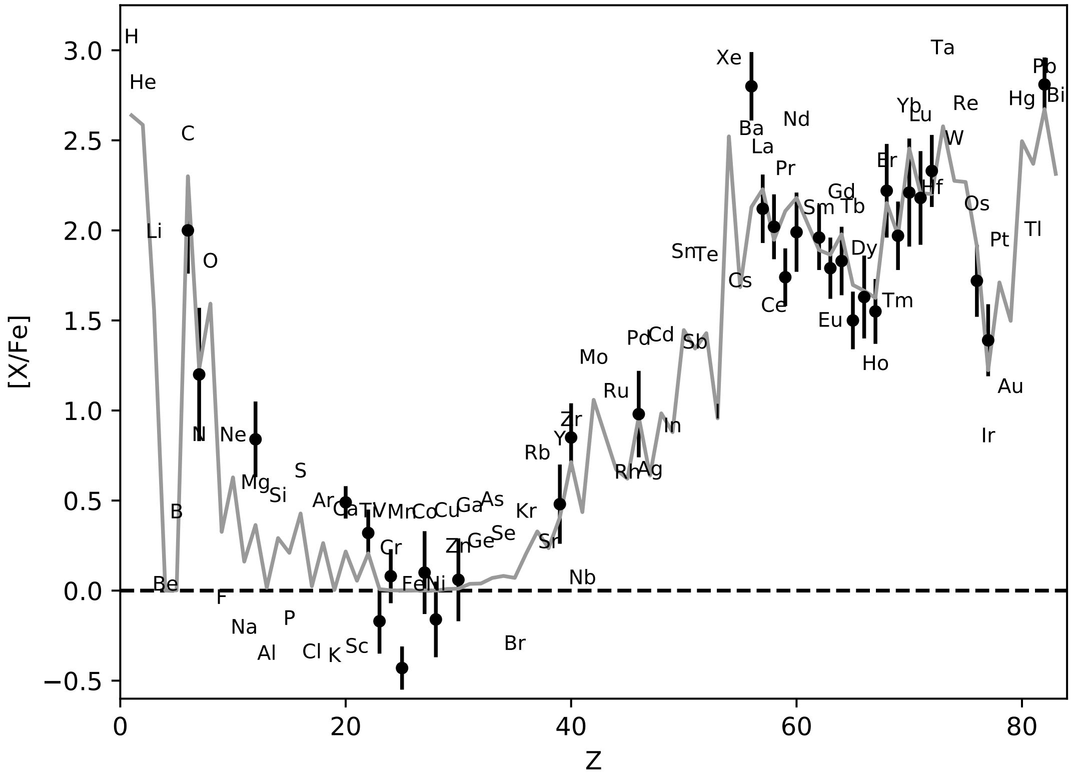

Figure 4.6: The elemental abundances of the *i*-process material within the He-shell, assuming that all of the unstable species decayed, after 15 days of H-ingestion. This is the best-fit to the star CS31062-050 for the diffusive mixing model. The H-ingestion event lasts for approximately 1 month.

abundance pattern that matches the diffusive mixing RAWD model very well after 15 days of H-ingestion and is shown in Fig. 4.6. The advective mixing model requires 20 days to have a large enough neutron exposure to produce the observed Pb elemental abundance and match the observations of CS31062-050 (Fig. 4.7). Both the diffusive mixing and advective mixing models produce remarkably similar elemental abundance patterns however the H-ingestion event needs to be longer in the advective mixing model to reach the large abundance of Pb. The advective mixing model takes longer for the material to have a neutron exposure that is comparable to the diffusive mixing model for the simple reason that the neutron density is not isotropic. This can be seen in Fig. 4.8 where the neutron densities within the downstream are noticeably smaller than the upstream. The neutron density in the advective model also falls off much more sharply as a function of radius than the diffusive model sug-

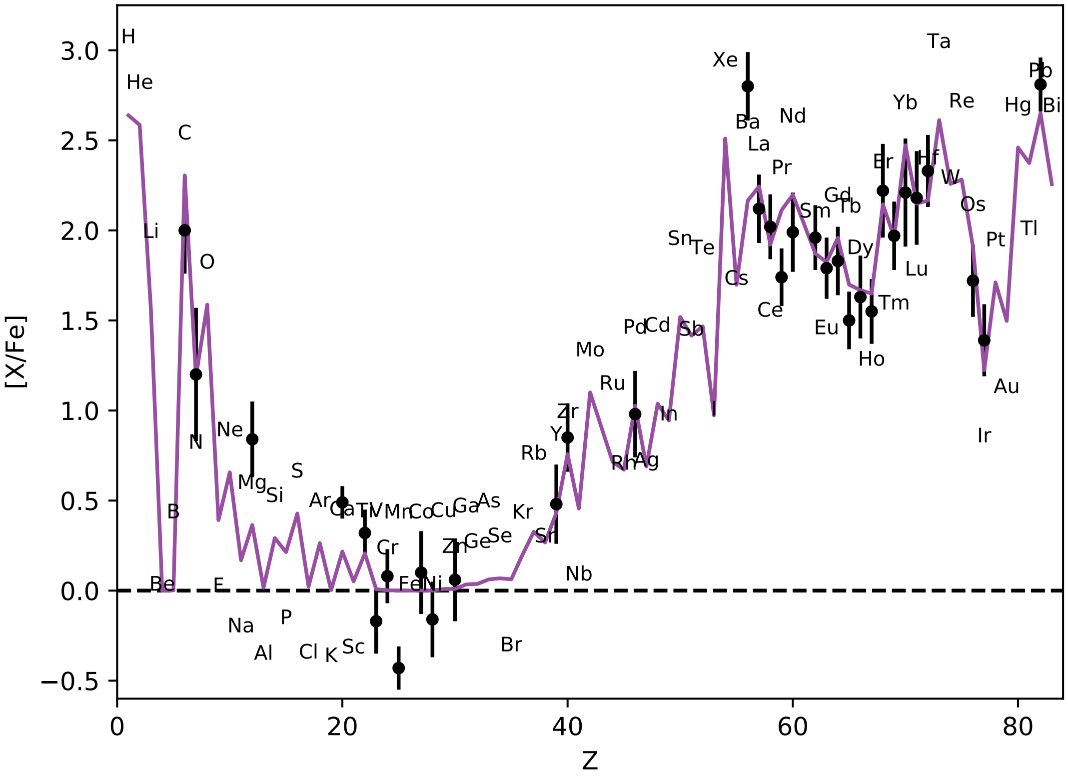

Figure 4.7: The elemental abundances of the *i*-process material within the He-shell, assuming that all of the unstable species decayed, after 20 days of H-ingestion. This is the best-fit to the star CS31062-050 for the advective mixing model. The H-ingestion event lasts for approximately 1 month.

gesting that the diffusion method is overestimating the mixing of species throughout the convection zone. With the neutron density being larger in the upstream than the downstream this could suggest that since the bulk of the ^{13}N is produced in the downstream it takes time for it to advect down to the bottom of the convection zone where it will be transferred to the upstream and then subsequently decays. There is also a different (n, p) and (p, γ) equilibrium at the bottom of the convection zone as seen in Fig. 4.3.

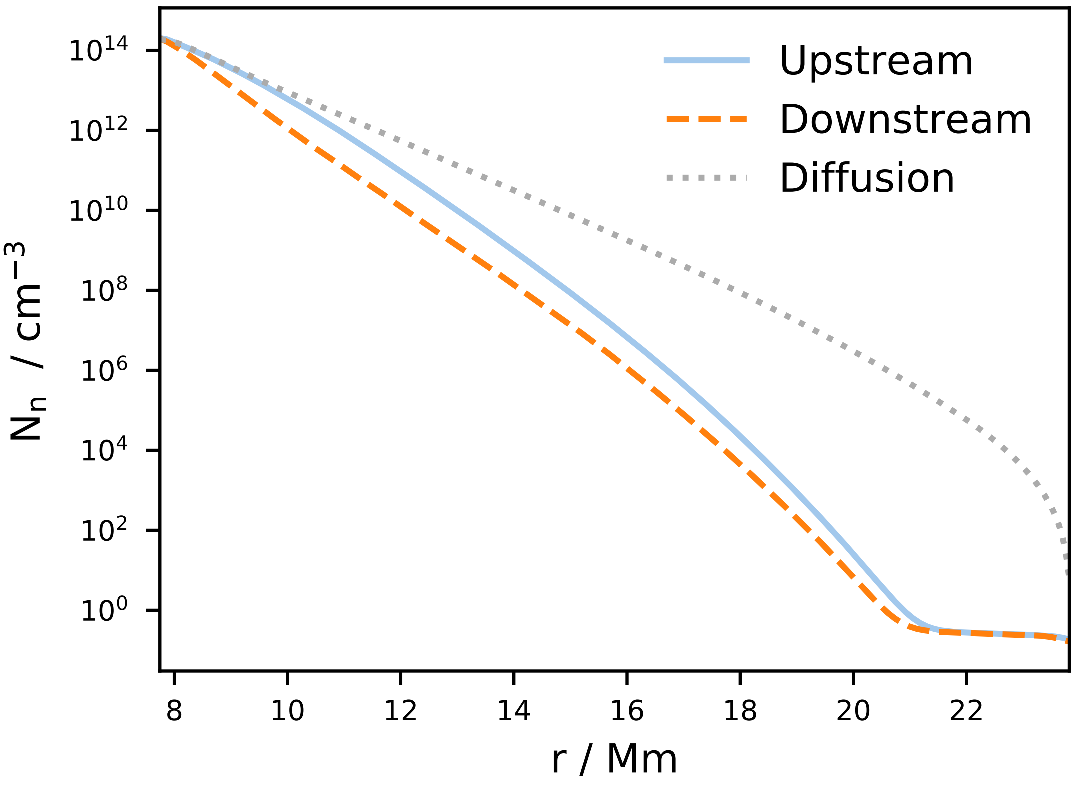

Figure 4.8: The neutron densities within the convection zone at $t = 299$ min for the advective and diffusive mixing models.

5

Summary and Conclusions

Obtaining the *briquette* 3D data of the `PPMstar` simulations required the development of computational tools. All thermodynamic quantities in the `PPMstar` simulations are close to spherically symmetric. In order to obtain valuable information about them that is not already contained in the spherically averaged *rprofs* data, the underlying 3D cartesian cubic grid of the *briquette* data needed to be interpolated onto spheres. Plotting and obtaining averages of quantities on spheres in a non-biased manner required distributing points evenly on a sphere such that they cover equal surface areas on the sphere. This required a non uniform sampling of the θ coordinate. With points distributed evenly on a sphere any interpolation method could be used to determine a quantity on that sphere and visualized with a mollweide projection.

The various methods of interpolating quantities: binning, trilinear interpolation, quadratic interpolation and cubic interpolation were compared. The binning method can be used for obtaining estimates of radial profiles of quantities however it cannot be used for 3D visualization due to the large numerical effects shown in Fig. 2.2. The quadratic interpolation, a variation of which is used in the PPM method, poorly represented the underlying functionality of an analytic tanh function which represents the FV within the transition region. This was due to the fact that the method does not ensure continuity of the interpolation functions from one cell to the next but instead relies on the data being sufficiently sampled so that the interpolation is approximately continuous. The interpolation methods of cubic splines and the `PCHIP` algorithm were also applied to the analytic tanh function with both interpolations closely following the analytic result. However, when they were applied to the FV data of `M29` the cubic spline method over and undershoots the data, introducing new maxima and minima to the data. With the constraints on the FV values to be between 0 and 1, the cubic spline method cannot be used because it can have values of $FV > 0$. The cubic spline method also cannot be feasibly applied to any of the *briquette* data due to the computational work required for interpolating on the 3D data set. The `PCHIP` method could be suitable for the *briquette* data however its extension to 3D is not straightforward. The simplicity in 3D and the constraints of the trilinear interpolation method made it the method of choice for any interpolation in this work as discussed in detail throughout Chapter 2.

For applications of diffusive mixing, determining the diffusion coefficients from *briquette* data requires the computation of the radial gradient of X_{H} on spheres which is computed using the FV. Computing the radial derivative on a cartesian grid required changing basis vectors from cartesian to radial due to the numerical derivatives being calculated in the cartesian basis. Then, the radial gradient was interpolated onto a sphere. Using the trilinear interpolation, computing the radial gradient of FV in this manner had significant numerical artifacts even with 384^3 *briquette* data (Fig. 2.6). Using the higher order interpolation method, `PCHIP`, and then taking the derivatives of the interpolating function is not usable because of the discontinuities in the second derivative of the interpolating function. The choice of how to estimate the numerical derivative also modified the interpolated values. There is also the issue that the `PCHIP` and trilinear interpolation methods do not introduce any new maxima or minima between interpolated points. This means that applications of these interpolation methods to defining the convective boundary as the minimum gradient of the tangential velocity, as in Jones et al. (2017), will always choose a grid point.

A 1D advective mixing model was formulated, implemented and applied to a RAWD in Chapter 3. It is comprised of two streams, a downstream which transports H-rich material down to the H-burning region and an upstream which transports H-free material to the upper convective boundary. A model of the horizontal mixing between the two streams was formalized and it has a coefficient, γ, that is calibrated from the horizontal mixing properties of the 3D simulations of the RAWD. In order to describe the flow characteristics, justify the approximations of the two stream model, and determine the γ coefficients, the *briquette* data and the numerical techniques described in Chapter 2 were used extensively. This included creating mollweide plots of quantities, such as v_r, X_{H} and ρ and computing power spectra (spherical harmonics) of v_r at various radii within the convection zone. Each of the burning runs `N15`, `N16` and `N17`, had different time dependent behaviour for the entrainment of H (Fig. 3.10). In `N15` there was a minor GOSH that occurred around $t = 500$ min which increased the entrainment of H into the convection zone. The burning of this H did not cause a runaway feedback event like in `N17` and the GOSH dissipated after $t = 700$ min. There was no additional GOSH in `N15` over the 1600 minutes of simulation time. `N16` had the same heating rate as `N15` but had quasi-static entrainment and burning across its entire simulation time, 744 minutes, with no traces of a GOSH. The advective post-processing model of `N16` reproduces the total mass of H burned, the rate of H burning and the location of the H burning that is measured in the `PPMstar` simulations. This is also true during the dramatic changes in entrainment and burning rates of H that `N15` and `N17` experience during their GOSH's. The advective post-processing model can faithfully model the RAWD 3D hydrodynamic simulations in all conditions.

The limitations of the models presented in Chapter 3 are due to the fact that the burning network only included the $^{12}\mathrm{C}(p,\gamma)^{13}\mathrm{N}$ reaction. However, implementing the advective mixing routine into the nucleoysnthesis post-processing code `mppnp` (Herwig et al., 2011) allows for the inclusion of reactions for over 1000 isotopes which was needed to model the i-process. In Denissenkov et al. (2019) the i-process nucleosynthesis of model G used diffusive mixing within the convection zone. Comparing the advective and diffusive mixing models of this scenario, with the same stratification, H entrainment and simulation time, immediately shows differences in the burning signatures of each method. After only $t = 299$ min of simulation time, or 8 convective turn over times, the quasi-static burning of each is established. The X_{H} profile from the diffusive mixing model has a gradual drop from the top of the convection zone to the bottom while the profile from the advective model sharply drops where the `PPMstar` simulations predict the bulk of the $^{12}\mathrm{C}(p,\gamma)^{13}\mathrm{N}$ reactions to occur. With the extended network there are sources of protons at the bottom of the convection zone from (n,p) reactions leading to a sudden rise in the X_{H} profile in the advective mixing model. The resulting $^{13}\mathrm{N}$ production and thus neutron densities as a function of time are very similar from the two models. One notable difference is that the $^{13}\mathrm{N}$ is more concentrated towards the bottom of the convection zone in the downstream of the advective mixing model than the diffusive mixing model.

Running the advective and diffusive mixing for the entirety of the H-ingestion into the He-shell of the RAWD shows significant differences between the models in the efficiency to which the neutrons are able to transform the $^{56}\mathrm{Fe}$ seeds to heavier elements up to $^{208}\mathrm{Pb}$. Comparing the elemental abundances of each model with the elemental abundances of the CEMP-r/s star CS31062-050 shows that the diffusive mixing is able reproduce the abundance pattern for most species, except Ba, after 15 days of exposure. The advective mixing model requires 20 days to reach high enough abundances of Pb to match observations. This is due to the anisotropic distribution of neutron densities between the two streams and the complicated interplay between the (n, p) and (p, γ) reactions at the bottom of the convection zone.

6

Future Work

The 1D advective mixing model can be applied to many different convective-reactive environments. The model is not only able to calculate the nucleosynthesis from the quasi-static burning of `N16` but it is also able to evolve with the rapid H-ingestion events of `N17`. This means that it could also be applied to Sakurai's Object where a GOSH occurs in the models of Herwig et al. (2014). It could also be applied in cases of C-ingestion into a O-shell. There, the nucleosynthesis has an interesting odd-Z elemental pattern (Ritter et al., 2018a) that could be significant for the galactic chemical evolution of said elements Côté et al. (2018) but the details of the nucleosynthesis pathways are not known. Here there are multiple burning layers of (γ, p) and (p, γ) reactions that produce the odd-Z elements that could be influenced by the mixing details. The 1D advective model could also relax many of its constraints, such as having equal velocities in both streams and uniform density and mass conservation on a cell basis, for cases in which these assumptions are not true like surface convection. The model currently only uses two streams with horizontal mixing between them. It could be extended to include more streams to get a more accurate representation of the 3D flow while only modestly increasing the computational effort. The 1D advective mixing model could be applied to situations in which 3D hydrodynamic simulations have not been computed for. With estimates of the velocities from MLT and suitable γ profiles nucleosynthesis can be compared with previous diffusive mixing models. This could be specifically applied to the s-process occurring in the He-shell flash convection zones of 2-3$M_\odot$ stars. There, the ^{22}Ne$(\alpha, n)^{25}$Mg reaction can occur in a narrow region near the bottom of the convection zone where temperatures are high enough. Perhaps the advective transport of material changes how much fuel brought to the bottom of the convection zone where it is burned producing large s-process neutron densities that rearrange the isotopic ratios of the now mixed ^{13}C pocket material (Battino et al., 2016) from a previous exposure of *s*-process neutron densities. Isotopic information of this *s*-process material can be observed as the material in the He-shell convection zone eventually mixes into the H-envelope of the star and forms SiC grains when it is lost to stellar winds during the stars AGB phase. The metals from the ^{13}C pocket are encoded in the grains and spread across the galaxy. Pre-solar SiC grains from AGB stars have been brought to Earth and provide valuable information on the isotopic ratios of metals (Barzyk et al., 2006) which can be used to constrain the mixing processes in the He-shell flash convection zones of intermediate mass stars.

Bibliography

Abbott B. P., et al., 2017, Phys. Rev. Lett., 119, 161101

Andrassy R., Herwig F., Woodward P., Ritter C., 2018, eprint arXiv:1808.04014

Angulo C., Arnould M., Rayet, M. et al. 1999, Nucl. Phys., A 656, 3

Asplund M., Lambert D. L., Kipper T., Pollacco D., Shetrone M. D., 1999, A&A, 343, 507

Barzyk J. G., Savina M. R., Davis A. M., Gallino R., Pellin M. J., Lewis R. S., Amari S., Clayton R. N., 2006, , 50, 587

Battino U., et al., 2016, , 827, 30

Biermann L., 1932, , 5, 117

Bisterzo S., Gallino R., Straniero O., Cristallo S., Käppeler F., 2012, , 422, 849

Busso M., Gallino R., Lambert D. L., Travaglio C., Smith V. V., 2001, , 557, 802

Cannon R. C., 1993, Monthly Notices of the Royal Astronomical Society, 263, 817

Carter A., 2001, Classical and Statistical Thermodynamics. Raymond F. Boyer Library Collection, Prentice Hall

Chandrasekhar S., 1961, Hydrodynamic and hydromagnetic stability

Clarke C., Carswell B., 2007, Principles of Astrophysical Fluid Dynamics. Cambridge University Press

Clarkson O., Herwig F., Pignatari M., 2017, Monthly Notices of the Royal Astronomical Society: Letters, 474, L37–L41

Colella P., Woodward P. R., 1984, Journal of Computational Physics, 54, 174

Côté B., Denissenkov P., Herwig F., Ruiter A. J., Ritter C., Pignatari M., Belczynski K., 2018, , 854, 105

Cowan J. J., Rose W. K., 1977, , 212, 149

Cox J. P., Giuli R. T., 1968, Principles of stellar structure. New York, Gordon and Breach [1968], New York

Davis A., Jones S., Herwig F., 2019, , 484, 3921

Denissenkov P. A., Herwig F., Battino U., Ritter C., Pignatari M., Jones S., Paxton B., 2017, ApJ Lett., 834, L10

Denissenkov P., et al., 2018, Journal of Physics G: Nuclear and Particle Physics, 45, 055203

Denissenkov P. A., Herwig F., Woodward P., Andrassy R., Pignatari M., Jones S., 2019, MNRAS, 488, 4258

Dimotakis P. E., 2005, Annual Review of Fluid Mechanics, 37, 329

Fritsch F. N., Carlson R. E., 1980, SIAM Journal on Numerical Analysis, 17, 238

Harris J. A., Hix W. R., Chertkow M. A., Lee C. T., Lentz E. J., Messer O. E. B., 2017, , 843, 2

Henkel K., Karakas A. I., Lattanzio J. C., 2017, Monthly Notices of the Royal Astronomical Society, 469, 4600

Herwig F., 2000, , 360, 952

Herwig F., Pignatari M., Woodward P. R., Porter D. H., Rockefeller G., Fryer C. L., Bennett M., Hirschi R., 2011, , 727, 89

Herwig F., Woodward P. R., Lin P.-H., Knox M., Fryer C., 2014, ApJ, 792, L3

Iwamoto N., Kajino T., Mathews G. J., Fujimoto M. Y., Aoki W., 2004, , 602, 377

Johnson J. A., Bolte M., 2004, , 605, 462

Jones S., Andrássy R., Sandalski S., Davis A., Woodward P., Herwig F., 2017, MNRAS, 465, 2991

Kippenhahn R., Weigert A., Weiss A., 2012, Stellar Structure and Evolution. Springer, doi:10.1007/978-3-642-30304-3

Kundu P. K., Cohen Ira M. a., Dowling David R. a., 2012, Fluid mechanics, fifth edition edn. Waltham, MA : Academic Press

LeVeque R. J., 2002, Meccanica, 39, 88

McKay J. E., Denissenkov P. A., Herwig F., Perdikakis G., Schatz H., 2019, arXiv e-prints, p. arXiv:1909.07011

Meakin C. A., Arnett D., 2007, , 665, 690

Meyer B. S., 1994, , 32, 153

Müller B., Janka H.-T., 2015, , 448, 2141

Oswalt T. D., Barstow M. A., 2013, Planets, Stars and Stellar Systems Vol. 4, doi:10.1007/978-94-007-5615-1.

Paxton B., Bildsten L., Dotter A., Herwig F., Lesaffre P., Timmes F., 2010, , 192, 3

Porter D. H., Woodward P. R., 1994, ApJS, 93, 309

Porter D. H., Woodward P. R., 2000, ApJS, 127, 159

Ritter C., Andrassy R., Côté B., Herwig F., Woodward P. R., Pignatari M., Jones S., 2018a, , 474, L1

Ritter C., Herwig F., Jones S., Pignatari M., Fryer C., Hirschi R., 2018b, Monthly Notices of the Royal Astronomical Society, 480, 538

Roederer I. U., Karakas A. I., Pignatari M., Herwig F., 2016, The Astrophysical Journal, 821, 37

Woodward P. R., 1986, in Winkler K.-H. A., Norman M. L., eds, NATO Advanced Science Institutes (ASI) Series C Vol. 188, NATO Advanced Science Institutes (ASI) Series C. p. 245

Woodward P. R., 2007, in Grinstein F. F., Margolin L. G., Rider W. J., eds, , Implicit Large Eddy Simulation, Computing Turbulent Fluid Dynamics. Cambridge University Press, Cambridge, p. 130

Woodward P., Colella P., 1981, in W. C. Reynolds and R. W. MacCormack ed., , Lecture Notes in Physics. Springer Verlag, Berlin, pp 434–441

Woodward P., Colella P., 1984, Journal of Computational Physics, 54, 115

Woodward P. R., Herwig F., Lin P.-H., 2015, , 798, 49

Woosley S. E., Weaver T. A., 1995, , 101, 181

Yadav N., Bernhardüller Janka H. T., Melson T., Heger A., 2019, arXiv e-prints, p. arXiv:1905.04378

Appendix A

Advective Mixing Code

With the bulk of the scientific work in this thesis being concentrated into the development of the advective mixing algorithm, that code which mixes the species within `mppnp` is made public in the repository
`https://github.com/David-Stephens/two-stream-mixing`.

The repository contains the code that uses the algorithms as described in Chapter 3. It does not contain any of the nuclear burning but is a stand alone mixing routine.